Numerical Study of a Hybrid Photovoltaic Thermal Desalination System

A thesis submitted for the Degree of Master of Science

in Sustainable Energy Engineering

Cole Douglas Noble

Student Number: NBLCOL001

Supervisor: Dr Amos Madhlopa

Energy Research Centre

Department of Mechanical Engineering

University of Cape Town

August 2016

Plagiarism Declaration

I know the meaning of plagiarism and declare that all the work in the document, save for that which is properly acknowledged, is my own. This thesis/dissertation has been submitted to the Turnitin module (or equivalent similarity and originality checking software) and I confirm that my supervisor has seen my report and any concerns revealed by such have been resolved with my supervisor.

Name: Cole Douglas Noble

Signature:

Signed by candidate Signature removed

Date: 21 August 2016

Abstract:

The world as we know it depends highly on fossil fuels. However, these resources are finite, and evidence suggests that their combustion contributes to climate change. In addition, fresh water supplies are becoming scarcer amidst instabilities in weather patterns and unsustainable water consumption levels. As such, photovoltaic (PV) systems have emerged as a potential off-grid alternative to traditional fossil fuel energy generation. However, their widespread proliferation is, in part, inhibited by their inefficiency as less than 20% of incident solar energy is converted to electrical energy. Hybrid photovoltaic thermal (PV/T) desalination systems have emerged as one way of improving the overall efficiency of PV panels as they make use of the waste heat from panels to aid the desalination process in solar stills.

Solar stills have been modelled with software for the purpose of performance optimisation, but most of them do not account for the still's view factor in the calculation of internal radiative heat transfer coefficient. The aim of this study was to construct a numerical model for a hybrid PV/T desalination system and determine its accuracy. The modelling was undertaken in Matlab and was validated against experimental data from a previous study using Root Mean Square Error (RMSE) and correlation values.

It was observed that the model performed adequately as a water yield RMSE value of 22.0% was found. Furthermore, it was found that the view factor reduces the RMSE of hourly water yield from 28.9% to 22.0% and improves the correlation factor from 0.9890 to 0.9896. Sensitivity analyses were performed with annual data from Stellenbosch, South Africa (33.935°S 18.7817°W) and indicated an optimal water depth of 0.02m for high water yield, and 0.04m for high electrical energy yield. Also, an optimal panel tilt angle of 30° was found for both water and electrical energy yields and optimal cover tilt angles of 40° and 60° were observed for maximum water and electrical yields respectively.

The conclusion of this study was that the incorporation of a view factors does indeed improve the accuracy of hybrid PV/T desalination system models. Additionally, low basin water depth is favourable for high water yields and high basin water depth, for high electrical energy yields. Furthermore, a panel tilt angle of 30° is optimum for both types of yield. Finally, the still cover tilt angle should be set to 40° for optimal water yields, but should be as steep as possible for optimal electrical energy yields.

Acknowledgements:

1) The NRF (RSES) and the University of Cape Town for two years of funding assistance
2) My mother (Diane Noble), for her financial, moral and academic support
3) My brothers and sister (Dane Noble, Justin Robbins and Haylee Robbins), for their financial and moral support
4) Dr Amos Madhlopa for his patient guidance and supervision
5) Energy Research Centre and the Department of Mechanical Engineering for their support and for the use of their facilities.

Table of Contents

Abbreviations/Acronyms

GDP -Gross Domestic Product

GCC - Gulf Corporation Council

IEA - International Energy Agency

IMP - Current max power point

IPCC -Intergovernmental Panel on Climate Change

PV- Photovoltaic

PV/T -Photovoltaic Thermal

MAE -Mean Absolute Error

MBE -Mean Bias Error

MED - Multiple Effect Distillation

MSF - Multi-Stage Flash Distillation

RMSE - Root Mean Squared Error

VMP -Voltage max power point

Nomenclature

A – surface area (m^2)

B –day of the year angle (rad)

b –breadth (m)

C –specific heat ($Jkg^{-1}K^{-1}$)

C_l– the speed of light in a vacuum (ms^{-1})

D –diameter of water tube (m)

E –electric power generated (W)

E_g –band gap energy (eV)

E_f–final energy state (eV)

E_i –initial energy state (eV)

f–Darcy friction factor (dimensionless)

f_l –frequency of light (Hz)

FF –Fill Factor (dimensionless)

G –solar radiation flux (Wm^{-2})

H_{buo}– buoyant pressure head (Nm^{-2})

H_f– frictional head (Nm^{-2})

H_t –Irradiation on tilted surface for a day (Whm^{-2})

H_z –Irradiation on horizontal surface for a day (Whm^{-2})

h –heat transfer coefficient (Wm^{-2} K)

h_p– Planck's constant (Js)

h_{lw} – heat transfer coefficient between the cover of the still and the water (total) (Wm^{-2} K)

I_{sc}– short circuit current (A)

K_1 -perturbation factor (dimensionless)

K_2 -background diffuse radiation (Wm^{-2})

k –thermal conductivity ($Wm^{-1}K^{-1}$)

L –length (m)

M –mass (kg)

M_r –effective air mass length accounting for refraction only (dimensionless)

M_{rz} –effective air mass length accounting for refraction and pressure differences (dimensionless)

$\dot{m}$ –mass flow rate (kgs^{-1})

N –Number (dimensionless)

Nu –Nusselt number (dimensionless)

n –refractive index (dimensionless)

Pr – Prandtl number (dimensionless)

P_{ki} –The partial vapour pressure of the water vapour at the inner surface of the solar still cover (Nm^{-2})

P_o – atmospheric pressure (Nm^{-2})

P_z – The air pressure at some height (z) above sea level (Nm^{-2})

P_w –The partial vapour pressure of the water vapour at the inner surface of the water in the still (Nm^{-2})

Q –energy flux (W)

R –thermal resistance (KW^{-1})

R_b–Ratio of tilted radiation to horizontal radiation (dimensionless)

Re –Reynolds number (dimensionless)

r – reflectivity (dimensionless)

r_c –ratio of solar cell area to aperture area (dimensionless)

r_{cor}–correlation value (dimensionless)

T –temperature (°C)

T_w–temperature of water in basin (collector inlet) (°C)

T_{w1}– average temperature of water in the tube (°C)

T_{w2}–temperature of water from the collector output (°C)

T_r– Linke factor (FTU)

t –Celsius temperature (ITS-90, °C)

t_{68} –Celsius temperature (IPTS-68, °C)

T_{68} –Kelvin temperature (IPTS-68, K)

t_{90} –Celsius temperature (ITS-90, °C)

u –flow velocity (ms^{-1})

v –kinematic velocity (m^2s^{-1})

V –View factor (dimensionless)

V_{oc} – open circuit voltage (V)

W –width or spacing (m)

x –distance (m)

x_p –average path length in each segment (m)

X_i –Theoretical value obtained from the simulation model at hour i (units depend on simulation outputs)

Y_i –specific value obtained from the experiment at hour I (units depend on experimental outputs)

Z - height (m)

Greek Symbols

α –absorptance (dimensionless)

α_s –Solar Altitude (°)

Γ – thermal conductivity ($Wm^{-1}K^{-1}$)

γ –Surface Azimuth Angle (°)

γ_g –specific gravity (dimensionless)

β –tilt angle of surface (to horizontal) (°)

β'–Volume expansion coefficient (K^{-1})

δ –thickness or depth (m)

ε –emissivity (dimensionless)

ζ –declination (rad)

η –efficiency (%)

η_g–efficiency of generation and distribution (%)

η_f–final equivalent efficiency (%)

θ –Angle of incidence (°)

θ_z –Zenith Angle (°)

κ – thermal diffusivity (m^2s^{-1})

Λ –extinction coefficient of glass (m^{-1})

λ_l –wavelength of light (m)

ξ –Frictional loss factor (dimensionless)

ρ –reflectance (dimensionless)

σ –Stefan-Boltzmann constant (5.67×10^8 W.m^{-2})

τ –transmittance (dimensionless)

$(\tau\,\alpha)$ – transmittance-absorptance coefficient (dimensionless)

Φ –Latitude (°)

ϒ - angle of refraction (°)

Subscripts

a –Air

ad –adhesive layer

B –beam

b –absorber plate

bb –basin bottom

bd –basin side

bo – bond

bs –basin

bw –basin water

c–convective (in the code, collector)

cc –short circuit

d –diffused

E– electrical

e – evaporative

ew –east wall

f -fluid

fw –front wall

G –global

g –glass cover

gr –ground

i – inner (in the code, also insulation material)

m –mean

n –normal/perpendicular

o –outer

ob –observations

on –outside the earth's atmosphere

p –PV plate

PV/T –Photovoltaic Thermal

q –collector

r – radiation

ref – reference

rw –rear wall

s –sky

sc –solar cell

sh –shunt

st –solar time (minutes)

std –standard time (minutes)

sur –surface

sw –sea water

t –tube

th –thermal

w –water

ww –west wall

z –horizontal

κ –cover of the solar still

Ψ – insulation material

1 Introduction

1.1 General

This introductory chapter highlights the context, technical background, problem statement and the aim and objectives of this study. In order to do this, the chapter starts by examining the context problems of energy security, CO_2 emissions, climate change and water shortages (Section 1.2.1). Thereafter, energy access is discussed (Section 1.2.2). Hybrid photovoltaic thermal (PV/T) desalination Systems are then introduced in Section 1.3, which is followed by a motivation for hybrid PV/T desalination system modelling (Section 1.4) and a problem statement for this thesis (Section 1.5). The aim and objectives of this study are then given (Section 1.6) which is proceeded by the scope of the study (Section 1.7) and, lastly, a thesis outline (Section 1.8).

1.2 Context

The world is highly dependent on fossil fuels as approximately 99% of all food production use oil or gas at some point and, beyond the food industry, about 95% of on-the-shelf products depend on oil for transport (Stiftung, 2007). If fossil fuel supplies were limitless and carbon emissions played no role in climate change, this dependency would not be a problem. However, oil reserves are finite (Sorrell et al., 2009) and there is evidence to suggest that the combustion of fuel is linked to climate change (Davis, Caldeira & Matthews, 2010). Also, particularly in the context of some developing countries, the twin problems of energy and clean water access already exist and as such climate change will aggravate existing drinking water access problems (Niang et al., 2014).

1.2.1 Energy Security, Climate Change and Water

Oil production is estimated to be on the decline in the range of 4-6% per annum and 6% per annum for a weighted average of oil and gas production (Höök, Hirsch & Aleklett, 2009).

Furthermore, there is a close link between the global economy and oil production. Stiftung (2007) presents a rough estimate of the relationship between oil production and global GDP. It is estimated that a 1% drop in oil production could possibly result in a 1% loss in global GDP. Also, declining oil production rates present issues surrounding energy security. More nations with declining production rates result in fewer sources for purchase (Yergin, 2006) and a consequent vulnerability to oil supply disruptions and price fluctuations. This will particularly affect those close to the poverty line as this group of people will have to spend larger portions of their incomes on energy compared to higher-earning households (Karekezi et al., 2012).

A shortage of fossil fuel is not the only energy-related problem. From an emissions perspective, multi-lateral co-operation has been implemented so as to try and keep the global temperature within a 2° C range of the pre-preindustrial levels (Houser, 2010). The New Policy scenario, drafted by the IEA (2014) makes predictions about future CO_2 emissions that will result from implementing new carbon restriction policies. As such, it was found, that reducing power sector emissions by 25% will go a long way towards limiting the 2° C temperature change. In other words, power sector reform is pivotal in achieving this goal. There are questions, however, about who's responsibility it should it be to cut emissions.

The developing world is recognised as not yet having contributed significantly to cumulative CO_2 emissions and thus climate change. To illustrate, less than 25% of cumulative global emissions have been sourced from the developing world (Pegels, 2010). According to Botzen, Gowdy & van den Bergh (2008), the biggest contributors to cumulative CO2 emissions between the 1900 and 2008 are the US (48%), Western Europe (24%), China (16%), Japan (7%) and India (5%). However, it is predicted that China's and India's cumulative emissions will exceed those of the higher emitters after 2021. Africa is not expected to overtake the US or Europe with regard to cumulative emissions until 2080 (Botzen, Gowdy & van den Bergh, 2008), but population and energy demand are expected to grow by about 80% by 2040. To meet these growing energy needs, electricity generation capacity is projected to quadruple (IEA, 2014).

Although developing regions are not as responsible for the cumulative contribution towards carbon emissions, Africa will experience disproportionately large climate changes compared to the rest of the developing world. According to the IPCC (IPCC, 2011), the temperature increases of the 21st century in Africa are expected to rise more rapidly than the global average and – also, rainfall averages are anticipated to drop for regions of northern and southern Africa

(Niang et al., 2014). In addition to affect that climate could have on rainfall patterns, the world has already has limited fresh water supplies as less than 1% of fresh water supplies are available for human consumption (Kumar & Tiwari, 2009). Furthermore, many surface fresh water sources are salinising (increasing in salt content) (Baldwin et al., 2006) and aquifer water levels are dropping (due to over consumption) (Tiwari & Tiwari, 2008).

These changes will bear significant consequence for Africa as it relies heavily on rainfall for agriculture. Furthermore, 62% of the population already lives below the poverty line (Niang et al., 2014) which contributes to a certain lack of adaptive capacity to future changes in the climate (Pegels, 2010) and water scarcity. In regions where the mean annual rainfall is becoming increasingly unpredictable, it is important that technology is used to bring water to crops in areas with unpredictable or scarce water supplies. Irrigation is a major step towards doing this in Africa (Fischer et al., 2007). To illustrate, irrigated crops often have yields that are twice as large as rain-fed crops (Fischer et al., 2007) and so irrigation will play a significant role in minimising future food shortages. According to the World Bank, agricultural losses in South Africa of up to 20% can be expected as a result of climate change (Pegels, 2010). While, as reported by Fischer et al. (2007), the need for increased irrigation due to climate change and standard socio-economic development are similar. This indicates how necessary irrigation will be for development in a future with increasingly unpredictable rainfall.

Solar pumping systems have emerged as a promising way of extracting water from the ground for domestic use or crop irrigation purposes. This type of pumping system is advantageous in remote areas where fuel supplies are limited (Bakelli, Arab & Azoui, 2011). Furthermore, solar pumping systems have an advantage over other systems in that they require little maintenance, they are easily installed, and they are reliable. Additionally, peak power production coincides well with peak water demand use due to the correlation between higher radiation values and greater water demand (Hamrouni, Jraidi & Chérif, 2009) et al. 2009). Furthermore, water tanks can be used as a storage mechanism instead of battery packs to allow for water availability when the sun does not shine (Bakelli, Arab & Azoui, 2011). Finally, there are environmental advantages in that PV systems do not release pollutants and run quietly compared to diesel pumps (Jafar, 2000).

Two solutions for fresh water provision exist. The first is to pump water from deeper sources and the second is to desalinate water. Pumping is a much more efficient form of water provision compared to distillation. For instance, considering the distillation form of desalination, the

evaporation of water requires 2260kJkg^{-1} of energy, but pumping at a head of 20m would only require 0.2kJkg^{-1}of energy. In a situation where pumping is an option, pumped systems should, therefore, be favoured, but in other cases, desalination should be considered as a source for fresh water (Tiwari & Tiwari, 2008).

Many countries rely on oil to drive desalination processes and provide fresh water. Desalination has become of increasing importance in regions where renewable fresh water supplies are exceeded (Khawaji, Kutubkhanah & Wie, 2008). The Gulf Corporation Council (GCC), which is comprised of six countries (Saudi Arabia, Oman, UAE, Kuwait, Bahrain and Qatar) relies significantly on energy intensive desalination processes to provide fresh water. Furthermore, more than 65% of the world's desalination processes take place in this region (Khawaji, Kutubkhanah & Wie, 2008).

Countries in the GCC currently rely mostly on thermal desalination processes such as MSF (Multi Stage Flash Distillation) and MED (Multiple Effect Distillation) (Dawoud, 2005). Of these technologies, MSF currently dominates current desalination capacity (61.6% of total capacity) but other technologies are increasing their own share of capacity (Khawaji, Kutubkhanah & Wie, 2008). These large-scale desalination projects tend to focus on supplying water to densely populated areas and neglect to provide small and poor communities with their water requirements (Mathioulakis, Belessiotis & Delyannis, 2007). One way of meeting the water needs of distributed communities is through solar distillation with solar stills. This process is discussed in Section 1.3.

1.2.2 Energy Access

Around the world, many large communities still lack access to electricity. For example, in developing Asia, about 19% of the population does not have access to electricity, while in Africa, this figure sits at about 58% (IEA, 2011a). Access to electricity can mean access to valuable services. For example, communication is improved with access to mobile networks. In addition, education opportunities arise with access to electricity since access implies better lighting, more time and surplus income to devote towards education and access to computers and the internet (Karekezi et al., 2012). All these opportunities work together to create an

environment that is more conducive to local business development and thus generalised economic growth (Kanagawa & Nakata, 2008).

Universal access to electricity has been challenging in South Africa. Although this has been a goal, a backlog of connections creates a required electrification rate that well exceeds the current funding and capacity constraints. In addition, universal electrification has referred to 100% of households existing at the time of the goal and so numbers do not incorporate the emergence of new households (Tait, Merven & Senatla, 2013). Furthermore, for households connected to the municipal electricity grid, there is a growing distrust in the reliability of centralised electricity provision. South Africa's utility (Eskom) has a supply grid that has recently been running under strain, with intermittent load-shedding, and it is expected to run this way until 2023 due to coal supply issues, skills and experience shortages and a lack of adequate funds (Odendaal, 2015, June 2). As such, distributed renewable energy solutions have emerged as an alternative to reliance on an unstable grid.

1.3 Hybrid Photovoltaic Thermal Desalination

The proliferation of renewable energy technologies (henceforth referred to as renewables), particularly solar powered photovoltaic (PV) generation, holds the potential for diminishing the dependency on fossil fuels. According to the International Energy Agency (IEA), renewables will account for about half of new global electricity production by 2040. Of this, wind, hydro and solar energy generation will have the largest shares, at 34%, 30% and 18% respectively (IEA, 2014). In addition, it is reported that the technical potential of direct solar radiation as a means of primary energy far exceeds the potential of other renewable sources (such as hydro, geothermal, biomass etc.) (IPCC, 2011). For this reason, PV systems are esteemed as a technology that holds some of the greatest potential for future energy generation.

However, despite the potential for solar energy production, low PV generation efficiency is a major drawback of this source of energy. One of the reasons why PV systems are inefficient is because about 80% of incident energy, which is not all converted to electrical energy, is lost to the surroundings (Huang et al., 2001). As a result, Photovoltaic Thermal (PV/T) systems have emerged as a way of enhancing the overall efficiency of PV panels. These systems remove unwanted heat from panels through a heat exchange process with fluids such as water (in the

case of high radiation, high ambient temperature environments) or air (in the case of low radiation and low-temperature environments) (Zondag et al., 2003). The derived useful thermal energy from these systems means that they have an overall energy production that is higher per unit area than separate PV and solar collector systems (Zakharchenko et al., 2004; Fraisse, Ménézo & Johannes, 2007). Furthermore, such systems require less construction material than separate PV and solar collector systems (Fraisse, Ménézo & Johannes, 2007).

One common type of PV/T system is a Sheet-and-Tube PV/T collector with one cover. This kind of system is common because it has adequate electrical and thermal efficiencies and because it is easy to manufacture (Charalambous et al., 2007). The side view of this type of system is shown in Figure 1.1. As can be seen from this figure, heat enters the system by radiation incident on the glass cover and on the panels. Heat then proceeds to flow towards the water by traversing through the PV panel, adhesive absorber and tube. One useful application of the heated water from the tube is to use it to aid the desalination process in solar stills.

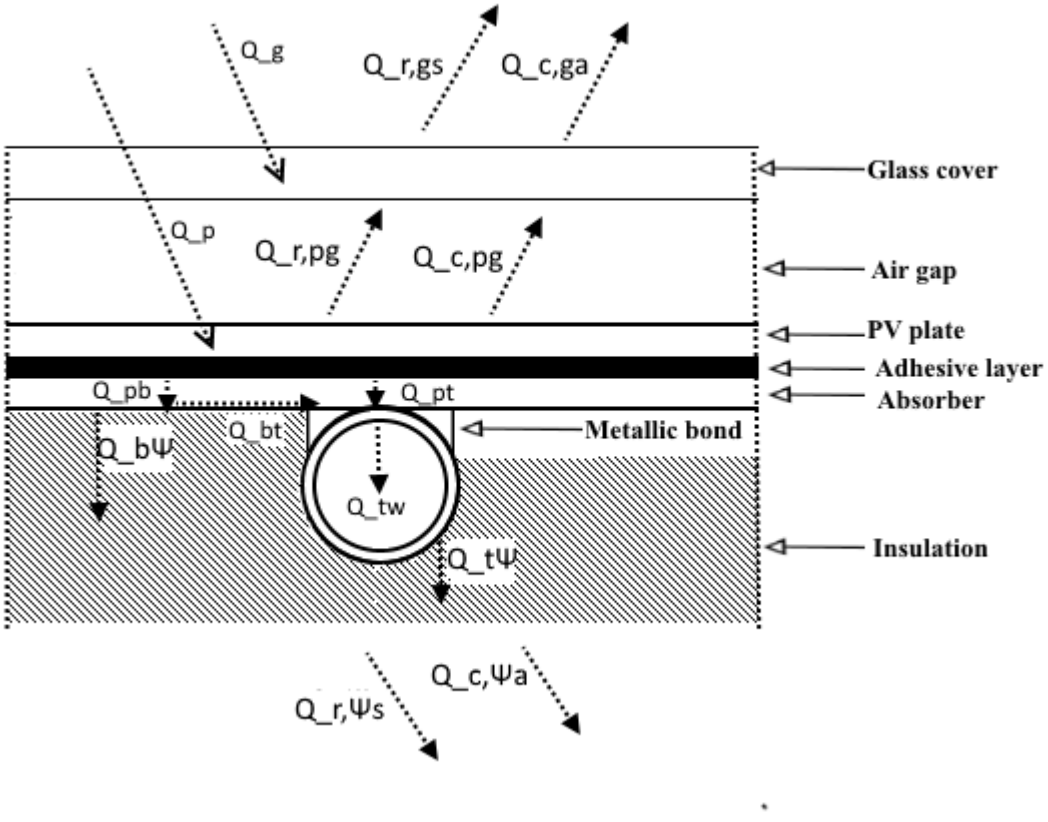

Figure 1.1: Sheet-and-Tube PV/T system (side view)

Solar distillation is the oldest form of desalination and such systems utilise the greenhouse effect to evaporate clean water from brine solutions and provide a fresh water yield (Kumar & Tiwari, 2009). Such a system, which is shown Figure 1.2, conventionally consists of a chamber with a thin layer or saline water in a basin. The top of the chamber is a single or double layer of sloped transparent film which allows incident solar radiation into it to heat the basin water. Some of the heated water then evaporates and forms water vapour in the chamber. This vapour rises and condenses as it comes into contact with the inclined transparent cover. The Freshwater distillate is then funnelled to a collection tray (Madhlopa & Clarke, 2013) to provide about 2 to 4 $lm^{-2}day^{-1}$ (Kumar & Tiwari, 2009). Heat transfer between the water and the cover of the solar still takes place in the form of convection ($q_{c,wk}$), radiation ($q_{r,wk}$), and evaporation ($q_{e,wk}$), with the magnitude of the evaporative heat transfer coefficient ultimately determining the extent of the system's water yield. This heat transfer coefficient is largely dependent on the temperature difference between the still's water and the condensing surface with both of these surfaces themselves having their temperatures influenced by the extent to which radiative, convective and heat transfer occurs within the system and by how much incident radiation is absorbed (Madhlopa, 2009). Wind speed and ambient temperature also affect the systems heat transfer coefficients and so affect the system yield (Al-Hinai, Al-Nassri & Jubran, 2002).

As the water yield of solar stills is largely dependent on the temperature difference between the water in the still and the cover of the still (Madhlopa, 2009), solar stills can utilise the waste heat from PV panels to increase the yields of solar stills (Kumar & Tiwari, 2008a). The resulting systems are henceforth referred to as hybrid PV/T desalination systems.

Waste heat from PV panels can be removed and used to aid the evaporation process in solar stills. Such systems are called hybrid PV/T desalination systems (illustrated in Figure 1.3 and Figure 3.5). In such systems, water is pumped (or circulated naturally) into a distillation chamber from the PV panels. The heat from the water from the PV panel enhances the amount of incident energy in the basin. However, as discusses (Section 2.3.3), the efficiency of the PV panels is reduced with higher temperatures, and heat removal is enhanced with a higher temperature differential between the water in the tube and the panels (See (2.54)). Thus, heating the water from the PV panel and collector configuration further does not enhance the panel's electrical efficiency. Nonetheless, hybrid PV/T desalination systems provide a use for otherwise wasted heat from the panels (Erdil, Ilkan & Egelioglu, 2008) and as such, these systems offer improved water yields over standalone solar stills. These higher water yields, in

parallel to electrical energy yields, may be important for remote locations (Kumar & Tiwari, 2008a).

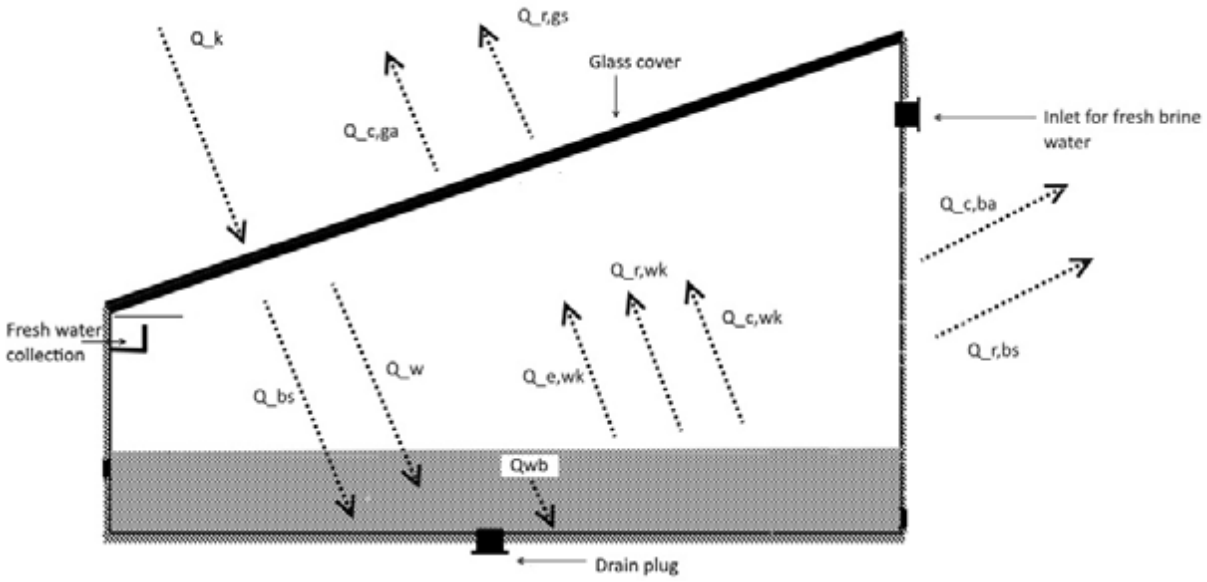

Figure 1.2: Simple solar sill

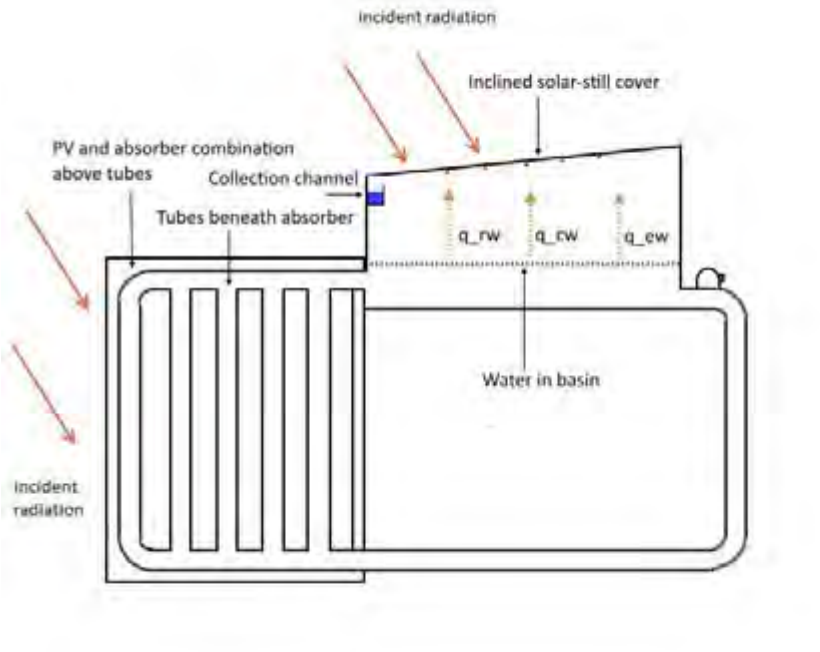

Figure 1.3: Basic hybrid PV/T desalination system configuration

1.4 Hybrid Photovoltaic Thermal Desalination Modelling

Numerical modelling is perceived to be a useful tool for optimising the designs of hybrid PV/T desalination systems as solar still models have helped determine optimal operational parameters for experimental setups (Al-Hinai, Al-Nassri & Jubran, 2002). Models, however, have varying degrees of accuracy (Tripathi & Tiwari, 2004; Tiwari & Tiwari, 2007b) and so require validation to determine the accuracy of a model.

In order for these models to predict the water yield of a system, heat transfer within the solar still needs to be determined as accurately as possible. The internal radiative heat transfer coefficient ($h_{r,wk}$) is one of these coefficients, which can be calculated using the view factor of the water in the basin (El-Maghlany, El-Samadony & Kabeel, 2015). The view factor incorporates the geometry of the basin into the determination of the internal radiative heat transfer coefficient. More specifically, the factor accounts for the fact that not all radiative heat exchange occurs between the still's water and the cover of the still as some radiative heat exchange occurs between the water in the still and the walls of the still (Madhlopa, 2014).

1.5 Problem Statement

Previous research into solar still modelling has undertaken various sensitivity studies to determine optimal operating parameters such as basin area (El-Sebaii, 1998), cover inclination (Tiwari & Tiwari, 2007a), basin insulation thickness (Al-Hinai, Al-Nassri & Jubran, 2002) etc. Studies have also been undertaken to determine the effect that ambient temperature and wind speed have on still yield (Al-Hinai, Al-Nassri & Jubran, 2002). With regard to model performance, one study examined the effect that accounting for the view factor in a solar still had on model accuracy (Madhlopa, 2014) and one study examined how this accuracy changes for different cover inclinations (El-Maghlany, El-Samadony & Kabeel, 2015).

More specifically, with regard to hybrid PV/T desalination systems, studies have modelled the performance of active (pumped) and passive (thermos-syphoned) systems at varying still water depth (Kumar & Tiwari, 2008a) and examined the payback periods between active and passive systems (Kumar & Tiwari, 2009). However, no work has been found which deals exclusively with incorporating view factors into hybrid PV/T desalination models. Furthermore, accounting for the view factor in solar still models has resulted in improved the model performance of solar still models (Madhlopa, 2014; El-Maghlany, El-Samadony & Kabeel, 2015) and therefore it is possible that the performance of hybrid PV/T desalination models could be improved upon by likewise incorporating this factor into a model.

1.6 Aim and Objectives

The aim of this study was to construct a numerical model of a hybrid PV/T desalination system and determine its accuracy.

The following objectives for this thesis were formulated:

1) Design a hybrid PV/T desalination system
2) Create a mathematical model for the system and implement it
3) Validate the model against experimental data
4) Run sensitivity analyses for a specific site in Stellenbosch, South Africa (33.935°S 18.7817°W).

1.7 Scope

The design was undertaken using a common type of PV/T system design (tube-and-sheet) with the entire hybrid PV/T desalination system being similar to existing designs (Kumar & Tiwari, 2010). Additionally, modelling equations common to literature are used (Chow, 2003). For this reason, it is expected that the findings of the validation part of this thesis are generalisable to hybrid PV/T desalination systems of a similar design.

The sensitivity analyses part of this thesis was performed at a specific location in South Africa. As such, the findings of optimal performance parameters may not be directly applicable to different climatic conditions or locations.

1.8 Thesis Outline

Chapter 2 of this thesis examines relevant literature. This includes a description of important concepts such as solar radiation, heat transfer, photovoltaics and PV/T systems. Chapter 3 outlines the thesis' methodology. This includes the design of a hybrid PV/T desalination system, the mathematical model used to simulate the system, the model validation parameters and relevant statistical tools, and a discussion of how the validation and the sensitivity analyses results were obtained. Chapter 4 presents the results and discussions for model validation, an annual run for a default parameter case and for sensitivity analyses. Finally, Chapter 5 provides conclusions and it makes recommendations for future work.

2 Literature Review

2.1 Introduction

This chapter starts by examining relevant topics related to solar radiation (Section 2.2). These include a definition of radiation terms, a discussion of how terrestrial radiation can be estimated as a function of extra-terrestrial radiation and a review of the equations that govern the absorption of radiation on tilted surfaces. Following this, a discussion of solar photovoltaics is given (Section 2.3), which includes the topics of materials, the photovoltaic effect and cell performance. Next, PV/T systems are discussed (Section 2.4), with reference to heat removal, solar still and hybrid PV/T desalination studies and efficiency calculations. Following this, the modelling is discussed (Section 2.5) with regard to model order and dynamic/steady-state modelling. Finally, the software considerations made for this project are then discussed (Note: Basic heat transfer principles, namely, conduction, convection and radiation are discussed in Appendix A and types of solar cells and their associated efficiencies are discussed in Appendix B.)

2.2 Solar Radiation

2.2.1 Introduction to Solar Radiation

This study requires a definition of solar terminology, and as such, some of these terms are defined in the bullet points below. Following this, extra-terrestrial radiation, and Global Horizontal Irradiance (GHI) then are defined.

- Solar time is a time system contingent on the fact that noon is achieved only when the sun is exactly at its highest point (solar noon). This solar noon thus implies an equal division of daylight hours on either side of this time (Tiwari & Tiwari, 2008).
- The Surface Azimuth Angle (γ) is the angular deviation of the horizontal-plane-projection of the surface from the local meridian (Duffie & Beckman, 2013). See Figure 2.1.

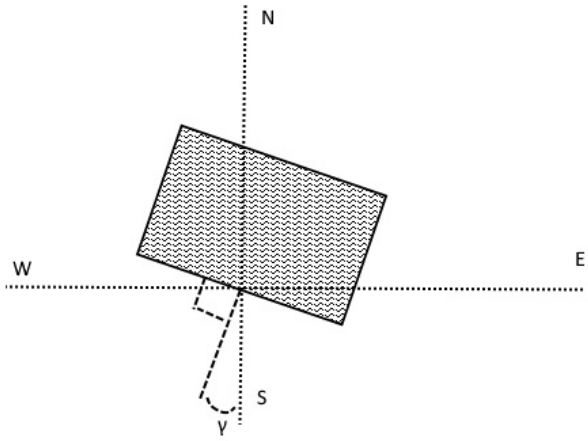

Figure 2.1: Azimuth angle illustration

- Declination (ζ) is the angle of the sun at solar noon, with reference to the equatorial plane (North is positive). The angle of declination sits at 0° at Equinox and ranges up to 23.5° depending on where the earth is on its orbital path (Myers, 2013). This maximum angle corresponds to the tilt angle of the earth. In summer, the sun reaches higher declinations in the sky, and thus its light is distributed across less surface area making more energy available per unit area (IEA, 2011b).
- Irradiance is the power flux of radiation received from the sun (Wm^{-2}) (Duffie & Beckman, 2013).
- Irradiation ($kWhm^{-2}$) is the energy flux of radiation received from the sun at some time interval. It is found by integrating irradiance for a specified time interval (Duffie & Beckman, 2013).
- Diffuse Radiation is radiation that received from the sun after being scattered by the earth's atmosphere (Myers, 2013). That is, its original direction of travel has been altered (Duffie & Beckman, 2013) (See Figure 2.2).
- Beam Radiation is radiation that has not been scattered and it's direction of travel remains unaltered by the earth's atmosphere (Duffie & Beckman, 2013) (See Figure 2.2).
- Global Radiation is the total combination of both diffused and beam radiation components (Duffie & Beckman, 2013).

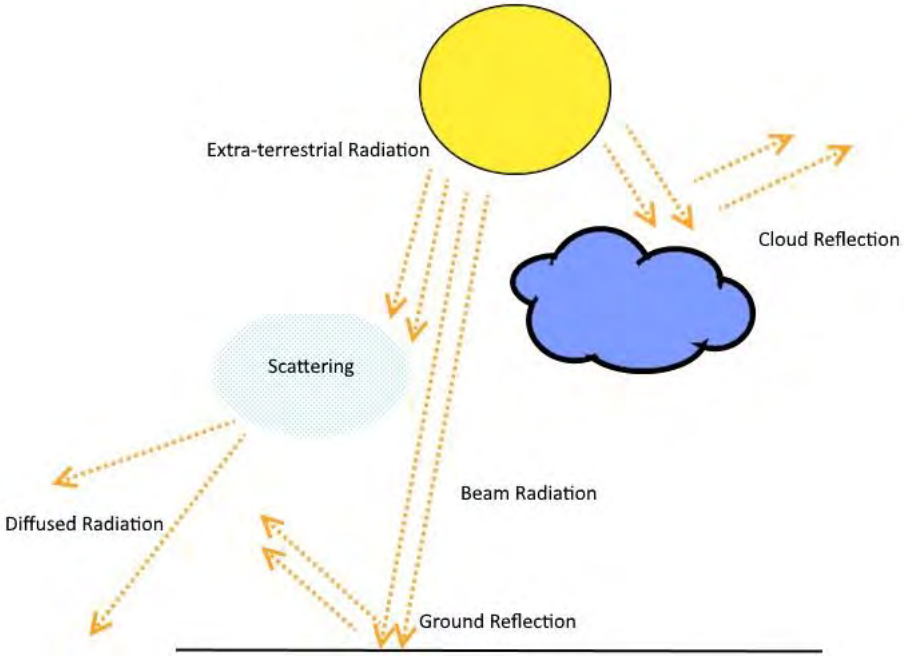

Figure 2.2: Components of radiation

- The angle of incidence (θ), is the angle beam radiation and the normal of a receiving surface (Duffie & Beckman, 2013) (See Figure 2.3).
- The Zenith Angle (θ_z) is the angle between the normal from the earth's surface and the line towards the sun (Duffie & Beckman, 2013). See Figure 2.3.

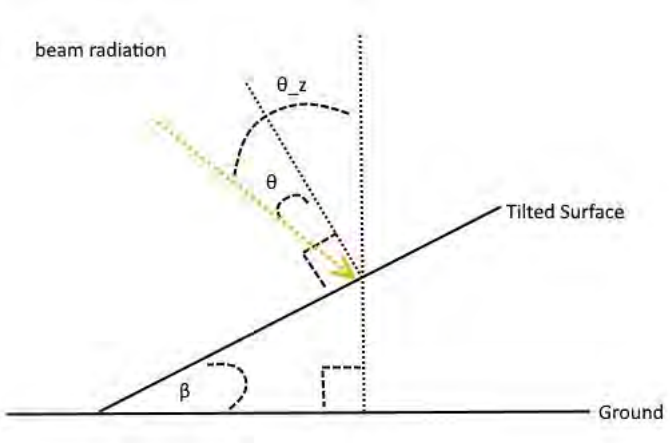

Figure 2.3: Illustration of solar angles (incidence, zenith and surface tilt)

- The hour angle(ω) is an indication of how far the angle of the sun is from being at solar noon (east or west of the local meridian). Each hour is represented by 15° and morning

angles are referenced as negative, afternoon angles as positive (Duffie & Beckman, 2013).

Extra-terrestrial radiation (G_{on}) from the sun is measured above the earth's atmosphere (See Figure 2.2) and it is measured per unit area perpendicular to the sun's rays. However, this value is not constant as the amount of radiation reaching the earth's atmosphere varies because the earth orbits the sun in an elliptical manner. To account for this variation in radiation, radiation can be modelled using (2.1) (Tiwari & Tiwari, 2008; Duffie & Beckman, 2013). In this equation, G_{sc} is the solar constant, which is available radiation at a mean distance from the sun (1367 Wm^{-2}) and B is given by Eq. (2.2).

$$G_{on} = G_{sc}(1.000110 + 0.034221\cos B + 0.001280\sin B + 0.000719\cos 2B + 0.000077\sin 2B) \quad (2.1)$$

$$B = (n - 1)\frac{360}{365} \quad (2.2)$$

Radiation received by the earth's surface can be divided into both beam and diffused components (as discussed). These components can be combined to give a total indication of the amount of radiation available on a horizontal surface. This total is called Global Horizontal Irradiance (GHI) and can be written in terms of the zenith angle, beam and diffused radiation as shown by Eq. (2.3) (Tiwari & Tiwari, 2008).

$$G_G = G_B \cos\theta_z + G_d \quad (2.3)$$

2.2.2 Radiation Attenuation in the Atmosphere

At sea level sunlight can provide approximately 1000Wm^{-2} (Tilley, 2013). As shown by Eq. (2.1), available irradiance at the extra-terrestrial level is a function of the solar constant. The

discrepancy between the arriving radiation on the horizontal plane and extra-terrestrial radiation is due to atmospheric absorption and scattering. This section discusses how wavelengths of light are affected by different particles and presents equations for estimating the amount of available beam and diffused radiation available at the earth's surface (Tiwari & Tiwari, 2008).

Of all arriving energy, about 8.73% of it is contained in the ultraviolet region ($\lambda < 0.4\mu m$), 38.15% in the visible region ($0.4\mu m < \lambda < 0.7\mu m$) and 53.12% is in the infrared region ($\lambda > 0.7\mu m$). Water vapour is responsible for absorbing most of the ultraviolet and infrared radiation in the more extreme wavelength ranges ($\lambda < 0.4\mu m$ and $\lambda > 2.3\mu m$ respectively) while nitrogen, oxygen and other gases absorb the extreme ranges of ultraviolet light and X-rays (Tiwari & Tiwari, 2008).

The total arriving beam radiation can be estimated according to Eq. (2.4). This equation depends on the atmospheric air mass above the point of interest, the Rayleigh scattering optical thickness of the atmosphere (ε), the Linke Turbidity factor (T_r) and a constant that determines the attenuation of direct radiation due to cloudiness or haziness (α). The derivation of the mass term and its relating variables is shown by Eqs. (2.6) to (2.9) as they are illustrative of how the azimuth angle and height affect the air mass the beam needs to traverse through. The scattering optical thickness, ε, is related to the air mass as shown by Eq. (2.5)(Tiwari & Tiwari, 2008).

$$G_B = G_{on} e^{-(M_a \varepsilon T_r + \alpha) cos\theta_z} \tag{2.4}$$

$$\varepsilon = 5.529 \times 10^{-4} {M_a}^2 - 9.66865 \times 10^{-3} M_a + 0.108014 \tag{2.5}$$

The Linke factor (T_r) by Eq. (2.4) is a spectrally integrated indicator of the attenuation. This attenuation is due to atmospheric pollution and the presence of gaseous water vapour. A study by Chaâbane, Masmoudi & Medhioub (2004) indicates that this factor varies throughout the seasons and at different times of the day. This fluctuation is due to winds that either carry in additional vapour content from the ocean air, dust content from land, or the times of rush-hour traffic (there are increased emissions at these times). For the African region, this factor is said to show little variation around the Mediterranean basin (T_r values of about 3.5 are found). However, for the subtropical South-Eastern parts of the continent, monthly variation is large.

For example, T_r values for Lusaka, Zambia, vary from 2.5 to 7.0 throughout the year (Diabate, Remund & Wald, 2003).

The mass of air that needs to be traversed by radiation affects the amount of radiation that reaches the earth due to scattering. The minimum amount of air mass to be traversed is the horizontal slab drawn perpendicularly from the earth to the sun. This air mass is allocated a length of 1 unit as it is the shortest possible length that can be travelled by the sun's rays. To account for different air masses, the zenith angle can be used to calculate the relative distance radiation has to travel along the hypotenuse (Myers, 2013).

$$M_a = \frac{1}{cos(\theta_z)} \tag{2.6}$$

This equation needs to be extended to account for the refraction that takes place between space and the atmosphere and the air pressure differences that affect the equivalent air mass length. The refraction angle only needs to be accounted for at zenith angle larger than 70°, such as at sunrise and sunset. To account for this angle, Eq. (2.7) can be used to calculate a more accurate effective air mass length using the zenith angle. To extend this to account for air pressure, Eq. (2.8) can be used to calculate the approximate air pressure at different heights (Z) above sea level. This pressure can then be used in conjunction with calculated refraction-corrected air mass (Eq. (2.7) to account for the influence of pressure differences and the effective air-mass-length as is shown by Eq. (2.9) (Myers, 2013).

$$M_r = \frac{1}{\cos(\theta_z) + 0.50572(96.07995 - \theta_z)^{-1.6364}} \tag{2.7}$$

$$P_z = P_o\, e^{-0.000832\, Z} \tag{2.8}$$

$$M_{rz} = M_r \frac{P_z}{P_o} \tag{2.9}$$

The diffused radiation estimate at ground level is written as a function of the normal irradiance at ground level (G_n), the extra-terrestrial irradiance (G_{on}) and the zenith angle,θ_z. In addition, two additional factors are introduced. The first factor (K_1), is referred to as a Perturbation Factor and indicates the extent to which a beam scatters though a lumped piece of atmosphere. The second term (K_2) is referred to as Background Diffuse Radiation (Tiwari & Tiwari, 2008). These parameters can be defined for a specific region using regression analysis (Singh & Tiwari, 2005).

$$G_d = K_1(G_{on} - G_n)\cos\theta_z + K_2 \quad (2.10)$$

The performance of PV panels is largely determined by how much radiation is received by each panel. The optimal amount of radiation is received when the sun's rays arrive perpendicularly to the surface of the panel (Kacira et al., 2004). Ideally, this can be achieved by using a tracking system, which is a mechanical mechanism that allows panels to track the path of the sun. However, these systems add additional upfront cost to PV projects, and so fixed optimal tilt is often used (Mehleri et al., 2010). These optimal tilt angles are discussed in Section 3.2.1.2. As radiation is often measured in the horizontal plane, to determine available radiation on a tilted surface, a conversion model is needed. This model is given in Section 2.2.3.1.

2.2.3 Radiation Absorption

2.2.3.1 Glass

The radiation that is absorbed by the glass (Q_g) is given by Eq. (2.11) (Chow, 2003). This equation depends on the absorptivity of glass (α_g) and tilted irradiance (G_t). The derivation of the absorptivity term is first given, followed later by the derivation of the radiation component (G_t) (Eq. (2.27)).

$$Q_g = G_t \alpha_g \tag{2.11}$$

The absorptance of the glass (α_g) is found by averaging the perpendicular and parallel components of absorptance ($\alpha_\perp$ and $\alpha_\parallel$) as shown by Eq. (2.12). These components, which are functions of perpendicular reflectivity and parallel reflectivity ($r_\perp$ and $r_\parallel$) respectively, are given by Eqs. (2.13) and (2.14) accordingly. In these equations, the parallel and perpendicular components of reflectance are required, and so defined by Eqs. (2.15) and (2.16) respectively (Duffie & Beckman, 2013).

$$\alpha_g = \frac{\alpha_\perp + \alpha_\parallel}{2} \tag{2.12}$$

$$\alpha_\perp = (1 - \tau_g)\left(\frac{1 - r_\perp}{1 - r_\perp \tau_g}\right) \tag{2.13}$$

$$\alpha_\parallel = (1 - \tau_a)\left(\frac{1 - r_\parallel}{1 - r_\parallel \tau_a}\right) \tag{2.14}$$

$$r_\perp = \frac{sin^2(\Upsilon - \theta)}{sin^2(\Upsilon + \theta)} \tag{2.15}$$

$$r_\parallel = \frac{tan^2(\Upsilon - \theta)}{tan^2(\Upsilon + \theta)} \tag{2.16}$$

To calculate the perpendicular and parallel components of reflectance (Eqs. (2.15) and (2.16)), the incidence (θ) and the refraction angles (Υ) need to be found. The angle of incidence is calculated later by Eq. (2.19) and Υ is derived from Snells law (Eq. (2.17) using the refractive indices of air and glass (n_1 and n_2) and the angle of incidence (Serway & Jewett, 2004).

$$n_a sin\theta = n_g sin\Upsilon \tag{2.17}$$

The transmittance of glass (τ_g) in Eqs. (2.13) and (2.14) considers the absorptance losses and depends on the angle of incident solar radiation. Transmittance can be calculated according to Bouguers Law which is given by Eq. (2.18)(Duffie & Beckman, 2013). In this equation, δ_g is the thickness of the glass and Λ is the excitation coefficient. The angle of refraction (Υ) can be calculated from Snell's law as shown by Eq. (2.17). The derivation of the angle of incidence, required to calculate the perpendicular and parallel components of reflectivity (Eqs. (2.15) and (2.16)) and transmittance (Eq. (2.18)), is provided.

$$\tau_a = \exp\left(-\frac{\Lambda \delta_g}{cos\Upsilon}\right) \tag{2.18}$$

The angle of incidence is calculated from Eq. (2.19). This equation can be simplified by creating an artificial latitude, $(\Phi + \beta)$, and setting the tilt, β, to 0 radians (the tilt is now accounted for in the artificial latitude). Also, for an optimal orientation that maximises incident radiation in the southern hemisphere, where a North facing azimuth of 180° is used, this equation simplifies to Eq. (2.20) (Duffie & Beckman, 2013).

$$\begin{aligned} cos\theta = {} & \sin(\delta)\sin(\Phi)\cos(\beta) + \sin(\delta)\cos(\Phi)\sin(\beta)\cos(\gamma) \\ & + \cos(\delta)\cos(\Phi)\cos(\beta)\cos(\omega) + \cos(\delta)\sin(\Phi)\sin(\beta)\cos(\gamma)\cos(\omega) \\ & + \cos(\delta)\cos(\beta)\sin(\gamma)\sin(\omega) \end{aligned} \tag{2.19}$$

$$cos\theta = \cos(\delta)\cos(\Phi + \beta)\cos(\omega) + \sin(\delta)\sin(\Phi + \beta) \tag{2.20}$$

If a system is in the Northern hemisphere and radiation is to be maximised, the system should be set to face South (an azimuth of 0°). Doing this changes Eq. (2.19). to Eq.(2.21). This equation can now be rewritten to incorporate the artificial latitude with the new form of the equation being given by Eq. (2.22).

$$cos\theta = \sin(\delta)\sin(\Phi)\cos(\beta) + \sin(\delta)\cos(\Phi)\sin(\beta) + \cos(\delta)\cos(\Phi)\cos(\beta)\cos(\omega) + \cos(\delta)\sin(\Phi)\sin(\beta)\cos(\omega) \quad (2.21)$$

$$cos\theta = \sin(\delta)\sin(\Phi-\beta) + \cos(\delta)\cos(\Phi-\beta)\cos(\omega) \quad (2.22)$$

Eqs. (2.20) and (2.22), which provide the angle of incidence, are contingent on many variables. The first variable is declination (ζ), which is defined by Eq.(2.23)(Duffie & Beckman, 2013). The angle B is defined by Eq. (2.2).

$$\zeta = 0.006918 - 0.399912\cos B + 0.070257\sin B - 0.006758\cos 2B + 0.000907\sin 2B - 0.002697\cos 3B + 0.00148\sin 3B \quad (2.23)$$

The hour angle (ω) in Eqs. (2.20) and (2.22) is given by Eq. (2.24) (Tiwari & Tiwari, 2008; Duffie & Beckman, 2013). In Eq. (2.24), the solar time (st) is given by Eq. (2.25). In Eq. (2.25) where L_{st}, is the standard meridian for the regional time zone (in 15° degree increments) and L_{loc} is the longitude of the system. Lastly, E is the correction factor that accounts for the variation in the earth's rotational rate and is given by Eq. (2.26) (Duffie & Beckman, 2013).

$$\omega = 15\pi(SolarTime/60 - 12)/180 \quad (2.24)$$

$$st = StdT + E + (L_{st} - L_{loc})/15 \quad (2.25)$$

$$E = 229.2(0.000075 + 0.001868cosB - 0.032077sinB - 0.014615cos2B - 0.04089sin2B) \quad (2.26)$$

The total tilted irradiance (G_t) is also a fundamental variable for the model as is seen in Equation (2.11). Tilted surface irradiance, by taking into account ground reflection, can be given by an anisotropic approximation shown by Eq. (2.27) (Duffie & Beckman, 2013). This approximation for total irradiance on a tilted surface includes the circumsolar and horizon

brightening components of diffused irradiance and it is called the Hay, Davies, Klucher, Reindl (HDKR) model (Duffie & Beckman, 2013). The circumsolar component accounts for the fact that there is a concentration of diffused radiation around beam radiation. That is to say, this radiation is not isotropic because it is directionally dependent. Horizontal brightening, on the other hand, accounts for the fact that on clear days there is a concentration of diffused radiation around the horizon (Myers, 2013).

$$G_t = (G_b + G_d A_i)R_b + G_d(1 - A_i)(\frac{1+\cos\beta}{2})\left[1 + \mathrm{f}sin^3(\frac{\beta}{2})\right] + (G_B + G_d)\frac{1+\cos\beta}{2}\ \rho_{gr} \quad (2.27)$$

The circumsolar irradiance component is included into Eq. (2.27) using the anisotropy index (A_i). This index determines the portion of diffused irradiance that should be reckoned as directionally dependent (On clearer days, this index is closer to one). The equation for this index, which is simply the ratio of measured beam irradiance to extra-terrestrial irradiance, is given by Eq. (2.28) (Duffie & Beckman, 2013). The horizontal brightening component, in Eq. (2.27), is introduced with the sine term. This term depends on the tilt angle of the surface (β) and the modulation factor (f), with the modulation factor being given by Eq. (2.29) (Duffie & Beckman, 2013).

$$A_i = \frac{G_B}{G_o} \quad (2.28)$$

$$f = \sqrt{\frac{G_b}{(G_B + G_d)}} \quad (2.29)$$

In Eq. (2.27), G_B and G_d are the horizontal beam and diffused radiation components respectively. The ground reflectance factor (ρ_{gr}) depends on the geometry of the site (See Figure 2.2). R_b is the geometric coefficient and indicates the portion of beam radiation on the tilted surface compared to a horizontal surface. This ratio can be calculated by comparing the angle of incidence on a horizontal and a tilted surface as shown by Eq. (2.30) (Duffie & Beckman, 2013).

$$R_b = \begin{Bmatrix} \dfrac{\cos(\phi+\beta)\,cos\delta cos\omega + \sin(\phi+\beta)\,sin\delta}{\cos(\phi)\,cos\delta cos\omega + \sin(\phi)\,sin\delta}, & for\ \gamma = 180° \\ \dfrac{\cos(\phi-\beta)\,cos\delta cos\omega + \sin(\phi-\beta)\,sin\delta}{\cos(\phi)\,cos\delta cos\omega + \sin(\phi)\,sin\delta}, & for\ \gamma = 0° \end{Bmatrix} \quad (2.30)$$

$R_b$in Eq. (2.30), which is simply the ratio of the cosine function of the angle of incidence on tilted surfaces to cosine function of the angle of incidence on horizontal surfaces, tend towards infinity as the zenith angle approaches 90° (i.e. at sunset and sunrise).To avoid having sunset and sunrise zenith hours give distorted R_b values, it is necessary to average out the $R_b$values around sunset and sunrise hours instead of calculating R_b values at particular hour midpoints.

This averaging out is performed using Eqs. (2.31), (2.32) and (2.33). In these equations, ω_1 and ω_2 represent one of two different values depending on whether the average is being calculated for a sunrise or sunset hour. For sunrise, ω_1 represents the sunrise hour angle and ω_2 the hour angle for the nearest whole hour from sunrise (for example, if sunrise is at 6:45am, ω_1 is this hour angle and ω_2 is the hour angle of 7am). Similarly, for sunset, ω_1 represents the hour angle for the nearest whole hour before sunset and ω_2, the hour angle for sunset (Duffie & Beckman, 2013).

$$R_{b,average} = \frac{a}{b} \quad (2.31)$$

$$\begin{aligned} a = {} & (sin\delta sin\phi\cos\beta - sin\delta cos\phi sin\beta cos\gamma)(\omega_2 - \omega_1) \\ & + cos\delta cos\phi cos\beta + \cos\delta sin\phi sin\beta cos\gamma(sin\omega_2 - sin\omega_1) \\ & - cos\delta sin\beta sin\gamma(cos\omega_2 - cos\omega_1) \end{aligned} \quad (2.32)$$

$$b = (cos\phi cos\delta)(sin\omega_2 - \sin\omega_1) + sin\phi sin\phi(\omega_2 - \omega_1) \quad (2.33)$$

To find the values of ω_1 and ω_2, the sunset and sunrise hour angle, which are just negatives of each other for particular days, must be known. To attain the sunset/sunrise hour angle, the formula for the zenith angle must first be found (θ_z). This is derived by using the fact that the

zenith angle is equal to the angle of incidence on a horizontal surface (i.e. β=0) and so Eq. (2.20) is thus simplified to Eq. (2.34). Thereafter, by using the fact that the zenith angle (θ_z) is $\frac{\pi}{2}$ radians at sunrise and sunset, a value for the hour angle at these times can be found according to Eq. (2.35) (Markvart, 2000; Duffie & Beckman, 2013).

$$cos\theta_z = \sin(\delta)\sin(\Phi) - \cos(\delta)\cos(\Phi)\cos(\omega) \quad (2.34)$$

$$cos\ \omega = -tan\ (\Phi)\tan(\delta) \quad (2.35)$$

2.2.3.2 PV Panel/Collector

The amount of solar radiation absorbed by the panel and collector, (the panel is used in this discussion as a term of reference) can be calculated using Eq. (2.36), which was adapted (to account for different transmittance-absorptance coefficient components) from Chow (2003). This equation depends on the elements of tilted radiation (beam, diffused and ground) on the PV panel (given by Eq. (2.27)) and the effective absorptivity of each of the radiation components as defined by transmittance-absorptance coefficients $(\tau\alpha)_{B,}(\tau\alpha)_d$ and $(\tau\alpha)_g$ accordingly (Duffie & Beckman, 2013). Also in this equation is the electrical power output of the panel,E_p, which affects how much of the incident energy is converted to heat on the panel.

$$\mathrm{Q}_p = \mathrm{G}_b(\tau\alpha)_B + \mathrm{G}_d(\tau\alpha)_d + (\mathrm{G}_g)(\tau\alpha)_g - E_p \quad (2.36)$$

Conceptually, this equation represents what occurs after incident solar radiation has been transmitted through the glass. First, the radiation is reflected from the PV panel back towards the glass cover. It is then reflected back towards the PV panel by the glass surface with this process being repeated towards infinity, as illustrated in Figure 2.4. By summing the successive reflections of radiation in the system towards infinity, the transmittance-absorptance factor for beam radiation, $(\tau\alpha)_B$, diffused radiation , $(\tau\alpha)_d$, and ground reflected radiation,$(\tau\alpha)_g$, are attained. Eq. (2.37) provides an equation for this summation (Duffie & Beckman, 2013).

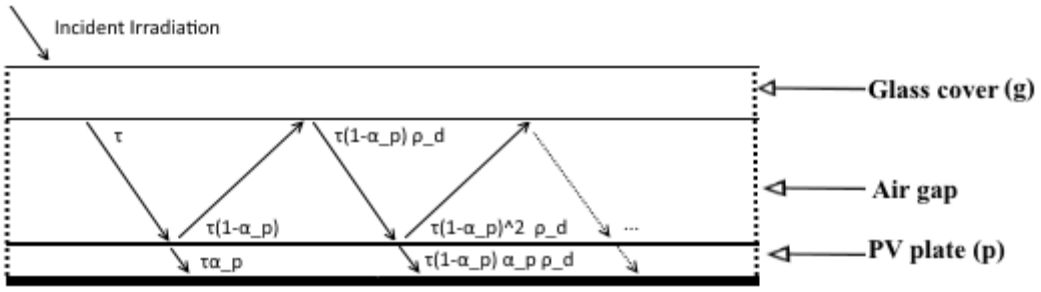

Figure 2.4: Absorption of solar radiation by PV panel under glass

Source: Adapted from Duffie & Beckman (2013)

$$(\tau\alpha) = \frac{\tau\alpha_p}{1-(1-\alpha_p)\rho_d} \tag{2.37}$$

In Eq. (2.36), the transmissivity of the glass (τ) is found by averaging the perpendicular (Eq. (2.39)) and horizontal (Eq. (2.40)) components of transmissivity as shown in (Eq. (2.38)). The reflectance components are provided for by Eqs. (2.15) and (2.16) and the absorptance component of transmission (τ_a) is given by Eq. (2.18) (Duffie & Beckman, 2013).

$$\tau = \frac{\tau_\perp + \tau_\parallel}{2} \tag{2.38}$$

$$\tau_\perp = \frac{\tau_a(1-r_\perp)^2}{1-(r_\perp\tau_a)^2} \tag{2.39}$$

$$\tau_\parallel = \frac{\tau_a(1-r_\parallel)^2}{1-(r_\parallel\tau_a)^2} \tag{2.40}$$

The diffused reflectance of the glass (ρ_d) is also present in the denominator of Eq. (2.37) because radiation being reflected from the inside of the glass cover is diffused in nature. To find this term, the average unpolarised diffused radiation is calculated according to Eq. (2.41)

. The perpendicular and horizontal components of reflectance ($\rho_\perp$ and $\rho_\parallel$) are provided for by Eqs. (2.42) and (2.43) respectively (Duffie & Beckman, 2013).

$$\rho_d = \frac{\rho_\perp + \rho_\parallel}{2} \tag{2.41}$$

$$\rho_\perp = r_\perp + r_\perp \frac{\tau_a^2(1-r_\perp)^2}{1-(r_\perp \tau_a)^2} \tag{2.42}$$

$$\rho_\parallel = r_\parallel + r_\parallel \frac{\tau_a^2(1-r_\parallel)^2}{1-(r_\parallel \tau_a)^2} \tag{2.43}$$

The components of diffused reflectance ($\rho_\perp$ and $\rho_\parallel$) consist of the polarised reflective components ($r_\perp$ and $r_\parallel$) (which are given by Eqs. (2.15) and (2.16)) and the absorptance component of transmission (τ_a) (Eq. (2.18)). All three equations for diffused reflectance depend on the angle of incidence. This angle differs from the angle used to calculate the transmissivity in the numerator in Eq. (2.37) as now diffused radiation is incident on the glass from beneath it. A set incidence angle of 60° may be used to account for the fact that the radiation is diffused (Duffie & Beckman, 2013).

The beam transmittance-absorptance coefficient ($(\tau\alpha)_B$) of Eq. (2.37) is calculated using the angle of incidence which is calculated using Eq. (2.20). On the other hand, the transmittance-absorptance coefficients for diffused $(\tau\alpha)_d$ and ground reflection $(\tau\alpha)_g$ are instead calculated with equivalent an angle of incidence. For diffused radiation, this coefficient is calculated according to Equation (2.44) and, for ground reflection radiation, according to Eq. (2.45) (Duffie & Beckman, 2013).

$$\theta_d = 59.7 - 0.1388\beta + 0.001497\beta^2 \tag{2.44}$$

$$\theta_{gr} = 90 - 0.5788\beta + 0.0026993\beta^2 \tag{2.45}$$

The electrical power component of Eq. (2.36) is defined by Eq. (2.46). This variable depends on tilted irradiance (G_t), the ratio of aperture area to cell area (r_c) and the efficiency of the cell (η_{sc}). The cell efficiency (η_{sc}), represented by Eq. (2.47) , depends on the temperature of the panel (T_p), the reference operating temperature (T_{ref}), the reference efficiency of the panel (η_{ref}) and on the efficiency temperature coefficient of the panel (β_{ref}) (Chow, 2003; Skoplaki, Boudouvis & Palyvos, 2008). β_{ref} is often provided by the manufacturer but can be calculated as shown in Eq.(2.48), where $T_{\eta=0}$ in this equation is the temperature of the panel that results in a panel efficiency of zero percent (Skoplaki & Palyvos, 2009).

$$E_p = \eta_{cc} r_c \left(G_b(\tau\alpha)_b + G_d(\tau\alpha)_d + (G_g)(\tau\alpha)_g\right) \quad (2.46)$$

$$\eta_{cc} = \eta_{ref}[1 - \beta_r(T_p - T_{ref})] \quad (2.47)$$

$$\beta_{ref} = \frac{1}{T_{\eta=0} - T_{ref}} \quad (2.48)$$

2.3 Solar Photovoltaics

2.3.1 Classes of Electric Materials

When discussing photovoltaics, there are three classes of materials that should be considered. The first is conductors, the second, semiconductors and the last insulators. Conductors allow charge to flow with minimal resistance, while semiconductors allow charge to flow with minimal resistance under specific conditions. Lastly, insulators inhibit the flow of charge.

In conductors, the outermost electrons do not remain fixed to individual atoms. Rather, they can move freely within the material. Conductors, such as copper, exhibit this property because they have their electrons in the lower levels of the valence band (highest band occupied by electrons). When a small electric field is applied, these electrons can reach many vacant levels higher in the band even if the provided energy is small (Halliday, Resnick & Walker, 1997). In contrast, insulators have their valence band entirely filled, and so the next vacant energy levels

lie within the conduction band. Thus, insulators require the provision of significant of levels energy for electrons to cross into the conduction band (Halliday, Resnick & Walker, 1997).

There is an additional class of materials which exhibits both properties of conductance and insulation. These materials are called semiconductors. The valence structure of semiconductors and insulators are the same. However, semiconductors require less energy to get an electron from the valence band to the conduction band. This is because the states adjacent to the filled valence band are not available in semi-conductors and insulators alike (Callister & Rethwisch, 2007). In this way, we say the Energy Gap or Band gap for semiconductors is smaller than that for insulators (Halliday, Resnick & Walker, 1997; Serway & Jewett, 2004; Callister & Rethwisch, 2007). The band gap energy required to elevate an electron to the conduction band is shown in Figure 2.5.

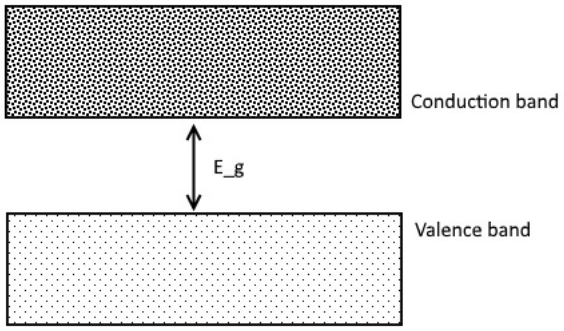

Figure 2.5: Energy gap

An interesting difference between conductors and semiconductors is the dependence of resistance on temperature. In conductors, the resistivity of a material rises as temperature rises. However, in semiconductors, the opposite is true. If the temperature of a material rises in a standard conductor, the average time between collisions goes down and the number of charge carriers stays roughly the same. Consequently, the total resistivity of the material goes up. However, if the temperature rises in a semiconductor, the number of charge carriers increases rapidly. The collision time, as for conductors, goes down in semiconductors but the increase in charge carriers overrides the effect of the reduced collision-time (Halliday, Resnick & Walker, 1997).

Pure semiconductors are called intrinsic semiconductors. This means that the semiconductor consists of only one element or compound. Such semiconductors have equal numbers of electrons and holes that can be used for conduction (Serway & Jewett, 2004; Callister & Rethwisch, 2007). Intrinsic semiconductors have a limited number of charge carriers, and so, to increase the number of available charge carriers, impurities are added (Hummel, 2011). This process is called 'doping' (Hummel, 2011), and materials that have been doped are called extrinsic semiconductors (Serway & Jewett, 2004). Two types of doping exist. The one exists for the formation of p-type and the other for n-type semiconductors (Hummel, 2011).

When a group IV semiconductor such as silicon has a material with five outer-shell electrons (P, As and Sb (Hummel, 2011) added to it, one electron is left over after the formation of covalent bonds. The resulting material has a 'free' electron that sits just below the conduction band, and the impurity that allows for this is called a 'donor' (Callister & Rethwisch, 2007). This type of material is termed an n-type semiconductor because the charge carriers are generally negatively charged electrons (Hummel, 2011).

If the process is repeated, but this time a substance with three outer-shell electrons (B, Al, Ga and In (Hummel, 2011) is added to a group IV semiconductor, an electron deficit occurs after the formation of covalent bonds within the semiconductor material. The deficit of each electron in a bond is called a hole. At room temperature electrons from covalent bonds can drift between bonds and fill these holes. The type of impurity that allows for this is known as an acceptor because it is able to accept electrons to fill a state (Callister & Rethwisch, 2007). As positively charged holes are main charge carriers in this type of material, it is termed, a p-type semiconductor (Serway & Jewett, 2004; Hummel, 2011).

These two types of semiconductors – p-type and n-type – can be made to form a junction diode. This is done by allowing impurities to diffuse through a piece of silicon. These impurities form the junction barrier at the point where they meet (Meyers & Myers, 1997). Effectively, free electrons from the n-type semiconductor are swept across to the p-type semiconductor where they combine with holes. One can consider the holes to have been swept across to the n-side (Da Rosa, 2009). As a result of this, there is a region that is established between the p-type and n-type with no mobile charge carriers. This region is termed a depletion region (Serway & Jewett, 2004). The portion of the depletion region on the n-type side is positively charged, and the p-type side of the depletion region is negatively charged (Markvart, 2000). As a result, an

electric field is set up which sweeps any remaining charge carriers out of the depletion region (Serway & Jewett, 2004).

2.3.2 Photovoltaic Effect

Electrons that have been excited to the conduction band can be moved by a driving electric field and, as such, sometimes recombine with holes. When an electron recombines with a hole, radiation with an energy relating to the band gap energy (E_g) is emitted in the form of a photon. This is essentially how light emitting diodes work. On the other hand, incident photons can also be absorbed by electrons. This energy can, if sufficient energy exists, elevate the electrons to the conduction band (Serway & Jewett, 2004). This process of absorption forms the basis of the photovoltaic effect.

Incident photons do one of three things when they come into contact with silicon semiconductor material. They either, pass through the silicon, reflect off the surface or, if they contain sufficient energy, they are absorbed. If absorption occurs, an electrical current may be induced in the material (Hersch & Zweibel, 1982; Chukwuka, 2013). If a photon is absorbed, sufficient energy may exist for electrons in the depletion region to leave the valence band to join the conduction band. Electrons that gain enough energy to jump to the conduction band are free to move, and thus there is an increase in the material's conductivity (Chukwuka, 2013; Tilley, 2013). If this happens on the n-side of the depletion region, the electric field across the junction causes these electrons to be swept across to the n-side of the material (Hummel, 2011). In a similar way, when photons are incident on the p-side of the depletion zone, normal electron-hole pairs are broken, and holes are swept across to the p-side of the semiconductor (Hersch & Zweibel, 1982; Hummel, 2011). When a load is connected between the p-side and n-side, electrons from n-side flow towards the p-side to fill holes and attain an equilibrium (Messenger & Venre, 2003). The build-up of charge on either side of the junction is illustrated in Figure 2.6. Several functions, however, limit the current-generating ability of solar cells.

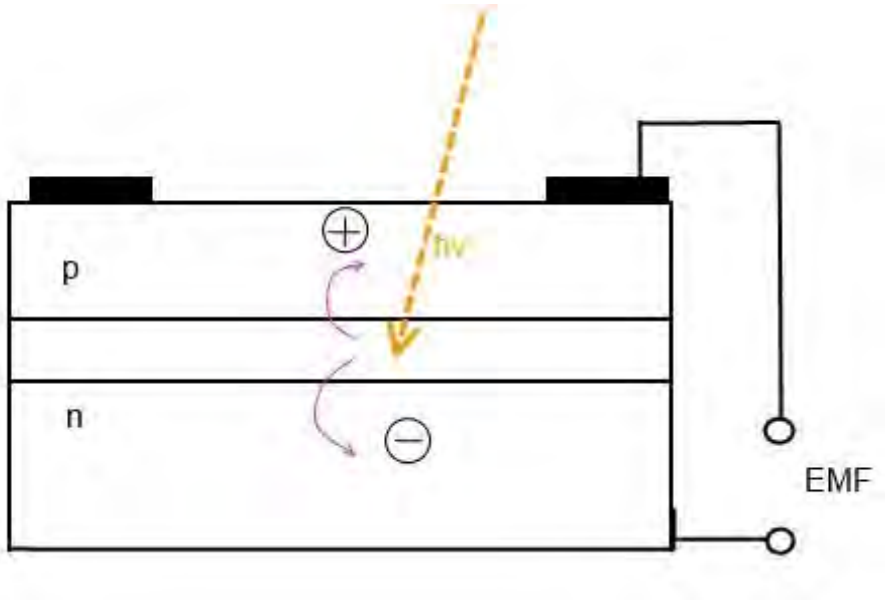

Figure 2.6: Generation of EMF due to incident photons

Source: Adapted from Hummel (2011)

The main factors that limit PV cell efficiency are surface-reflection (Furkan & Mehmet Emin, 2010), unmatched bandgap energy (Messenger & Venre, 2003), unwanted electron-hole recombination (Hummel, 2011), material electrical resistance and self-shading (Hummel, 2011). Each of these factors, which inhibit cell efficiency, is looked at in greater detail below.

The reflection of radiation from PV cells is one of the most significant losses that limits cell efficiency (Dobrzański & Drygała, 2008). Anti-reflective coatings, such as Silicon Monoxide (SiO), can be added to PV cells so that reflection losses are reduced (Messenger & Venre, 2003) or, alternatively, texturing techniques can be used to ensure than the surface of the cell has its own anti-reflective properties (Dobrzański & Drygała, 2008). Texturing can also be added to the cell's rear surface so that photons, which managed to pass through the silicon, have a higher probability of being reflected back into the cell where they are available for reabsorption purposes (Tilley, 2013). The use of coating and texturing to maximise the amount of radiation within solar cells is illustrated in Figure 2.7.

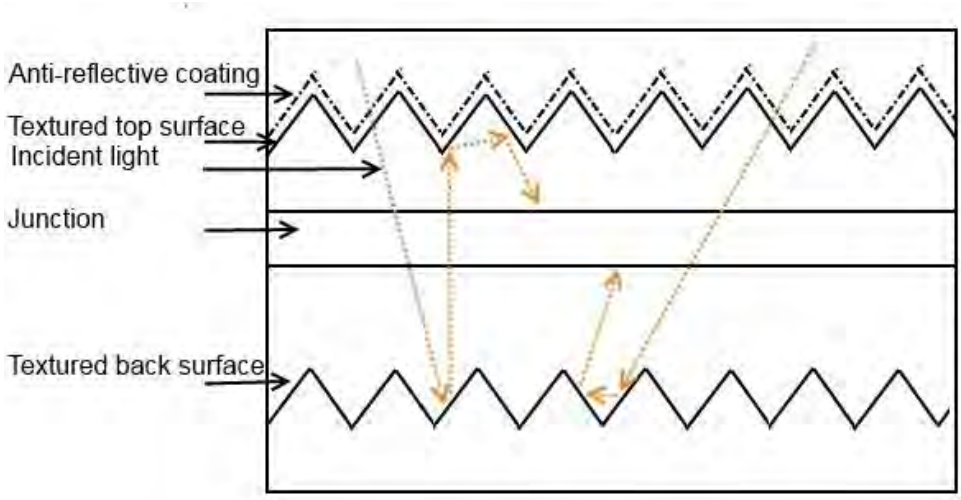

Figure 2.7: The use of coating and texturing for radiation retention

Source: Adapted from Messenger & Venre (2003)

Photons that are eventually absorbed by the cell do not have all of their energy converted into electrical energy. As discussed, the minimum energy required to elevate an electron to the conduction band is called the bandgap energy and the magnitude of this required energy depends on the material in use (Messenger & Venre, 2003). The frequency needed to raise an electron to the conduction band is represented by Eq. (2.49) as a function of the final (E_f) and initial (E_i) energy states. This frequency can then be related to the wavelength of light by Eq. (2.50) (Hersch & Zweibel, 1982; Serway & Jewett, 2004). When the energy of incoming photons does not exactly match the required energy for conduction band elevation, some of the remaining energy gets transferred to the panel as heat (Hersch & Zweibel, 1982; van Helden, van Zolingen & Zondag, 2004).

$$f_l = \frac{E_f - E_i}{h_p} \tag{2.49}$$

$$\lambda_l = \frac{c_l}{f_l} \tag{2.50}$$

Electron-hole recombination is also a cause of inefficiency in solar cells (Tilley, 2013). The extent to which this occurs is dependent on how far electron-hole pairs are from the depletion

region and the quality of the semiconductor material. Electron-hole pairs which are far from the depletion region, naturally undergo recombination before being swept across the depletion region (Hummel, 2011). Furthermore, impurities may trap charge carriers and so inhibit the amount of available charge (Hersch & Zweibel, 1982; Tilley, 2013).

Another loss that occurs in the systems is due to the thermal resistance of the thin p-type-layer. This occurs because current must first traverse laterally along the thin p-type material of the cell to reach the contact points (Hersch & Zweibel, 1982; Hummel, 2011). Lastly, another loss related to the p-type layer is the shading loss due to the contact points on the top side of this layer (Hummel, 2011). As such, it is beneficial to limit the surface area of these contacts.

A solar cell circuit can be modelled as a current generator, diode and an equivalent series resistance as shown in Figure 2.8 (Markvart, 2000). Shown in this diagram is the equivalent series resistance, R_s. This resistance, due to internal resistance (mostly within the bulk material) causes a voltage drop in the system and should so be minimised. While, in addition, but not shown in this diagram, the loss of current, such as leakage at the perimeter is modelled by parallel shunt resistor R_{sh} (Messenger & Venre, 2003).

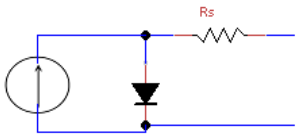

Figure 2.8: A representation of resistance losses in a solar cell

The shape factor is an important term when determining solar cell performance. To understand this factor one needs to look at the I-V characteristic curve as shown in Figure 2.9 (Falk, Durschner & Remmers, 2007). This curve, in conjunction with where the curve intersects the load curve, determines the working point of a PV panel. At a point on this curve, there is a specific current and voltage value that provides the maximum power delivery of the system. This is called the Maximum Power Point (MPP). The respective voltage and current needed to achieve this point are referred to as the Voltage Maximum Power Point (VMP) and Current Maximum Power Point (IMP). The shape factor or fill factor (FF) is written as a ratio of the Maximum Power Point to the product of the short circuit current (I_{sc}) and the short circuit

voltage (V_{oc}) as shown by Eq. (2.51) (Papadopoulou, 2011). A given fill factor for a specific panel can thus be used to determine the maximum power output of the panel (Skoplaki & Palyvos, 2009) and the size of the fill factor can be maximised by increasing the shunt resistance and minimising the series resistance of a solar cell (Messenger & Venre, 2003).

$$FF = \frac{\mathrm{E_{p(max)}}}{I_{sc}V_{oc}} \tag{2.51}$$

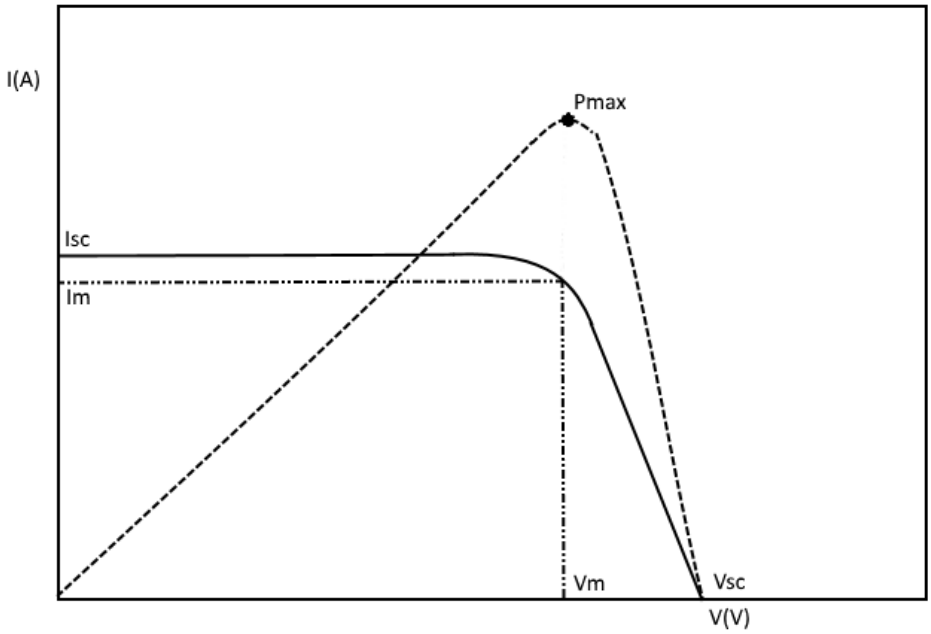

Figure 2.9: I-V characteristic curve

2.3.3 Temperature and Performance

The two most important variables to take into consideration when considering the performance of PV cells are temperature and radiation levels. The relationship between cell and ambient temperature and radiation is first given, followed by descriptions of how different temperatures inhibit the performance of cells.

The performance of PV modules is characterised under operating conditions called Normal Operating Cell Temperature (NOCT). This performance is defined at 0.8kWm^{-2} at an ambient temperature of 20° C, a wind speed of 1ms^{-1} and a spectral distribution of Air Mass (AM) of 1.5 (Air mass is an indication of the thickness of the atmosphere as discussed in Section 2.2.2). This helps determine the spectral composition of radiation reaching the ground (Falk, Durschner & Remmers, 2007). This factor can then be used to calculate the cell temperature as it is commonly assumed that the relationship between cell temperature and the ambient temperature is linearly dependent on radiation. This relationship is depicted by Eq. (2.52) (Markvart, 2000). However, there are many such equations for relating the temperature of the cells to the ambient conditions (Skoplaki & Palyvos, 2009). These types of equations are not discussed further because different equations for determining cell temperature were used in this present study.

$$T_c = \frac{NOCT-20}{0.8}\mathrm{G}+T_a \tag{2.52}$$

Solar cells undergo an efficiency loss at low and high temperatures (Callister & Rethwisch, 2007). This efficiency change is caused by two factors: lattice vibrations and a loss of charge separating ability in the junction. Lattice vibrations inhibit the flow of charge carriers and the contribution of temperature to this quality of semiconductors is significant even at room temperature (Hersch & Zweibel, 1982).

The second cause for inefficiency is realised at high temperatures. n-type properties of extrinsic semiconductors persist between a range of 150 K to 450 K (Callister & Rethwisch, 2007). Above this range, the concentration of holes overwhelms the amount of electrons present from the donor atoms. In this way, the properties of the extrinsic semiconductor tend towards being intrinsic in nature at high temperatures. The region beyond this threshold is termed the Intrinsic Temperature Region (Callister & Rethwisch, 2007).

In a similar way, the p-type side begins to lose its inherent distinguishing properties. This results in charge carriers having so much energy that they move through the junction as though it were not in existence. Also, the junction breaks down as the n-side and p-side lose their properties (as described), and these properties are a prerequisite for the junction's existence

(Hersch & Zweibel, 1982). The performance of cells also decays at low temperatures. At these temperatures, charge carriers are less likely to be excited beyond the donor level to the conduction band and so the flow of charge is less likely. This region is called the Freeze-out region (Callister & Rethwisch, 2007).

Charge carrier mobility is also affected by temperature changes as rising temperature effectively increases the chances of thermal scattering (collisions). Both charge carrier mobility and carrier concentration factors need to be accounted for when calculating the effective conductivity of semiconductors at different temperatures (Callister & Rethwisch, 2007).

2.4 Photovoltaic Thermal Systems

2.4.1 Heat Removal

PV/T systems are classified according to whether or not they are flat-plate or concentrated and what type of fluid is used to remove heat from the system (air or water) (Charalambous et al., 2007). This thesis focuses on a flat-plate setup and methods of heat removal for such systems are therefore discussed.

Flat plate PV/T systems can be broken down into four main categories of design. First, the merits of different heat removal fluids will be discussed followed by a description of Sheet-and-Tube, channel, free flow and two-absorber type PV/T systems (Zondag et al., 2003). A performance summary of some of these systems is given in Table 2.1.

Table 2.1 Thermal and electrical efficiencies of selected PV/T system designs

Source: Adapted from Zondag et al. (2003)

Design type	Thermal Efficiency (%)	Electrical Efficiency (%)
PV panel	N/A	9.7
Sheet-and-Tube PV/T (no cover)	52	9.7
Sheet-and-Tube PV/T (1 cover)	58	8.9
Sheet-and-Tube PV/T (2 covers)	58	8.1
Channel above PV/T	65	8.4
Free Flow PV/T	64	8.6
Two-absorber PV/T (insulated)	65	8.4
Thermal Collector	83	N/A

Air and water are common heat transfer fluids where the choice of fluid depends on the environment in which the systems reside as discussed in Section 1.3(Tripanagnostopoulos et al., 2002). The fluid circulation in a PV/T system can be achieved by using an active or passive (Kumar & Tiwari, 2009) system. In a pumped system, DC electric pumps/fans driven by the PV panels can be used. Although this reduces the power available from the Panels, net power gain is possible (Dubey & Tiwari, 2008).

Sheet-and-Tube PV/T systems are built such that a tube is fitted to a conventional photovoltaic panel (See Figure 1.1). The thermal insulation, and thus the thermal efficiency of this kind of system, can be improved upon with the addition of top covers. These covers, however, add additional heat retention and thus reduce the overall electrical efficiency of the collector (Zondag et al., 2003). This type of design is the easiest of all four methods to manufacture and yields adequate efficiency results as shown in Table 2.1 (Charalambous et al., 2007).

Another type of PV/T system design is a channel type (Figure 2.10). In this setup, multiple channels, usually made from plastic sheets, are used to withdraw heat. This kind of system allows for higher pressures than a single channel system, but the plastic has a higher coefficient

of expansion than metal alternatives. This expansion issue makes proper thermal contact to the PV panel more of a challenge (Hasan & Sumathy, 2010).

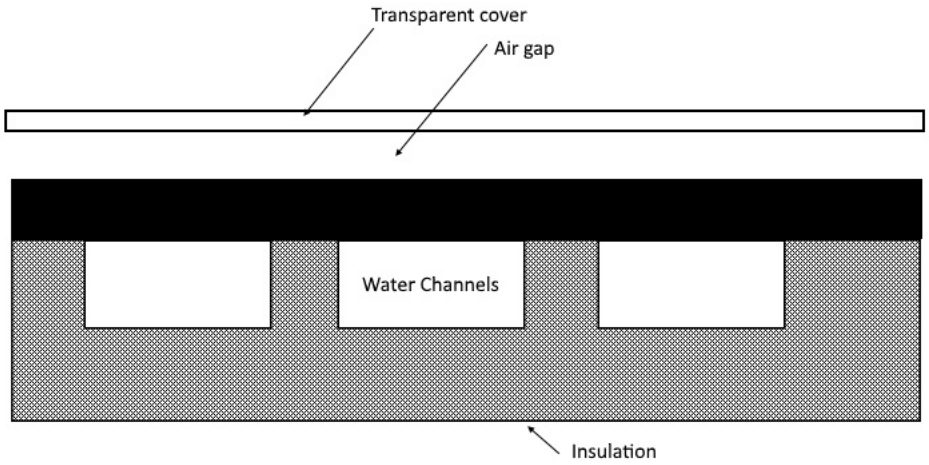

Figure 2.10: Channel Type PV/T system

PV/T systems can also have heat removal done from the top of the panels. Such systems have a channel for air (air gap) and a separate channel for water heat collection as shown in Figure 2.11 (Charalambous et al., 2007). This type of structure helps minimise the mean distance between heat generation and heat collection and thus improves heat transfer in the system (Hasan & Sumathy, 2010).

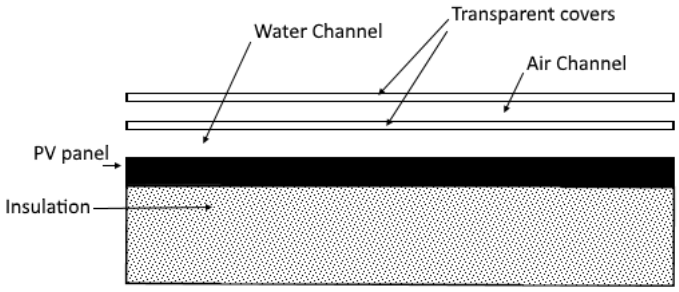

Figure 2.11: Channel above PV/T

Two-absorber PV/T systems have an air channel (air gap) and a water channel above a transparent PV module. Additionally, below the module, there is a water channel

(Charalambous et al., 2007). One variation of this design is the addition of an air insulation channel above the upper channel (primary channel) and beneath the transparent panel (above the secondary channel) as shown in Figure 2.12. This reduces the heat loss of the system but decreases the durability of the system (Zondag, 2008). This type of system is said to have a high efficiency, but the complexity of the system makes it difficult to manufacture (Charalambous et al., 2007).

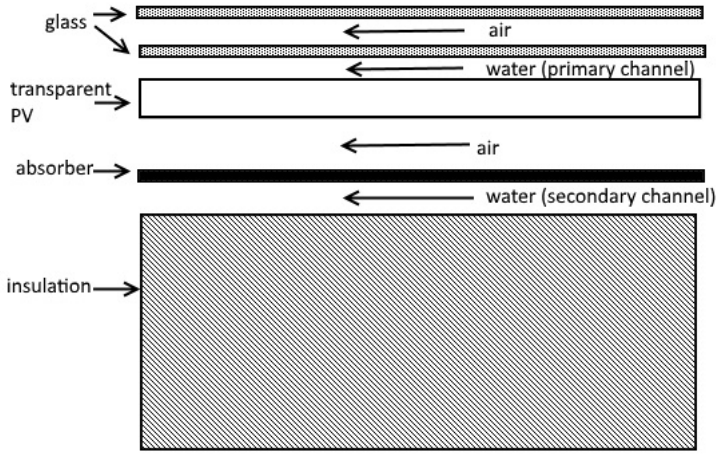

Figure 2.12: Two absorber PV/T system configuration

Free flow PV/T systems have a mixture of air/fluid vapour and fluid flowing between the glass cover and the PV module as shown in Figure 2.13 (Charalambous et al., 2007). This type of system works out to be cost-effective in that the need for an additional glass layer above the PV panel is eliminated. However, the fluid medium needs to be transparent for the solar spectrum, which limits the applicability of fluids for this function. Also, if water, which evaporates easily, is chosen as the fluid for the system, significant heat loss in the system occurs due to evaporation. This reduces the feasibility of water as a heat removal medium (Zondag et al., 2003).

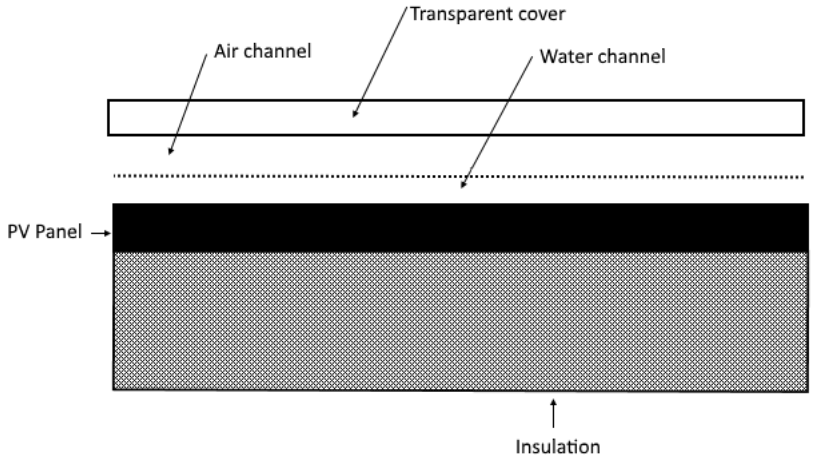

Figure 2.13: Free Flow PV/T system

2.4.2 Hybrid Photovoltaic Thermal Desalination Systems

Desalination can be broadly classified into two categories: membrane-based desalination and thermal desalination (solar distillation falls under this category). Membrane-based desalination is said to be highly energy intensive and not cost-effective for small volumes of fresh water output. On the other hand, thermal desalination is appropriate for water outputs of less than $50m^3$ per day (Madhlopa & Clarke, 2013). Because this thesis focuses on using the waste heat energy (a low form of energy) and because only a few PV panels are used, distillation is used (thermal desalination) instead of membrane-based desalination. This section first presents some of the findings of studies that have been carried out on simple solar stills. The section then progresses to highlight studies that have incorporated the use of view factors into solar still models. Finally, this section highlights the findings of hybrid-thermal desalination studies.

Al-Hinai, Al-Nassri & Jubran (2002) performed a study to predict the performance of a simple solar still with different climatic conditions and design and operation parameters being changed. The study found that ambient temperature and wind speed have a significant effect on distillate yield. That is, an increase in temperature from 23°C to 33°C was seen to increase the yield by 8.2%. And, concerning wind speed, a small increase in strength from 1m/s to 3m/s resulted in an increase in yield of 8%. The effect that wind speed had on yield was ascribed to the fact that wind speed affects the heat transfer coefficient. Thus, the cover temperature is naturally lower, and condensation happens at a higher rate on the inner side of the glass. The

study found an optimal insulation thickness of between 0.09 and 0.13m. With regard to tilt angle, optimal angles were found to be steeper in winter and shallower in summer. In this region, an optimal angle of 23° was found, although the latitude was not reported.

Interestingly, preheating the water did not have a highly significant impact on the daily water output yield. Increasing the temperature from 20°C to 50°C only resulted in a 9% increase in daily water production. Also, beyond 40°C, the increase in daily water output decreased remarkably. On the other hand, the daily water yield was found to be highly dependent on the depth of water. A lower depth of water reduces the heat capacity which results in a higher temperature in the water and thus a better evaporation rate. As an example, a decrease in water depth from 0.1m to 0.005m led to an increased daily output by19.6%. The study recommended a depth of between 0.02m and 0.06m.

El-Sebaii (1998) created a transient mathematical model for a vertical solar still. The paper concluded that the yield performance is greatly dependent on the wind speed and the length and breadth of the solar still. Also, that as the area becomes larger, so do the heat losses. As such, an optimal area of 3.5m^2 was found (which is quoted as being similar to non-vertical stills). Additionally, that for air velocities beyond about 10m/s, still yield performance did not significantly increase.

Tiwari & Tiwari (2007a) undertook a study to determine the performance of solar still systems depending on the different inclinations of the condensing cover. Experiments were conducted over the period of one year in New Delhi and found that a 15° inclination gave the best annual yield and distillation efficiency. The study found that the inner surface temperature of the glass to be 2.5° C higher than the outer surface (maximum) in summer and so it was recommended that this temperature should be in the calculation of the internal heat transfer coefficients. The study also found that the evaporative component of internal heat transfer to be the most significant fraction of internal heat transfer and that the radiative heat transfer component dominates at temperatures of around 32° C.

In these studies, and in other similar studies (Madhlopa, 2014), the view factor is seldom taken into account in the calculation of internal radiative heat transfer coefficients in solar stills ($h_{r,wk}$). As such, Madhlopa (2014) undertook a study to determine the effect that the inclusion of a view factor has on model accuracy. This was done by comparing the Mean Bias Error (MBE), Root Mean Square Errors (RMSE) (See Section 3.4.2.1) and t-values of two versions of the model (one with a view factor and one without). These results were then compared to

the actual outputs of an experimental setup to determine which of the two models performed more accurately. The study concluded that the model that incorporated the view factor overestimated water yield and the model that did not incorporate the factor underestimated the yield. Also, the inclusion of a view factor in the model yielded lower RMSE and t-statistic values than the model that did not incorporate the view factor. As such, models which account for the view factor are said to offer better performance over models that do incorporate this factor.

A similar study was performed by El-Maghlany, El-Samadony & Kabeel (2015), but this time, the performance difference between view factor and no-view factor models was observed for varying still cover tilt angle and insolation levels. The study concluded that that the inclusion of a view factor is particularly important for a steeper cover tilt angle at times of low solar insolation.

With regard to hybrid PV/T desalination systems, Kumar & Tiwari (2008a) performed a study to compare the performance of a passive hybrid-PV/T solar still to an active hybrid-PV/T solar still. Both systems used the same basin design (a 1m by 1m black basin with a glass cover at a 30° incline), and the experiment was conducted in Delhi. The experiments tested various water depths (0.05, 0.10 and 0.15m) and in both active and passive modes. In the active system, the pump was on for between 5 and 3 hours. The performance of the two types of systems was accessed with respect to daily distillate yield as a function of the pump running time and of water depth, thermal efficiency and exergy. The study found that the daily distillate yield was 3.5 times higher in the hybrid-active system than in the passive system for all water depths. However, it was found that less pumping time resulted in higher water yields during dark periods. This was because the temperature in the distillation chamber was higher with shorter pumping durations because reverse thermal losses (from the collectors) were smaller in this scenario. A pumping time of 5 hours was found to be ideal. Interestingly, when the hybrid system had its pump turned off completely and with water levels varying at 0.15m, 0.10m and 0.05m, the water yield was 2.1, 2.4 and 2.6 times the single unit passive solar still for these different water depths respectively. However, the exergy efficiency increases for the two systems with increasing water depth.

Kumar & Tiwari (2009) undertook a further study into the cost advantage of using passive vs. active hybrid PV/T desalination systems. The payback period for a passive system ranged from between 1.1 and 6.2 years while the payback period for the active still ranged between 3.3 and

23.9 years. However, it was noted that in remote and inaccessible areas, the value ascribed to water may be higher and thus the applicability of hybrid systems becomes more pertinent. Additionally, further cost reduction in the manufacturing of PV modules is expected to bring down these payback periods in the future.

Kumar, Tiwari & Gaur (2010) performed an experiment, based in Delhi, to determine the empirical relationship between basin water, ambient and the PV glass cover temperatures in a hybrid PV/T desalination system. The results were validated with experimental results and by outputs obtained from a numerical solution to the heat balance equation of the solar still. The study found a maximum relative error of 1.12% between the empirical and numerical solutions obtained.

No studies were found which incorporated the use of a view factor into PV/T desalination models. As such, it was anticipated that the inclusion of a view factor into a PV/T desalination model would improve model performance, as it did in previous solar still studies (Madhlopa, 2014; El-Maghlany, El-Samadony & Kabeel, 2015)

2.4.3 Efficiency

The instantaneous electrical efficiency of a system can be determined by the ratio of electrical power produced to the amount of incident irradiance. This ratio, per unit area, is shown by Eq. (3.63). Likewise, the thermal efficiency of the system can be attained by considering the temperature difference between the average temperature of the water (T_{w1}) and the temperature of the water leaving the tube (T_{w2}), the mass flow rate of water in the tube, the specific heat of water and the total irradiance available on a titled surface as shown, per unit area, by Eq. (3.64)(Chow, 2003).

$$\eta_e = \frac{E_p}{G_t} \tag{2.53}$$

$$\eta_{th} = \frac{\dot{m}_w C_w (T_{w2} - T_{w1})}{G_T} \tag{2.54}$$

Theoretical efficiencies of 60-80% are predicted for a once through system (water is not recirculated in the system) circulation system, while in practice, thermal efficiencies of 60% have been achieved through experimentation. However, efficiencies of the PV/T systems are mostly dependent on the design of the PV/T system (Huang et al., 2001) with some of these designs discussed in Section 2.4.1. These reported efficiencies are high as they indicate instantaneous efficiency. In reality, the temperature of the fluid may rise with time, and so the system efficiency will deteriorate. The deterioration is attributed to the temperature saturation of the fluid in the system. The daily characteristic efficiency takes account of the daily efficiency change. A test conducted by Huang et al. (2001) indicates a possible daily efficiency of 38%. For illustrative purposes, the same source states that this efficiency can be compared to conventional solar hot water heaters which have thermal efficiencies of about 50%. The discrepancy in the efficiencies of the two types of systems is attributed to the construction differences between conventional solar water heaters and PV/T systems (Tripanagnostopoulos et al., 2002). Some of these differences include (Sandnes & Rekstad, 2002; Zondag, 2008):

- The absorptivity of the surface of the PV panels is lower than that of conventional solar collectors, and thus less energy is absorbed.
- There is an additional thermal resistance in the systems due to the extra layers required in PV/T systems (i.e. the adhesive between the collector plate and PV panels)
- Some energy is 'lost' to electrical generation (that is, it is not used for thermal purposes)

The overall efficiency of a PV/T system can be expressed as the sum of the electrical efficiency and the thermal efficiency (Tripanagnostopoulos et al., 2002). However, due to the differences in quality of energy between thermal and electrical energy, the efficiencies are rather calculated as the primary energy saved which can be expressed as Eq.(2.55)(Chow, 2010). In this equation the generation and distribution electrical efficiency (η_g) is the total to-the-door efficiency from a supplying utility.

$$\eta_f = \frac{\eta_e}{\eta_g} + \eta_{th} \tag{2.55}$$

For hybrid PV/T desalination systems, the energy needed to evaporate the calculated hourly yield of water needs to be considered as a ratio of total incident irradiation for that period. Thus for this system, irradiance on the cover of the solar still (G_k) as well as the irradiance on the collector/PV combination (G_g) need to be considered with the respective areas of those components. An hourly efficiency is given by Eq. (2.56) (Kumar & Tiwari, 2008a).

$$\eta_{th(active)} = \frac{\dot{M}_{ew} L}{(N G_g A_g 3600 + G_k A_k 3600)} \tag{2.56}$$

2.5 Modelling Overview

2.5.1 Model type

PV thermal models that experience rapidly changing radiation require that the mass of the PV material be accounted for as this mass results in a lag in the time response of the material. For example, if the temperatures of a module are recorded at minute intervals and a step drop in radiation is experienced, an exponential decay in the module temperature is expected. This exponential decay's time constant is defined as the time it takes for the module temperature to drop by 63% of the total change in temperature and is in the order of 7 minutes (Jones & Underwood, 2001) (it is analogous to the time constant of a resistor-capacitor circuit (RC) (Armstrong & Hurley, 2010)). This time constant implies that one needs to wait 7 minutes after an affecting variable fluctuation for the system to be considered as steady state (Tina & Abate, 2008).

A study by Zondag et al. (2002) undertook the creation of four models: one dynamic 3D model and one steady state 3D, 2D and 1D model and a PV/T experimental configuration for verification purposes. It was found when assessing the performance of the 3D dynamic and 3D steady state systems at the start of the day, that the dynamic systems experienced an under-prediction because the system components first had to heat up. Similarly, at the end of the day, the heat inertia accounted for in the dynamic models led to an over-prediction in these models. Interestingly, when considering the overall performance of the dynamic systems over an entire

day, these effects cancel out, which results in little deviation between steady state and dynamic model daily yield predictions. For this reason, steady state models run with hourly input data are considered to be sufficient to predict the daily performance of PV/T systems.

This study also found that higher order models showed little improvement in performance over lower order systems and that they were cumbersomely slow for annual performance simulations. As a result of this and the minor improvement in the performance prediction capabilities of dynamic models compared to steady state models, the study used a 1D model to determine the annual energy yield in a PV/T system.

PV/T systems are inherently dynamic and steady state models are insufficient to predict changes in system component temperatures with fluctuating flow rates or radiation levels accurately (Chow, 2003). Furthermore, because of current computational abilities, dynamic models are not overly burdensome, and they allow the observation of temperature changes in system components (Chow, 2003).

Simple solar still modelling studies have also used dynamic models (El-Sebaii, 1998; Al-Hinai, Al-Nassri & Jubran, 2002) and a study into a hybrid PV/T desalination System assumed quasi-steady-state conditions in determining a characteristic equation for the system (Dev & Tiwari, 2010). Therefore, a semi-dynamic (which used hourly data) 1D simulation was used in this thesis to determine the daily and annual performance of the designed hybrid PV/T desalination system.

2.5.2 Software

The two software packages considered for simulation in this thesis were Matlab and TRaNsient System Simulation (TRNSYS) (Kalogirou, 2001). Each of these software packages is now discussed in brief.

TRNSYS was developed by the University of Wisconsin and was originally programmed in ANSII and Fortran-77. TRNSYS allows the creation of quasi-steady state simulations (Kalogirou, 2001) and was initially devised to perform simulations for Renewable Energy Applications and active or passive solar designed building heat simulations (EnergyModels.com, 2013). The software is versatile as, in addition to these processes,

TRNSYS is able to model other systems such as traffic flow or different biological processes ("What is TRNSYS?″, 2016). A version of TRNSYS is available for academic purposes at a price of $2370 ("Pricing Info″, 2016).

The program fundamentally consists of two parts: The Kernel (engine) and a library of components. The first part is responsible for performing all the calculations in the system. This includes: solving the system, determining the thermophysical properties of the system, performing plots, etc. The second part consists of a library of about 150 standard components such as pumps or wind turbines etc. which are each modelled by different differential or algebraic equations. These component models are customisable so that they model specific systems more accurately ("What is TRNSYS?", 2016). These components are represented visually by boxes which require that their parameters (constants) and input variables be stipulated. These components are then connected and represented by a flow diagram which provides a way for the relationship between the components and flow of information to be stipulated (Kalogirou, 2001). TRNSYS was used by Kalogirou (2001), (Kalogirou & Tripanagnostopoulos, 2006) and (Fraisse, Ménézo & Johannes, 2007) to model PV/T systems.

Matlab (which stands for Matrix Laboratory) has been available since 1984 and was initially developed to interface with LINPACK and EISPACK, matrix software of the time (Houcque, 2005). Matlab has since evolved into a high-level, interpretive programming language (Houcque, 2005) and it is ideally suited for numerical computation, aiding visualisation and software development ("Key Features″, 2016). Pricewise, Matlab Home 2015b is available for $135 ("New License for MATLAB…″, 2016).

Two of Matlab's greatest strengths is its ability to plot and undertake numerical methods (McMahon, 2007). Also, it is said to be easy to learn, and the fact that it is interpreted (that is, non-compiled) makes it relatively easy to find problems in code (Houcque, 2005).

Matlab/Simulink was used in a study undertaken by Da Silva & Fernandes (2010) to determine the annual performance of a PV/T system in Lisbon. One of the findings of this study was that the Matlab/Simulink environment provides an excellent way of breaking a problem down into modular components which lend itself useful in solar system modelling, an ability to scale simulations, develop them quicker and easier integration with computation tools peripheral to Matlab/Simulink. (Moradian, 2013) also undertook a study to determine the performance of a dynamic PV/T system a simulation using Matlab/Simulink. Lastly, a simulation of a PV system

by taking into account changes in temperatures was also modelled by Abdulkadir, Samosir & Yatim (2012) in Matlab/Simulink.

Both TRNSYS and Matlab appeared to be suitable software applications for this thesis in that similar modelling studies have been undertaken with these packages. However, from a cost perspective, Matlab is significantly more affordable. In addition, this language is commended for its versatility (Da Silva & Fernandes, 2010) in a model that is very similar to the subject of this thesis. Thus, Matlab was chosen over TRNSYS for the simulation part of this thesis.

3 Methodology

3.1 Introduction

Hybrid PV/T desalination systems generate electricity and waste heat, with this waste heat then being used to produce a fresh water yield (See Appendix A). To expand, solar radiation enters the system separately through the PV and solar still parts of the hybrid PV/T desalination system. In the PV part of the system, some of the energy in this radiation is captured by the PV panels and is converted to electrical energy while the rest remains as heat energy. This heat then moves through the panel, adhesive, absorber plate and tube into the water within the tube, while some is lost to the environment through the insulation surrounding the back-plate and tube. This heated water then flows through the tubes to the basin where additional radiation is received and absorbed by the water. Heated water in the basin then evaporates and condenses on the cover of the still and consequently runs down to a collector channel. This chapter deals with the design of this system (Section 3.2), the equations that govern the model (Section 3.3) and the validation of the model (Section 3.4).

A hybrid PV/T desalination system was designed for modelling purposes (Section 3.2). Aspects relating to the design are first discussed with regard to the PV component of the system (Section 3.2.1) and then with regard to the solar still part of the system (Section 3.2.2). Lastly, the tubes interconnecting the two system components are discussed (Section 3.2.3).

After the design is presented, the system model is discussed (Section 3.3). This section starts by providing the models for both the PV (Section 3.3.1) and solar still part (Section 3.3.2) of the hybrid PV/T desalination system. Thereafter, the determination of the flow rate between the two parts of the system is discussed (Section 3.3.3) followed by the numerical methods used in to implement the model (Section 3.3.4) and the solution procedure for implementing these models in Matlab (Section 3.3.5).

Next, in order to validate the model, some parameters of the model had to be changed so as to conform to the specifications of an existing experimental design (All aspects of this validation are discussed in Section 3.4). This validated model also creates a means for comparing the relative performance of a model that incorporates a view factor (hereafter, Model 1) and a model that does not incorporate a view factor (hereafter, Model 2)(See Table 3.1). Section 3.4.1

first presents the design parameters that differ from the design presented in Section 3.2. Thereafter, statistical tools for validation are presented (Section 3.4.2) followed by the validation procedure (Section 3.3.1). Finally, the sensitivity analyses procedures are provided (Section (3.5).

Table 3.1: Summary of models used for validation

Model	Description
Model 1	View factor present
Model 2	No view factor present

3.2 System design

3.2.1 PV Component

For the PV and collector configuration, a Sheet-and-Tube type design (Chow, 2003) with a single glass cover was chosen. This design was selected because Sheet-and-Tube designs are recorded as having the best electrical efficiency (Zondag et al., 2003) and, in addition, the performance of such systems is well documented (Chow, 2003; Dubey & Tiwari, 2008).

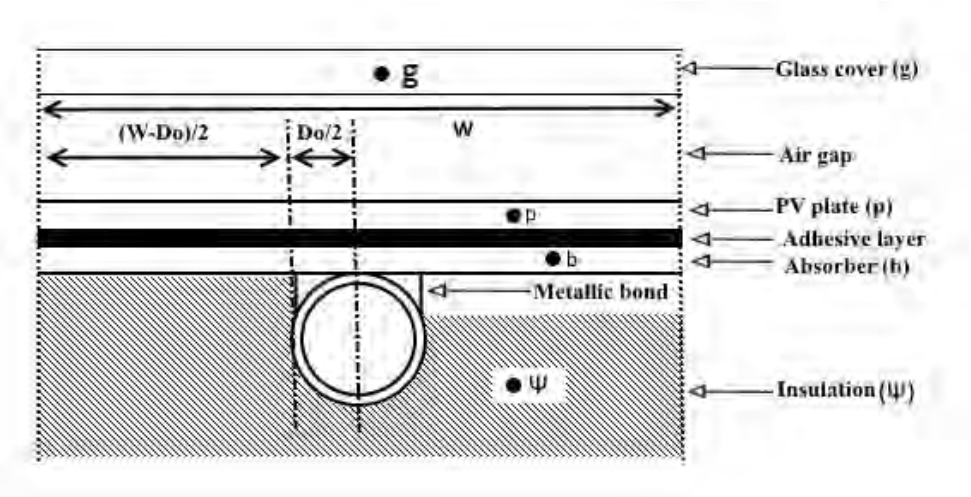

Figure 3.1: Side view of PV panel configuration

Source: Adapted from Chow (2003)

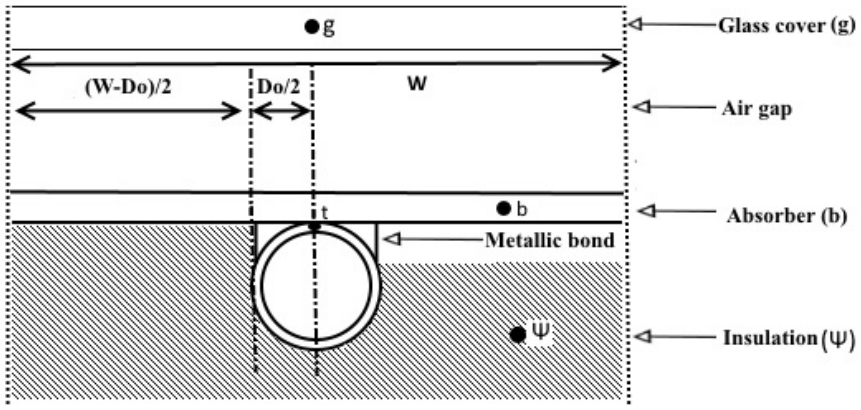

Figure 3.2: Side view of collector without PV covering

Source: Adapted from Chow (2003)

This design consists of a PV panel which is mounted to a part of an absorber plate with a thin adhesive layer. The term 'absorber' refers to the absorber covered by PV panels (See Figure 3.1) while 'collector' is used to refer to the part of the absorber not covered by the PV panels (See Figure 3.2). Two referencing terms are needed as heat transfer in the air gaps is treated separately). In cases where both collector and absorber are discussed as a unit, the term collector is used. A set of parallel tubes is then attached to the absorber/collector plate to remove heat from the system (See Figure 3.3). A glass cover is fitted over the PV panel and collector to protect the panel and improve heat retention and so improve the thermal efficiency of the system. The improved thermal efficiency comes at the expense of the system's electrical efficiency, which is a trade-off of glass covered designs' performance (Kalogirou & Tripanagnostopoulos, 2006). However, the electrical efficiency drop resulting from the addition of a single glass cover is said to be less than 2%, and thus this type of design is still deemed suitable for electrical generation improvement (Zondag et al., 2003). In light of the electrical performance degradation that occurs with the addition of glass covers, the number of glass covers in the system was limited to only one so as to limit the electrical efficiency deterioration. The dimensions of the PV panel configuration are shown in Table 3.2 and the material properties, and specifications of the subsystem are shown in Table 3.3. Other aspects of the design also affect the system, these being: the type of the attachments between the absorber and the tube, the tilt angle of the PV panels and the insulation behind the tubes and absorber. These aspects are discussed separately.

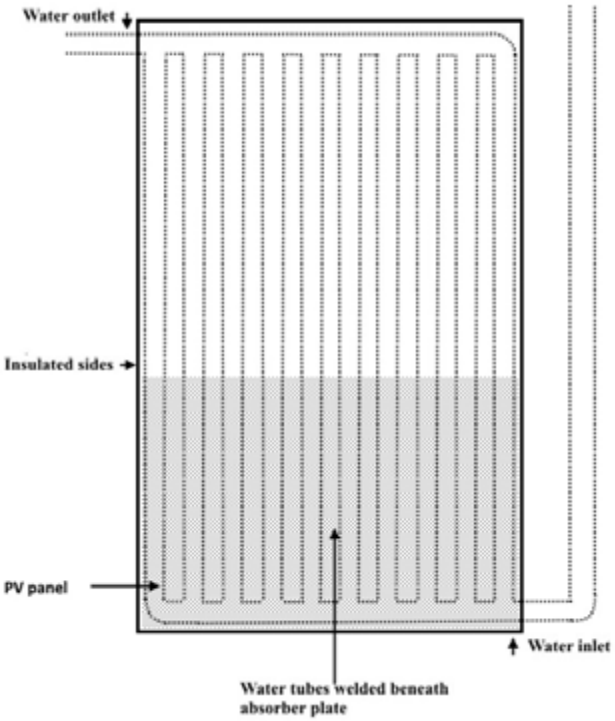

Figure 3.3: Overview of the PV panel configuration

Table 3.2: PV panel configuration dimensions

Component	Value (m)	Source
Total area of glass cover (A_g)	2 ×(2.00×1.00)	chosen
Glass cover thickness	0.004	(Kumar & Tiwari, 2010)
Absorber plate area under the PV module (A_b)	1.00×1.00	chosen
Panel Thickness (δ_p)	0.003	(Kitcher, 2012)
Absorber Thickness (δ_p)	0.002	(Duffie & Beckman, 2013)
Glass to panel gap	0.025	(He et al., 2006)
Insulation Thickness (δ_Ψ)	0.04	(Kalogirou & Tripanagnostopoulos, 2006)
Width between tubes (W)	0.079	calculated

Table 3.3: Material properties and specifications of the PV panel configuration

Component	Value	Source
Module electrical efficiency η_e	15%	(Europe Solar Production, n.d.)
Temperature coefficient of P_{max} (β)	0.46	(Europe Solar Production, n.d.)
Power output (E_p)	$148W_p$	Derived from Europe Solar Production (n.d.)
Tilt angle (β_p)	34°	Chosen for latitude
Panel Emissivity (ε_p)	0.85	(Acciani, Falcone & Vergura, 2010)
Collector Emissivity (ε_q)	Eq. (3.10)	(Duffie & Beckman, 2013)
Panel Conductivity (k_p)	$34Wm^{-1}K^{-1}$	(Acciani, Falcone & Vergura, 2010)
Panel Density (ρ_p)	$2320\ kgm^{-3}$	(Acciani, Falcone & Vergura, 2010)
Panel Specific Heat (C_p)	$678\ Jkg^{-1}K^{-1}$	(Acciani, Falcone & Vergura, 2010)
Excitation coefficient (Λ)	$4m^{-1}$	(Duffie & Beckman, 2013)
Bond heat conductivity (c_{bo})	$100Wm^{-1}K^{-1}$	(Chow, 2003)
Heat transfer coefficient (h_{bp})	$100Wm^{-2}$	(Chow, 2003)
Emissivity Glass (ε_g)	0.88	(Chow, 2003)
Ground Reflectivity (ρ_g)	0.2	(Duffie & Beckman, 2013)
Refractive Index of air (n_A)	1	(Serway & Jewett, 2004)
Refractive Index of glass (n_g)	1.526	(Chow, 2003)
Packing factor	0.9375	(Chow, 2003)
Insulation thermal conductivity (k_Ψ)	$0.038\ Wm^{-1}K^{-1}$	(Incropera & DeWitt, 2002)
Glass Thermal Conductivity (k_g)	$0.780Wm^{-1}K^{-1}$	(Dev & Tiwari, 2010)
Number of tubes per collector	10	Chosen
Number of collectors	2	(Kumar & Tiwari, 2010)

3.2.1.1 PV panel and attachments

A Polycrystalline Silicon (pc-Si) panel was chosen because these types of panels exhibit better electrical performance in PV/T systems than amorphous panels (See Table 7.1). A reasonably efficient pc-Si type panel was chosen to provide the electrical output for the system with its electrical characteristics (temperature coefficient and efficiency) being selected to match a commercially available panel (Europe Solar Production, n.d.).

The PV panel is attached to a part of the absorber plate using a silicon-based adhesive with excellent thermal conductivity (Dow Corning 282) which allows for the thermal expansion of the absorber without fracturing the PV panel as described by Charalambous et al. (2007). The absorber plate is in turn attached to the tubes with a welded metallic bond. The sequence of these layers for a tube segment with a PV panel is illustrated Figure 3.1, while the segment without the PV panel covering is shown in Figure 3.2.

The extent to which heat transfer occurs between the panels and the tubes is largely determined by the heat transfer coefficients between the panel and the absorber and the absorber/collector and the tubes. These coefficients are thus two of the main factors that inhibit the performance of PV/T systems. Low heat transfer coefficients for the bonds between these components results from imperfect adhesion between the PV plate and the absorber plate and, likewise, an imperfect connection between the absorber plate and the tubes beneath (Chow, 2003). 'Reasonable' values for these transfer coefficients were thus found in literature. A panel-absorber heat transfer coefficient of h_{bp} of 100 $Wm^{-2}K^{-1}$ and a bond heat conductivity of Γ_{bo} of 100$Wm^{-1}K^{-1}$ were chosen based on values presented in Chow (2003) as shown in Table 3.3.

The degree of insulation in the system affects how much heat is retained by the system and how much of it is lost to the environment. A fibreglass insulation with a thickness of 5cm and a thermal conductivity of 0.038$Wm^{-1}K^{-1}$ was chosen to insulate the bottom of the absorber plate and tube configuration. This insulation thickness is comparable to the order of thickness and conductivity used by Chow, He & Ji (2006) which utilises a thickness and thermal conductivity of 0.03m and 0.036$Wm^{-1}K^{-1}$ respectively.

3.2.1.2 Tilt Angle

The tilt of a PV panel/collector plays a major role in determining the available radiation on the panels and collector. This is because the tilt angle affects how much radiation is available on the surface of the glass and how much of that radiation gets absorbed by the glass, is reflected off it, or is transmitted towards the panel (this is discussed in Section 2.2.3). Various studies suggest different optimal tilt angles.

Some studies recommend seasonal tilt angle variations which require a steeper tilt angle during the winter season (latitude +5°) and a less steep tilt angle (latitude -5°) during the summer months (Yadav & Chandel, 2013). Alternatively, according to Benghanem (2011), the optimum tilt angle for PV panels should be adjusted every month for optimal performance. Furthermore, some studies indicate that that the optimal tilt angle should be accounted for at specific locations as optimal performance is not only dependent on latitude, but also altitude and the frequency of cloudy days at a specific location (Yadav & Chandel, 2013). However, despite the favourability of a frequently changing tilt angle, it was found that the optimal tilt angle of PV panels, on an annual basis, correspond with the latitude of a location. Using this angle is said to only result in an 8% total annual energy loss compared to the use of a monthly optimum tilt angle. Thus, a tilt angle of 34°, which corresponds to the latitude of the location (33.935°S 18.7817°W), was chosen for the PV/T system over the annual period.

3.2.2 Solar Still Component

Tubes connect the PV and collector configuration to a solar still to form a hybrid PV/T desalination system. To allow for thermo-siphoning, the solar still sits just above the PV panel configuration system. The solar still consists of a square chamber, with a blackened absorptive floor, as illustrated in Figure 3.4. Its dimensions are given in Table 3.4 and thermophysical properties and operational parameters are given in Table 3.5. The still has a saline water inlet and outlet which are situated at the mid-point front wall and the midpoint of the rear wall respectively. In addition, it has saline water replacement inlet for topping up the still and a freshwater collector (See Figure 3.5).

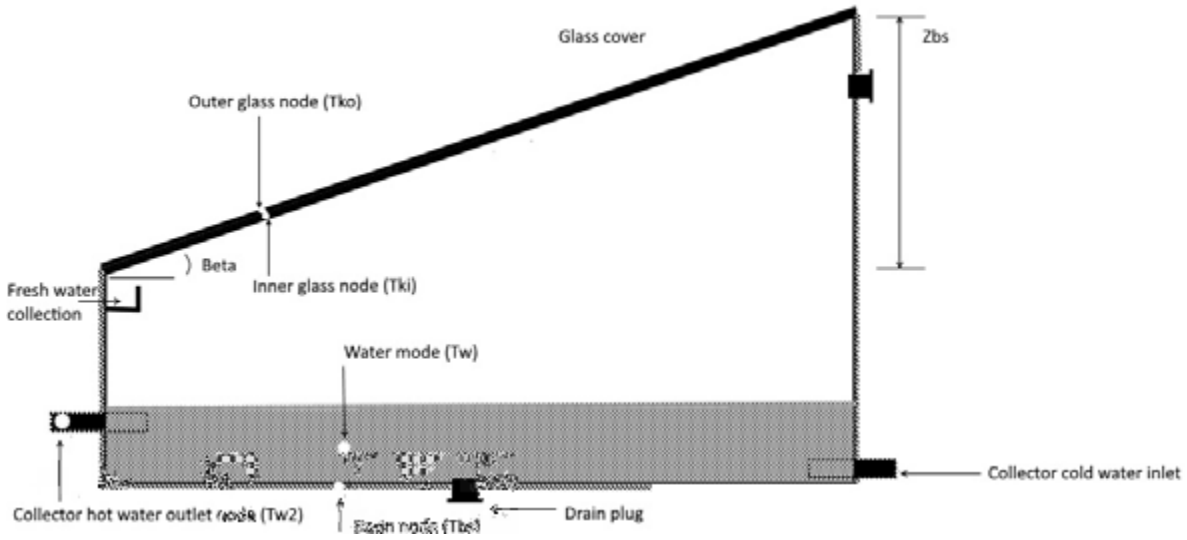

Figure 3.4: Solar still components with nodes shown

Table 3.4 Still dimensions

Component	Value
Still Length	1m
Still Breadth	1m
Cover Length	1.16m
Cover Breadth	1m
Cover Thickness (δ_k)	0.004m
Back height	1.07m
Front height	0.4m
Basin thickness	0.01
Depth of water (δ_k)	0.2m
Tilt Angle (β_p)	34°

Table 3.5: Still thermophysical properties and operational parameters

Component	Value	Source
Emissivity Glass Cover (ε_k)	0.88	(Chow, 2003)
Absorptivity Basin (α_{bs})	Eq. (3.60)	(Tiwari & Tiwari, 2008)
Absorptivity Basin Water (α_{bw})	Eq. (3.54)	(Tiwari & Tiwari, 2008)
Glass Cover Thermal Conductivity (k_k)	1.4$Wm^{-1}K^{-1}$	(Incropera & DeWitt, 2002)
Basin Thermal Conductivity (GRP)(k_{bs})	0.28 $Wm^{-1}K^{-1}$	("Guide to Glass Reinforced Plastic…", 2015)
Basin Heat Capacity (C_{bs})	2.3$kJkg^{-1}°C^{-1}$	("Guide to Glass Reinforced Plastic…", 2015)
Density of basin	1.7kgm^{-3}	("Guide to Glass Reinforced Plastic…", 2015)
Mass of water in basin (M_{bw})	20.53kg	calculated at initial conditions (water temp at 12.1°C)
Mass of water in tube (M_{tw})	12.22kg	calculated at initial conditions (water temp at 12.1°C)
Mass of basin (M_{bs})	24.22kg	(Dev & Tiwari, 2010)

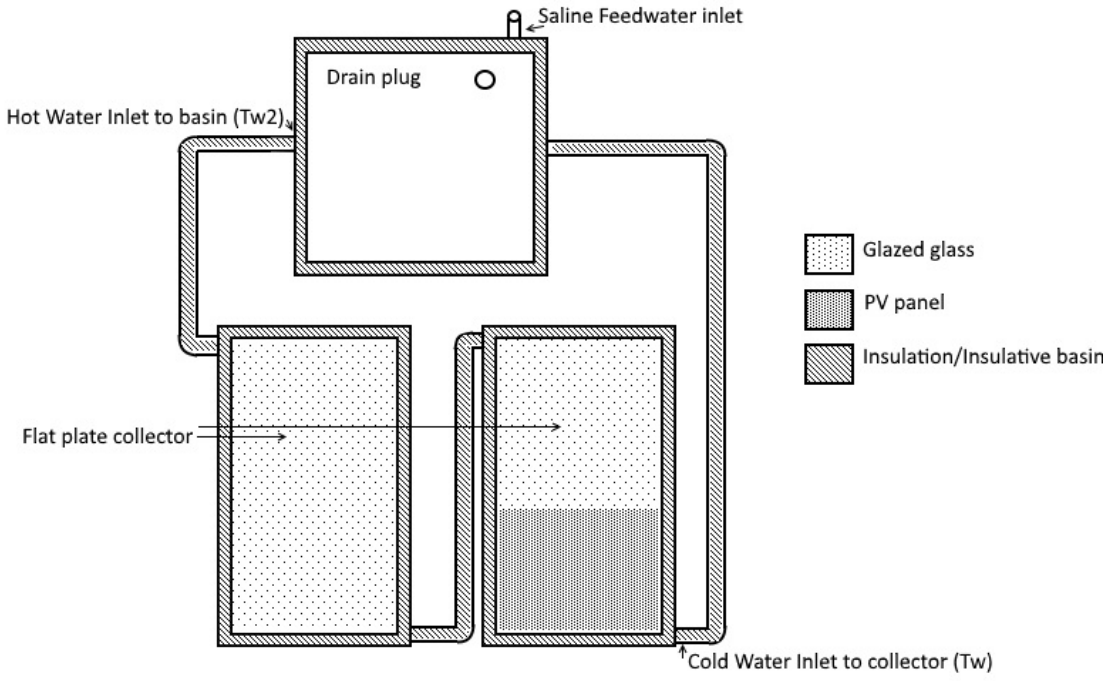

Figure 3.5: Plan view of partially covered PV/T-solar-still configuration and fitting resistance

As with the PV component of the system, the tilt angle of the cover is important as it determines the amount of available radiation on the surface and the component of the radiation that actually reaches the water due to absorptivity, reflectivity and transmissivity. In addition, with the cover, this angle helps gravity 'pull' water down towards the collector channel (Tiwari & Tiwari, 2008). Similarly, the tilt angle of the cover, like that of the PV and collector configuration, is optimal when it is near the latitude of the site (Khalifa, 2011). Considering this, a 34° tilt angle was chosen for the solar-still cover.

The water depth in the solar still is one of the most important factors for improving water yield. A low water depth means a lower effective heat capacity of the water, and thus the basin water reaches higher temperatures with less energy input (Al-Hinai, Al-Nassri & Jubran, 2002). This results in a greater temperature differential between the evaporating and condensing surfaces which means higher water yields for the solar still (Tiwari & Tiwari, 2008). However, this warmer water in the basin also means that heat removal from the PV panels is less efficient than in a system with cooler water. In other words, the electrical efficiency of the panel deteriorates as temperature saturation occurs in the solar still and thus it is advantageous to have a deeper depth of water if electrical production is a primary priority. For this reason, a water depth of 20cm was chosen for the design.

The degree of basin insulation determines, in part, the rate at which heat is lost from the system and thus how hot the basin water can get. As mentioned in Section 2.4.2, hot water in the basin is favourable because it enhances the temperature difference between the cover of the still and the water and therefore improves the water yield of the system. To avoid having to insulate the basin with insulation padding, an insulative glass reinforced fibreglass basin was chosen. This basin has its properties provided in Table 3.5.

3.2.3 Tubes and Flow Rate

The friction in a system can be divided into major and minor frictional losses. The first is determined by the tube diameter and the second by the type of fittings used in the system (See Section 3.3.3). These frictional losses help determine the actual flow rate in a system as they

bring about pressure drop in the system and reduce the flow rate. Major and minor head losses are discussed followed by the water flow rate in the system.

According to Bergene & Løvvik (1995), a small diameter is favourable in systems where electricity generation is a priority and yet, the smaller the diameter of the tube, the greater the major head loss (see Eq. (3.69)) and thus the lower the flow rate in the system. Considering this, copper tubes with a nominal tube diameter of 1.905cm were chosen for the system with further dimensions of the tubes being given in Table 3.6.

To minimise the minor head losses in the system, fittings with a small frictional resistance were chosen. For instance, the inlet to the tube system was chosen to be a bell-mouth inlet instead of a square inlet and long-radius elbows were chosen instead of short-radius elbows. A diagram for the fitting configuration, fitting resistance values and the appropriate equations for calculating total friction in the system are given in Section 3.3.3.

Table 3.6: Tube dimensions for a 0.01905 m (nominal) tube

Source: Adapted from Welty et al. (2007)

Attribute	Size (m)
Nominal Diameter	0.01905
Outside Diameter (D_o)	0.02670
Inside Diameter (D_i)	0.02093
Wall thickness	0.00287

Thermo-siphoning can be used to create water circulation in PV/T systems (Dubey & Tiwari, 2008). This type of system can result in lower flow rates than pumped systems, however, in a study by Bergene & Løvvik (1995), there was only a 10% increase in thermal efficiency when the flow rate was increased from 0.001kgs^{-1} to 0.075kgs^{-1}. Thus, satisfactory performance may be attainable at the flow rates achieved using only a thermo-siphon system. The absence of a pump reduces the system construction costs and, furthermore, makes more electrical power available from the PV panels as described by Dubey & Tiwari (2008).

3.3 Mathematical Model

3.3.1 Photovoltaic Component of Hybrid PV/T Desalination System

3.3.1.1 Assumptions

The following assumptions were made when determining the PV panel component nodal equations and their constituent components:

- Solar cell efficiency varies linearly with temperature according to Eq. (2.47).
- Surfaces are assumed to be grey, and thus radiation properties are not dependent on the wavelength of light (Tiwari & Tiwari, 2008; Duffie & Beckman, 2013).
- A Lumped System Analysis was used. This means that the temperature is assumed to be uniform throughout the different components of the PV/T system. Components are thus said to only be a function of time (Cengel, 1997).
- Incoming solar radiation is assumed to be uniform over the glass and panel.
- The surface reflects light in a specular or specular-diffused manner.
- Air is treated as an ideal gas (Cengel, 1997).
- The thermal resistance of the tube's bond configuration (the weld) and that of the convective heat transfer between the water the tube, is assumed to dominate total thermal resistance in this node. Therefore, the thermal resistance of the slither of absorber plate above the bond and of the actual tube are neglected (Chow, 2003).
- No sudden changes in the temperature or the flow rate of the water are expected. Thus, transport delay analysis, which describes the incremental temperature increase in water as it transits through a PV/T system, was not used. Instead, the water temperature in the tubes was treated as the average between the inlet and outlet water temperatures (Chow, 1997; Chow, 2003).
- Heat flow is one-dimensional (See Section 2.5.1).
- No radiative losses from the basin are assumed because small temperature differences between the insulation and the surrounding air are expected (Chow, 2003).

- The tube diameter is insignificant compared to the depth of the insulation (this means that the insulation thickness is calculated with a uniform thickness as though it were resting directly on the absorber plate) (Chow, 2003).
- The ground reflection factor of 0.2 is assumed. This corresponds to dry and bare ground (Markvart, 2000).
- The angle of incidence is calculated for the previous hour's midpoint and is used to derive the R_b factor for every hour's tilted irradiation value.

3.3.1.2 Nodal Equations

3.3.1.2.1 Glass node

The glass cover of the PV panels absorbs radiation from the sun and receives heat through the air gaps from the panel and collector beneath it. Incoming heat goes towards raising the temperature of the panel and is lost from the cover through radiation and convection. The energy balance for this node is given by Eq. (3.1) (Chow, 2003) (Note, this source does not have a collector component because the absorber is fully covered).

$$Q_g A_g + h_{pg} A_{pg}\left(T_p - T_g\right) + h_{qg} A_{qg}\left(T_q - T_g\right) = M_g C_g \frac{dT_g}{d\tau} + h_{c,g} A_g\left(T_g - T_a\right) + h_{r,g} A_g\left(T_g - T_s\right) \quad (3.1)$$

The heat absorbed by the glass (Q_g) is given by Equation (2.11). This heat is used in conjunction with the area of the glass cover (A_g) to determine how much heat is absorbed by the entire glass cover. After this term, the heat transfer coefficient between the inner surface of the glass and the panel (h_{gp}) and the area of the panel beneath the glass (A_{pg}) are found. The heat transfer coefficient h_{pg} is a combination of radiative and convective losses and is given by Eq. (3.2) (Chow, 2003). The first term in this equation accounts for radiative heat transfer between the glass and the panel and uses Eq. (7.4) (Duffie & Beckman, 2013). Radiative heat transfer between parallel plates depends on the effective emissivity between the panel and glass (ε_{eff}) which has its equation given by Eq. (3.3)(Tiwari & Tiwari, 2008).

$$h_{pg} = \sigma \varepsilon_{eff} \left({T_g}^2 + {T_p}^2\right)(T_g + T_p) + \frac{Nu_a k_a}{\delta_a} \tag{3.2}$$

$$\varepsilon_{eff} = \left[\frac{1}{\varepsilon_p} + \frac{1}{\varepsilon_g} - 1\right]^{-1} \tag{3.3}$$

The last term of Eq. (3.2) is the convective heat transfer coefficient between parallel inclined plates. This term contains the Nusselt number which indicates the ratio of conductive resistance to convective resistance in a fluid. This number is highly dependent on the geometric configuration of the system and can be derived empirically (Cengel, 1997). For this configuration, the ratio can be expressed as a function of Rayleigh's number and the tilt angle of the PV and collector configuration (from β=0° to β=75°) as shown in Eq. (3.4). In this equation, the '+' signifies that those terms should only be used if they are positive. If they are not, they are rendered as zero (Duffie & Beckman, 2013).

$$Nu_a = 1 + 1.44\left(1 - \frac{1708(\sin\beta)^{1.6}}{Ra\cos\beta}\right)\left(1 - \frac{1708}{Ra\cos\beta}\right)^{+} + \left(\frac{Ra\cos\beta}{5830}\right)^{1/3} - 1)^{+} \tag{3.4}$$

In Eq. (3.4), Rayleigh's number (Ra) is a ratio of buoyant to viscous forces in a fluid (Bergman, Incropera & Lavine, 2011). This ratio is thus indicative of the extent to which convection occurs in the system (Cengel, 1997) and it is described by Eq. (3.5).

$$Ra = \frac{g\beta'\Delta T\delta_a^3}{\upsilon_A \kappa_a} \tag{3.5}$$

In Eq. (3.5), the thermal diffusivity of a substance (κ_a) is defined by Eq. (3.6). In this equation, the numerator is thermal conductivity and the denominator is the specific heat of the material, and so the ratio represents how much heat can be conducted through a material compared to the heat that can be stored per unit volume of the material. In Eq. (3.5), the kinematic velocity of air,v_a, is given by the ratio of dynamic air viscosity to air density as shown by Eq. (3.7). Lastly, the volumetric coefficient of expansion for air (β') is given by Eq. (3.5) is given by Eq. (3.8) (Cengel, 1997; Lienhard IV & Lienhard V, 2008). The denominator of Eq. (3.8) is the temperature of the fluid (in absolute terms) which can be evaluated as the film temperature. This term is introduced in order to account for the change of fluid properties with temperature. For an open surface, it is taken as the arithmetic mean between the surface temperature and the temperature of the surroundings (T_∞). However, since convection between two surfaces is now being considered, the average temperature between the two surfaces, as absolute temperatures, was used as shown by Eq. (3.9) (Cengel, 1997).

$$\alpha_a = \frac{k_a}{\rho_a C_a} \tag{3.6}$$

$$v_a = \frac{\mu_a}{\rho_a} \tag{3.7}$$

$$\beta' = \frac{1}{T_f} \tag{3.8}$$

$$T_f = \frac{T_g + T_p + 546}{2} \tag{3.9}$$

To calculate the heat transfer coefficient between the glass and the collector (h_{qg}), shown by Eq. (3.1), the same equation as for the glass-panel heat transfer coefficient (h_{qg}), Eq. (3.2), is used. Except that h_{qg} uses the relevant temperatures (T_q instead of T_p), effective emissivity (ε_{eff}), air gap thickness (δ_a), Nusselt's number (Nu_a) and thermal conductivity (k_a). Additionally, for the calculation of ε_{eff} for the collector-glass configuration, Eq. (3.3), the emissivity of the copper collector(ε_q) is given by a regression shown by Eq. (3.10) as provided for by Duffie & Beckman (2013). The glass-collector heat transfer term in Eq. (3.1) also

requires the surface area of the collector under the glass (A_{qg}) (which neglects the area of the collector under the panel).

$$\varepsilon_q = -0.00443 + 0.0003451T_q + 2.6186 \times 10^{-7}{T_q}^2 \quad (3.10)$$

In Eq. (3.1) the convective heat transfer coefficient from the cover of the glass ($h_{c,g}$) is important as an incorrectly chosen formula can result in a 20-40% error in energy dissipation of the system (Palyvos, 2008). As such, an experiment by Notton et al. (2005) examined the discrepancies between the estimations that different convective heat transfer models made and sought to determine the most accurate model for a particular double-glass poly-crystalline experimental configuration. The study concluded that using a model that only accounts for forced convection and that factors in whether or not the surface is windward or leeward, provides the best estimation of actual convective heat transfer from the panel (for this configuration). This type of model was thus considered for use in this thesis, but, due to the absence of wind direction data in experimental data used for validation (see Section 3.4), a simple forced and natural convective heat transfer coefficient was used as suggested by Tiwari & Tiwari (2008) and as is shown by Eq. (3.11). This empirical relation was also used in a dynamic PV/T model as described by Chow (2003). The radiative heat transfer coefficient is given by Eq. (3.12) (Tiwari & Tiwari, 2008).

$$h_{c,g} = 3u_a + 2.8 \quad (3.11)$$

$$h_{r,g} = \epsilon_g \sigma({T_g}^2 + {T_e}^2)(\mathrm{T}_g + \mathrm{T}_e) \quad (3.12)$$

3.3.1.2.2 PV node

The PV panel receives heat from radiation that has been transmitted through the glass. This heat goes towards raising the temperature of the panel, is transferred to the glass from the panel and to the absorber from the panel, and lastly, to the tube from the panel. This node is modelled by Eq. (3.13) (Chow, 2003).

$$Q_p A_{pg} = M_p C_p \frac{dT_p}{d\tau} + h_{pg} A_{pg}(T_p - T_g) + h_{pb} A_{pb}(T_p - T_b) + h_{pt} A_{pt}(T_p - T_t) \quad (3.13)$$

In Eq. (3.13) the heat transfer coefficient from the panel to the absorber (h_{pb})is determined by the thermal conductivity and the width of the adhesive and is given by Eq. (3.14). The area perpendicular to the direction of heat transfer from the absorber to the panel (A_{bp}) is simply the rectangular area taken up by the tube weld and is given by Eq. (3.15) (Chow, 2003).

$$h_{pb} = \frac{k_{ad}}{\delta_{ad}} \quad (3.14)$$

$$A_{bp} = A_g(1 - \frac{D_o}{W_s}) \quad (3.15)$$

The thermal conductance between the panel and the tubes ($h_{pt}A_{pt}$) in Eq. (3.13) is calculated as a unit by determining the thermal resistance between these nodes (See Eq. (7.9)). The thermal resistance for heat travelling through the panel towards the tube can be divided into components. Firstly, heat travels across the panel towards the tube and then, secondly, it continues vertically through the adhesive layer to the tube. These can be represented as two series resistances which are totalled as R_{pt} according to Eq. (3.16). The inverse of this equation is taken to find $h_{pt}A_{pt}$ as shown by Eq. (3.17) (Chow, 2003).

$$R_{pt} = \frac{x_p}{2k_p(\delta_p L)} + \frac{\delta_{ad}}{k_{ad}(D_o L)} \tag{3.16}$$

$$h_{pt}A_{pt} = \frac{\delta_p L}{\frac{x_p}{2k_p} + \frac{\delta_{ad}\delta_p}{k_{ad}D_o}} \tag{3.17}$$

In the first part of Eq. (3.16), x_p is given in Eq. (3.18). This length, x_p, extends to the point "p" which is the midpoint between the tube and the point at which the configuration repeats (i.e. every W_s meters as shown in shown in Eq. (3.1)). Also in Eq. (3.16) is the variable W_s, which is defined by Eq. (3.19). The '2' in the denominator of Eq. (3.16) accounts for the fact that the lateral transfer of heat occurs from both sides of the tube. Conceptually, these resistances from both sides of the tube are parallel and thus the total resistance for this component of R_{pt} is halved.

$$x_p = W_s/4 \tag{3.18}$$

$$W_s = \frac{W_c - T_m D_o}{T_m} \tag{3.19}$$

In the second part of Eq. (3.16), the area, $D_o L$, in the denominator of the second term of Eq. (3.16) is determined by the diameter of the tube due to the welded configuration and the length of the tube on each segment of the collector. In other words, the surface width of the tube in contact with the adhesive is considered to be D_o because the weld is considered as a unit with the tube.

3.3.1.2.3 Absorber/Collector node

Heat enters the absorber/collector node from the PV panel (for the covered area) and directly from radiation received on the collector. Heat then goes towards raising the temperature of the absorber, travels towards the tubes, towards the insulation and the glass above the collector.

The equation for this node is shown in Eq. (3.20) (Chow, 2003) (Note, this author used a fully covered PV panel and so the $h_{gq}A_{gq}$ was not present).

$$h_{pb}A_{pb}(T_p - T_b) + Q_q(A_{gq}) = M_b C_b \frac{dT_b}{d\tau} + h_{qt}A_{qt}(T_q - T_t) + h_{q\Psi}A_{q\Psi}(T_q - T_\Psi) + h_{qg}A_{qg}(T_q - T_g) \quad (3.20)$$

In Eq. (3.20*)*, the heat transfer coefficient between the panel and the absorber (h_{pb}), is provided for by Eq. (3.14) and the area seen, A_{pb}, is given in Eq. (3.15). The heat absorbed by the collector (Q_q) is determined by Equation (2.36) and the area of collector plate beneath the glass (A_{qg}) is set to a constant (See Table 3.2).

In Eq. (3.20)*,* the heat transfer coefficient between the absorber and the tube (h_{bt}) is given by Eq. (3.21). This equation was derived in the same way as the lateral heat transfer coefficient in the panel as shown in Eq. (2.37). Now, however, the appropriate thermal conductivity (k_b) is used for the absorber material with the average distance travelled by the heat (x_b) being given in Eq. (3.22). The area, for lateral heat flow, between the absorber and the tube (A_{bt}) is given by Eq. (3.23).

$$h_{bt} = \frac{2k_b}{x_b} \quad (3.21)$$

$$x_b = \frac{W - D_o}{4} \quad (3.22)$$

$$A_{bt} = \delta_b L \quad (3.23)$$

In Eq. (3.20). the heat transfer coefficient between the absorber and the insulation ($h_{q\Psi}$) is given by Eq. (3.24) . In this equation the '2' is introduced, as with Eq. (3.24), because heat is received from either side of the tube in parallel which halves the thermal resistance. Also in Eq. (3.20*)*, the area between the absorber and the insulation ($A_{q\Psi}$), is calculated with as A_{bp}

by Eq. (3.15). The last heat transfer coefficient, between the glass and the collector, (h_{qg}) and its associated area (A_{qg}) is given in Section 3.3.1.2.1.

$$h_{q\Psi} = \frac{2k_{\Psi}}{\delta_{\Psi}} \tag{3.24}$$

3.3.1.2.4 Tube node

Heat enters the tube from the collector and panel and goes towards raising the temperature of the tube (as already mentioned, the tube mass (M_t), includes the mass of the bond material and the thin portion of absorber plate above the bond). Heat leaves the tube through the insulation and by heating the water within the tube. The nodal equation for the tube is given in given by Eq. (3.25).

$$h_{bt}A_{bt}(T_b - T_t) + h_{pt}A_{pt}(T_p - T_t) = M_t C_t \frac{dT_t}{d\tau} + h_{t\Psi}A_{t\Psi}(T_t - T_{\Psi}) + h_{tw}A_{tw}(T_t - T_{w1}) \tag{3.25}$$

In Eq. (3.25), the heat transfer coefficient between the absorber and the tube (h_{bt}) and the area between the absorber and tubes (A_{bt}) are provided by Eqs. (3.21) and (3.23) respectively. Additionally, the thermal conductance between the panel and the tube ($h_{pt}A_{pt}$) is provided by Eq. (3.17) (Chow, 2003).

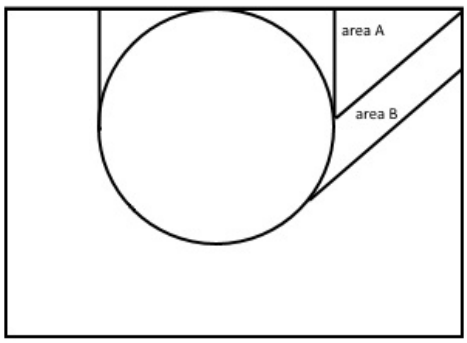

Figure 3.6: Tube view for x_t and $A_{\psi t}$ calculation

To determine the heat transfer coefficient between the tube and the insulation ($h_{t\Psi}$) in Eq. (3.25*),* the assumption can be made that $\delta_\Psi \gg D_o$. This assumption allows $h_{t\Psi}$ to be equated to $h_{c\Psi}$ which is defined by Eq. (3.24)(Chow, 2003). The area seen for heat transfer from the tube to the insulation ($A_{\Psi t}$) is comprised of two components. The first component is the weld area which is shown as area A in Figure 3.6. The second is the area of the side of the tube as shown by area B in the same figure. These areas are totalled for both the left and the right side of the tube to give Eq. (3.26).

$$A_{t\Psi} = \left[\left(\frac{\pi}{2}\right) + 1\right] D_o L \tag{3.26}$$

The last term in Eq. (3.25) to be defined is the thermal conductance of the segment between the tube and water ($h_{tw}A_{tw}$). To calculate this, consider the thermal resistance of the bond-tube combination and the thermal resistance of the water in the tubes. These resistances are in series and thus their equivalent thermal resistances can be combined to find a total thermal equivalent resistance as shown by Eq. (3.27). This thermal resistance can be inverted to find the thermal conductance: $h_{tw}A_{tw}$.

$$R_{tw} = \frac{1}{h_w A_{tw}} + \frac{1}{h_{bo} A_{bo}} = \frac{1}{h_w(\pi D_i L)} + \frac{1}{\Gamma_{bo}\, L} \tag{3.27}$$

The value of the heat transfer coefficient for water (h_w) in Eq. (3.27) depends on whether the flow in the tubes is laminar or turbulent. A test is therefore first performed to see which of the flow regimes is occurring in the system at a given time. This is done by calculating Reynolds number (Re) for the system according to Eq. (3.28). This number is a ratio of inertia forces to viscous forces in a fluid and therefore its value is indicative of if the flow regime is laminar or turbulent (Bergman, Incropera & Lavine, 2011).

$$Re = \frac{u_m D_i}{v} \tag{3.28}$$

If the Reynolds number is below 2300 (for a smooth tube configuration) the flow is said to laminar and in such a case, for a round tube configuration, the Nusselt number is constant (A constant of 4.364) (Cengel, 1997; Lienhard IV & Lienhard V, 2008). This constant can be substituted into Eq. (3.29), and further manipulated to yield an explicit equation for the heat transfer coefficient between water and the tube as shown by Eq.(3.30). In Eq.(3.30), the thermal conductivity (k_w) is evaluated, at the water temperature in the tube, according to Eq. (7.30)(Cengel, 1997; Chow, 2003).

$$Nu = \frac{hD_i}{k_w} \tag{3.29}$$

$$h_w = 4.364 \frac{k_w}{D_i} \tag{3.30}$$

However, if the Reynolds number is above 2300, it indicates turbulence. In such a case, Eq. (3.31) is used instead to calculate the Nusselt number for the flow regime (Cengel, 1997; Bergman, Incropera & Lavine, 2011). Eq. (3.31) depends on Reynolds number (Re) and Prandl's (Pr) number. Prandl's number is a dimensionless number which represents the ratio of molecular diffusivity of momentum to the molecular diffusivity of heat. This number thus indicates the size of the velocity boundary layer compared to the thermal boundary layer. The Prandl number is a function of fluid temperature (Incropera & DeWitt, 2002) and thus a simple interpolation can be used to ascertain the appropriate Pr number for each time instant with specific fluid temperatures.

$$Nu = 0.023 Re^{0.8} Pr^n \tag{3.31}$$

In Eq. (3.31), the constant n in the exponent depends on whether or not the fluid is losing heat. If the fluid is being heated, this is set to 0.4, and if it is losing heat, it is set to 0.3 (Welty et al., 2007). According to this source, this equation is also dependent on an appropriate range of Pr, the ratio of the length of the basin to the diameter of the basin and Re ($Re>10^4$; $0.7<Pr<100$; $L_{bs}/D_{bs}>60$). These factors thus need to be checked before using this equation. Note that the flow through the basin does not meet this condition and so laminar flow is assumed for this part of the system.

In Eq. (3.27), Γ_{bo} (defined in Eq. (3.32)) is the bond conductivity which is a function of the average bond thickness (δ_{bo}) and the width of the bond, W_{bo}. Instead of calculating Γ_{bo} from W_{bo} and δ_{bo}, a reasonable value for Γ_{bo} was used (Chow, 2003). See Table 3.3.

$$\Gamma_{bo} = \frac{K_{bo} W_{bo}}{\delta_{bo}} \tag{3.32}$$

3.3.1.2.5 Insulation node

Heat enters the insulation layer from the absorber and the tube. This heat goes towards raising the temperature of the insulation and towards the environment surrounding the insulation. The energy balance equation for the insulation node is shown in Eq. (3.33) (Chow, 2003).

$$h_{b\Psi} A_{bi} (T_b - T_\Psi) + h_{t\Psi} A_{t\Psi} (T_t - T_\Psi) = M_i C_i \frac{dT_\Psi}{d\tau} + + h_{\Psi a} A_g (T_\Psi - T_a) \tag{3.33}$$

In Eq. (3.33), the heat transfer coefficient for the region between the absorber and the insulation ($h_{b\Psi}$) is presented by Eq. (3.24). As mentioned previously, $A_{b\Psi}$ can be approximated to A_{bp} which is defined by Eq. (3.15).

The heat transfer coefficient ($h_{t\Psi}$) in Eq. (3.33). is calculated from equating $h_{t\Psi}$ to $h_{q\Psi}$, with $h_{q\Psi}$ being described by Eq. (3.24). The area associated with this coefficient, the area seen by the insulation ($A_{t\Psi}$), is given by Eq. (3.26). The last term's heat transfer coefficient ($h_{\Psi a}$) is

provided by Eq. (3.34), and the area for this coefficient is the same as the glass area of the whole PV and collector configuration (A_g). Eq. (3.34) simply represents the series combination of the thermal resistance of heat through the insulation (conductive) and heat leaving the insulation through convective heat loss. In this equation the convective heat transfer coefficient, $h_{c,g}$, is given by Eq. (3.11).

$$\frac{1}{h_{\Psi a}} = \frac{\delta_{\Psi}}{k_{\Psi}} + \frac{1}{h_{c,g}} \tag{3.34}$$

3.3.1.2.6 Water node

Heat enters the water from the tube and goes towards raising the temperature of the water and towards raising the temperature of the moving water within it. The water node has an energy balance as shown by Eq. (3.35) (Chow, 2003).

$$h_{tw}A_{tw}(T_t - T_{w1}) = M_w C_w \frac{dT_{w1}}{d\tau} + \dot{m}_w C_w (T_{w2} - T_{wo}) \tag{3.35}$$

The thermal conductance between the tube and water ($h_{tw}A_{tw}$) in Eq. (3.35) is defined by Eq. (3.27) while the temperatures at the inlet and outlet of tubes beneath the PV configuration are T_w and T_{w2} respectively. The average temperature of water within the tubes is T_{w1}, is the simple average of T_w and T_{w2} as shown by Eq. (3.36). The mass of the water in the tube is calculated for specific temperatures of water according to Eq. (7.20).

$$T_{w1} = \frac{T_{w2} + T_w}{2} \tag{3.36}$$

3.3.2 Solar Still Component of Hybrid PV/T Desalination System

3.3.2.1 Assumptions

The following assumptions were made when determining the solar still nodal equations and their constituent components:

- The flow of water in the basin is assumed to be fully developed laminar (i.e. that Reynolds number <2300 (Welty et al., 2007). Additionally, the flow of the water through the tubes is assumed to be fully developed laminar or turbulent flow (non-developing). This assumption was used by Chow, He & Ji (2006).
- Fluid is incompressible and thus the mean velocity (u_m) does not change throughout the tubes (Cengel, 1997; Lienhard IV & Lienhard V, 2008).
- The mass of the water in the basin stays constant (that is, the basin is assumed to be continually topped up with water that matches the basin water temperature).
- The basin walls and floor experience the same convective heat loss as the glass cover of the PV panels (the same wind velocity is used in the calculation of the heat transfer coefficient of the basin floor and walls). This implies that the wind passes the solar still at the same wind speed and that that it can pass beneath it freely.
- Radiative heat loss from the bottom of the basin was considered insignificant due to the small temperature difference between the basin and the shaded surface below the basin (Chow, 2003).

3.3.2.2 Nodal Equations

3.3.2.2.1 Cover node (outer)

The glass cover of the solar still has a heat equation given by Eq. (3.37). The node experiences heat input by absorbing incident radiation directly and by conduction from the inner node. Heat is then lost to the environment through convection and radiation.

$$Q_k A_k + h_k A_k (T_{ki} - T_{ko}) = h_{c,k} A_k (T_{ko} - T_a) + h_{r,k} A_k (T_{ko} - T_s) \quad (3.37)$$

The heat component directly incident on the glass (Q_k) is calculated in exactly the same way as the heat absorbed by the glass of the PV panels (Q_g) given by Eq. (2.11), but now using the angle of incidence of radiation on the still.

In Eq. (3.37) the conductive heat transfer coefficient between the inner and outer glass cover (h_κ) is calculated the same way as h_{pb} in Eq. (3.14), except that the thermal conductivity and thickness of the glass cover are used. Lastly, the convective and radiative heat transfer coefficients, $h_{c,\kappa}$ and $h_{r,\kappa}$, are governed by the same equations presented for the radiative and convective heat loss of the glass from the PV panels (Eqs. (3.11) and (3.12)). These Equations are reproduced appropriately for the nomenclature of this part of the system in Eqs. (3.65) and (3.42).

$$h_{c,\kappa} = h_{c,g} \quad (3.38)$$

$$h_{r,\kappa} = \epsilon_\kappa \sigma ({T_{\kappa o}}^2 + {T_s}^2)(T_{\kappa o} + T_s) \quad (3.39)$$

3.3.2.2.2 Cover node (inner)

The inner node of the glass still cover is given in Eq. (3.40). Heat is gained from the water surface and is lost through conduction to the top cover of the glass (Tiwari & Tiwari, 2008).

$$h_{lw} A_{bb} (T_w - T_{ki}) = h_k A_k (T_{ki} - T_{ko}) \quad (3.40)$$

In Eq. (3.40), the overall heat transfer coefficient (h_{lw}) is composed of three components which are shown in Eq. (3.41). These components are convective heat transfer coefficient ($h_{c,wk}$), the evaporative heat transfer coefficient ($h_{e,wk}$) and the radiative heat transfer coefficient ($h_{r,wk}$).

The convective heat transfer coefficient, which governs the transfer of heat from the water towards the cover of the solar still, due to buoyancy, is governed by Eq. (3.42) while the evaporative heat transfer coefficient is given by Eq. (3.43) and is a function of the convective heat transfer coefficient. Both the convective and evaporative heat transfer coefficients rely on the partial pressures in the system. These partial pressures, P_w and P_{κ}, are given by Eqs. (3.44) and (3.45) (Tiwari & Tiwari, 2008).

$$h_{lw} = h_{c,w\kappa} + h_{e,w\kappa} + h_{r,w\kappa} \tag{3.41}$$

$$h_{c,w\kappa} = 0.884\left[T_w - T_{\kappa} + \frac{(P_w - P_{\kappa})(T_w)}{(268.9 \times 10^3 - P_w)}\right]^{1/3} \tag{3.42}$$

$$h_{e,w\kappa} = 16.273 \times 10^{-3} h_{c,wk} \frac{P_w - P_{\kappa i}}{T_w - T_{\kappa i}} \tag{3.43}$$

$$P_w = \exp[25.317 - \left(\frac{5144}{T_w}\right)] \tag{3.44}$$

$$P_{\kappa} = \exp[25.317 - (\tfrac{5144}{T_{\kappa}})] \tag{3.45}$$

To derive the radiative heat transfer coefficient between the water and the cover, the radiative heat transfer coefficient has been represented with the appropriate nomenclature for the solar still as shown by Eq. (3.46). In this equation the effective emissivity (ε_{eff}) is different depending on whether or not the view factor is being used. If it is not being used, a simple effective emissivity between the two plates is calculated using the emissivity of water and the glass according to Eq. (3.3). Otherwise, if the view factor is accounted for, ε_{eff} is determined by the emissivity of the water (ε_w), the emissivity of the cover (ε_{κ}) and the total view factor between the water and the cover ($W_{w\kappa}$) as shown by Eq. (3.48).

$$h_{r,w\kappa} = {\varepsilon_{eff}}^{-1}\sigma({T_w}^2 + {T_{\kappa}}^2)(T_w + T_{\kappa}) \tag{3.46}$$

$$\varepsilon_{eff} = \frac{1-\varepsilon_w}{\varepsilon_w} + \frac{A_w(1-\varepsilon_к)}{A_k\varepsilon_к} + \frac{1}{V_{wк}} \tag{3.47}$$

The view factor ($V_{wк}$) in Eq. (3.47) accounts for the loss of radiation between the water and the rear wall (V_{w-rw}), front wall (V_{w-fw}), east wall (V_{w-ew}) and west wall (V_{w-ww}) as shown by Eq. (3.48) (Madhlopa, 2014). The constituent view factors are calculated by considering the water's view of every wall in the basin. The rectangular surface of water is in contact with the rectangular edges of the wall at the back and front of the basin and so Eq. (3.49), which calculates the view factor between rectangular surfaces, can be used to find each of these view factors (Bergman, Incropera & Lavine, 2011). This equation can also be used to find the view factors between the water and the side walls, even though the side walls are not rectangular. To do this, first consider the two variables, H and W, in Eq. (3.49) which are given by Eqs. (3.50) and (3.51) (not provided in nomenclature because they are used only in this section). These variables are ratios of relevant basin widths, lengths and heights, depending on the type of view factor being calculated. The relevant dimensions in these ratios have their X, Y and Z components defined in Figure (2.20). As can be seen in this equation, Z, is the height from the water surface to the top of the cover. However, the sidewall height varies as it runs from the back to the front of the still. Therefore, in order to use Eq. (3.49) to calculate the view factor between the water and each of the side walls, the side walls can be approximated as rectangles with a height defined by the average height between the front and rear wall (Madhlopa, 2014).

$$V_{wk} = 1 - (V_{w-rw} + V_{w-fw} + V_{w-ew} + V_{w-ww}) \tag{3.48}$$

$$V_{ij} \tag{3.49}$$
$$= \frac{1}{\pi W}\left(W tan^{-1}(\frac{1}{W}) + H tan^{-1}(\frac{1}{H}) - (H^2+W^2)^{\frac{1}{2}} tan^{-1}(\frac{1}{(H^2+W^2)^{\frac{1}{2}}}) \right.$$
$$\left. + \frac{1}{4} ln\left\{ \frac{(1+W^2)(1+H^2)}{1+W^2+H^2} \left[\frac{W^2(1+W^2+H^2)}{(1+W^2)(W^2+H^2)} \right]^{W^2} \left[\frac{H^2(1+H^2+W^2)}{(1+H^2)(H^2+W^2)} \right]^{H^2} \right\} \right)$$

$$H = \frac{Z}{X} \tag{3.50}$$

$$W = \frac{Y}{X} \tag{3.51}$$

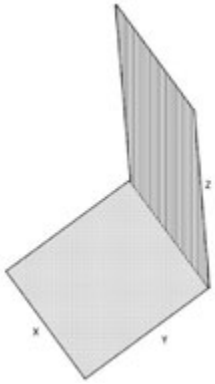

Figure 3.7: Geometry of perpendicular rectangles with a common edge

3.3.2.2.3 Water node

The water node in the basin is represented by Eq. (3.52) (Tiwari & Tiwari, 2008; Kumar & Tiwari, 2008b). In this equation, energy enters the basin with the moving water mass ($\dot{m}_w$). Additionally, energy flux (Q_w) is absorbed directly by the water. This incident heat goes towards raising the temperature of the water and travels towards the cover of the still according to the internal heat transfer coefficients. Heat is also lost to the basin bottom and to the sides of the basin.

$$\dot{m}_w C_w (T_{w2} - T_w) + Q_w A_{\mathrm{bb}} = M_{bw} C_{bw} \frac{dT_w}{d\tau} + h_{bw} A_{bw} (T_w - T_b) + h_{lw} (T_w - T_\kappa) A_{\mathrm{bb}} \tag{3.52}$$

The first term Eq. (3.52) indicates how heat enters the basin from the PV/T configuration through a flowing mass of water. The second term depicts absorbed incident energy flux (Q_w) and is given by Eq. (3.53). In this equation, an effective absorptivity of the water (α'_w), due to the attenuation of radiation, is calculated according to Eq. (3.54). In this equation, the

reflectivity of glass and water are calculated as per Eqs. (2.15) and (2.16) in Section 2.2.3.1. The absorptivity of glass is found using Eq. (2.12) and the water depth within the basin (δ_{wb}). The μ_j and η_j constants are given in Table 3.7 (Tiwari & Tiwari, 2008).

$$Q_w = \alpha'_w G_t \tag{3.53}$$

$$\alpha'_w = (1 - R_g)(1-\alpha_g)(1-R_w)[1-\sum \mu_j \exp(-\eta_j \delta_{wb})] \tag{3.54}$$

Table 3.7: Values of μ_j and η_j

Source: (Tiwari & Tiwari, 2008)

j	μ_j (m^{-1})	η_j (m^{-1})
1	0.237	0.032
2	0.193	0.450
3	0.167	3.000
4	0.179	35.000
5	0.124	255.000

In Eq. (3.52), heat leaves the water through the basin bottom and sides according to h_{wb}. To calculate this coefficient, the flow regime in the basin is always assumed to be laminar because the requirements for the turbulent flow heat transfer coefficient calculations (shown by Eq. (3.31)) are not met by the dimensional ratio of the basin (L_{bs}/D_{bs}>60). Therefore, the heat transfer coefficient for the water can be calculated according to Eq. (3.55), wherein the thermal conductivity of the water in the basin(k_{wb}) is evaluated at the temperature of the water (Eq. (7.30)) and the equivalent diameter of the basin(D_{bs}) is calculated according to Eq. (3.72). The accompanying area for this heat transfer coefficient (A_{wb}), is the surface area of water in contact with the basin. This area is calculated according to Eq. (3.56).

$$h_{wb} = 4.364 \frac{k_{wb}}{D_{bs}} \tag{3.55}$$

$$A_{wb} = D_{bs} \pi L_{bs} \tag{3.56}$$

The total mass of the water in the basin and tube in Eq. (3.52) is assumed to stay constant (M_{wTotal}) as withdrawn water is replaced. However, due to the varying densities of the water in the tube and basin, the mass distribution between the basin and the tube are expected to change with varying temperatures. Therefore, to keep the mass of water in the system constant despite varying water densities (Eq. (7.20)), the mass of the water in the basin is thus written as a function of the total mass of water(M_{wTotal}) at 25° Celsius, and the mass of the water in the tube. This relationship is shown in (Eq. (3.57).

$$M_{bw} = M_{wTotal} - M_{tw} \tag{3.57}$$

3.3.2.2.4 Basin node

Heat enters the basin from the hot water contained within it and from incident radiation which reaches the basin floor after traversing through the water. Heat then goes towards raising the temperature of the basin, and it leaves the basin from the floor and side walls. The basin node has an energy balance equation as shown by Eq. (3.58) (Tiwari & Tiwari, 2008).

$$h_{wb}(T_w - T_{bs})A_{wb} + Q_{bs}A_{bb} = M_{bs}C_{bs}\frac{dT_{bs}}{d\tau} + [h_{bb}(T_{bs} - T_a) + h_{bd}\,(T_{bs} - T_a)]A_{bb} \tag{3.58}$$

The first term in Eq. (3.58) is the heat transfer coefficient between the water and the basin (h_{wb}). This heat transfer coefficient and accompanying area (A_{wb}) are provided by Eq. (3.55) and (3.56). The second term in Eq. (3.58) contains the absorbed tilted irradiance on the basin

floor (Q_{bs}) and is given in Eq. (3.59). In this equation, the effective absorptivity of the basin (α'_{bs}) is given. This variable, as shown by Eq. (3.60), is a function of the absorptivity of the basin, the reflectivity of the glass and water and the absorptivity of the glass. Additionally, the equation includes a term that accounts for the attenuation of solar flux within the basin water (as with Eq. (3.54)), with this solar flux attenuation is given in Table 3.7 (Tiwari & Tiwari, 2008).

$$Q_{bs} = \alpha'_{bs} G_t \tag{3.59}$$

$$\alpha'_{bs} = \alpha_{bs}(1 - R_g)(1 - \alpha_g)(1 - R_w) \sum \mu_j \exp(-\eta_j \delta_{wb}) \tag{3.60}$$

In Eq. (3.58) the thermal resistance from the bottom of the basin towards the air (h_{bb}) is given by a series combination of the thermal resistance of the basin bottom with the parallel convective and radiative thermal resistances from the bottom of the basin. When these terms are combined, the total thermal resistance for the basin bottom is attained as shown Eq. (3.61). Using the definition for thermal resistance, the heat transfer coefficient for the bottom of the basin can be calculated. This is shown by Eq. (3.62)(Tiwari & Tiwari, 2008).

$$R_{bb} = \frac{1}{\frac{K_{bs}}{L_{bs}} A_{bb}} + \frac{1}{(h_{c,bs} + h_{r,bs}) A_{bb}} \tag{3.61}$$

$$h_{bb} = \left(\frac{1}{\frac{K_{bs}}{L_{bs}}} + \frac{1}{(h_{c,bs} + h_{r,bs})}\right)^{-1} \tag{3.62}$$

The heat transfer coefficient from the basin side wall (h_{bd}) is written as a ratio of the area of the side wall exposed to water to the area of the basin floor, as shown by Eq. (3.63). According to Tiwari & Tiwari (2008), this term can be neglected if the area of water in contact with the side wall is small compared to the bottom area of the basin.

$$h_{bd} = \frac{A_{bd}}{A_{bb}} h_{bb} \tag{3.63}$$

3.3.2.2.5 Yield rate of fresh water

The fresh water yield of the system, as an hourly water output, can be calculated according to Eq. (3.64) (Tiwari & Tiwari, 2008) where the evaporative heat transfer rate per unit area is given by Eq. (3.65). This equation uses the latent heat of evaporation which is provided in Appendix C by Eq. (7.34).

$$\dot{m}_{e,wk} = \frac{\ddot{q}_{ew} A_{\kappa} 3600}{L} \tag{3.64}$$

In Eq. (3.64) the evaporative heat transfer rate ($\ddot{q}_{ew}$) *is* given as a function of the convective heat transfer coefficient (h_{cw}) and the partial vapour pressures resulting from the temperature difference between the cover and the water as shown by Eq. (3.65). This heat transfer coefficient is provided by Eq. (3.42) and partial pressures are defined by Eqs. (3.44) and (3.45) respectively (Tiwari & Tiwari, 2008).

$$\ddot{q}_{ew} = 16.273 \times 10^{-3} h_{cw} (P_w - P_{\kappa i}) \tag{3.65}$$

3.3.3 Flow Rate of Water

Chow, He & Ji (2006) presents equations for determining the mass flow rate within a thermo-siphon PV/T system. The two main equations used to determine the flow rate are shown by Eq. (3.66) and Eq. (3.68). The first equation represents the total buoyant driving force in the system and the second the total frictional force in the system.

The buoyant driving force for natural circulation is given by Eq. (3.66). In this equation, the inlet water temperature to the collector is given by T_w and the outlet temperature is given by T_{w2}. Also present in this equation is T_{w1}, the mean of T_w and T_{w2}, and Z_q, the vertical displacement from the bottom of the collector to the top of the collector (Chow, He & Ji, 2006). Lastly this equation also relies on two coefficients, a_1 and a_2.

$$H_{buo} = \frac{T_w - T_{w2}}{2}(2a_1 T_{w1} + a_2)Z_q \tag{3.66}$$

The coefficients a_1 and a_2 in Eq. (3.66) are from the interpolation formula for the specific gravity (γ_g) of the water (specific gravity provides the density of saline water relative to a reference condition sample density at 4° C) (Cengel, 1997)). This interpolation equation is shown by Eq. (3.67)(Chow, He & Ji, 2006) and its coefficients can be found by using known densities of saline water at different temperatures to perform an interpolation.

$$\gamma_g = a_1 {T_{w1}}^2 + a_2 T_{w1} + a_3 \tag{3.67}$$

The total system frictional resistance (Eq. (3.68) in the system is due to the losses incurred from the tube and the fittings in the system. The two components of frictional loss are referred to as major frictional losses (Eq. (3.69)) and minor frictional losses (Eq. (3.70)) as discussed in Section 3.2.3. The governing equations for these frictional components are presented (Welty et al., 2007).

$$H_{f-total} = H_{f-major} + H_{l-minor} \tag{3.68}$$

$$H_{f-major} = f_t \frac{L_t}{D_i}\frac{{u_m}^2}{2g} + f_{bs}\frac{L_{bs}}{D_{bs}}\frac{{u_m}^2}{2g} \tag{3.69}$$

$$H_{f-minor} = \xi_{total} \frac{{u_m}^2}{2g} \tag{3.70}$$

The major head loss in the tubes and basin of the system is shown by Eq. (3.69). In this equation, the frictional factors, f_t and f_{bs} are from the Darcy frictional factor for laminar flow which is derived using the Hagen-Poiseuille equation and depends on Reynolds number (Re, is given by Eq. (3.28)) (Welty et al., 2007). The first frictional factor in Eq. (3.69),f_t, accounts for the pressure loss that occurs from the flow of water through the tubes and the second frictional factor, f_{bs}, accounts for the pressure loss that results from the flow of water across the basin. An equation for the calculation of this factor is given by Eq. (3.71). As is evident, this equation depends on the inner diameter of the tube (for f_t) or basin (f_{bs}). However, the basin does not have a diameter due to its rectangular shape and so an equivalent tube diameter (D_{bs}) for a non-circular passage can be calculated according to Eq. (3.72) using the breadth of the basin (b_{bs}) and the height of the water (Z_w) in the basin (Welty et al., 2007).

$$f = \frac{64}{Re} = \frac{64\mu}{D_i u_m \rho_w} \tag{3.71}$$

$$D_{bs} = 4\frac{cross\ sectional\ area\ of\ flow}{wetted\ perimeter} = 4\left(\frac{Z_w b_{bs}}{b_{bs} + 2Z_w}\right) \tag{3.72}$$

The minor frictional head loss is defined by Eq. (3.70). The type of fittings that result in this kind of pressure loss might include valves, elbows or other fittings that may alter the course of flow in the system. The coefficient, ξ, varies for each type of fitting and is only dependent on the roughness of the fitting (Welty et al., 2007). In order to calculate the total minor head loss in the system, one needs to sum the frictional losses in the system that result from the system configuration.

Figure 3.8 shows the different points of fitting friction in the system. These points are the Bell-mouth inlet, long radius elbows, straight through Tees and the Sudden Enlargement. To derive a total frictional coefficient for the minor losses in the system, the system can be broken down according to a series-parallel resistance scheme as shown in Figure 3.8. In this figure, each

resistor represents the frictional loss at each of the relevant fittings in the system. Consequently, the system's fitting resistance can be reduced to a single total, ξ_{total}, as shown by Eq. (3.73) with the variables in this equation, which are local to this section, shown in Table 3.8.

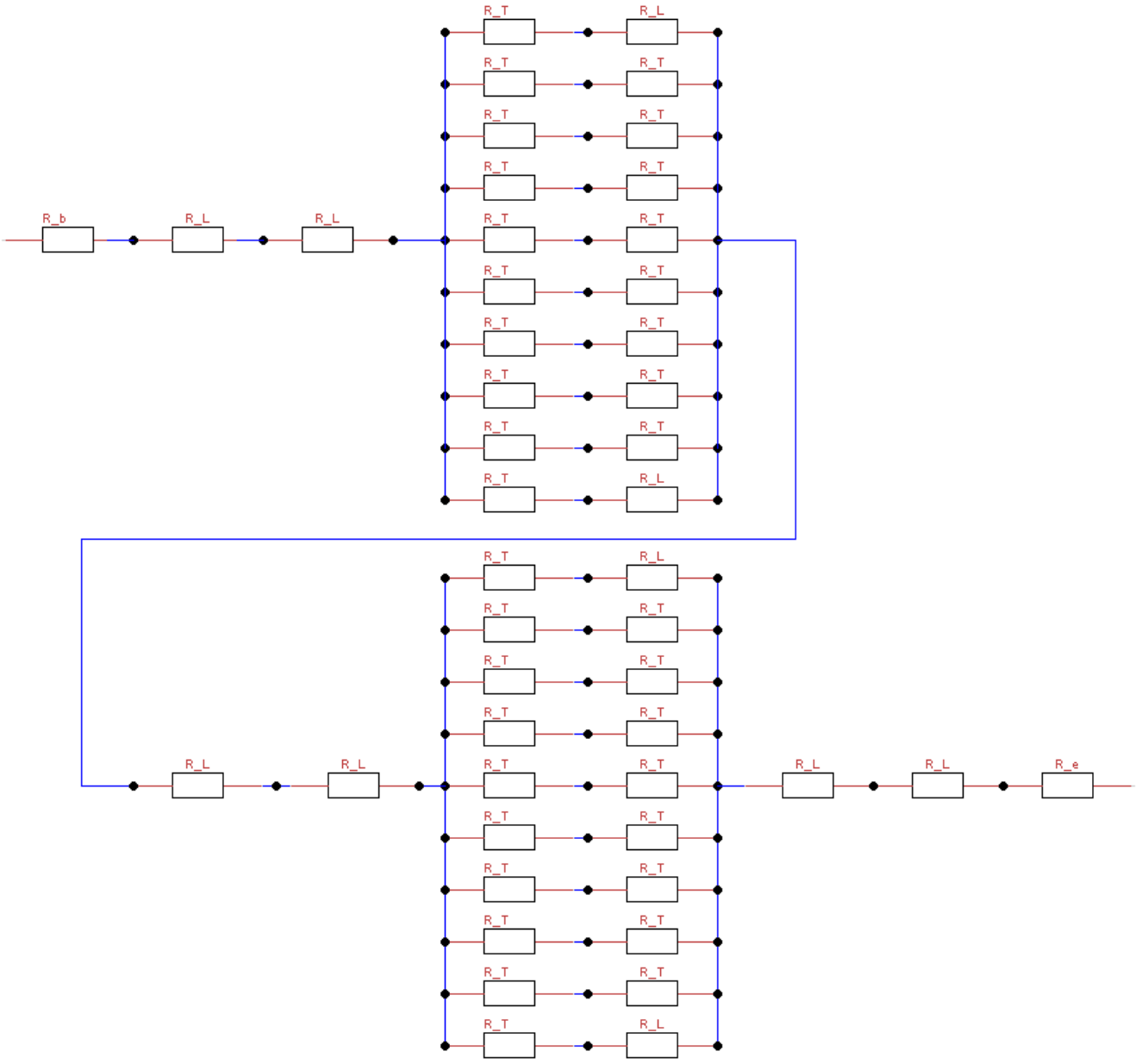

Figure 3.8: Fitting frictional coefficients

$$R_{total} = R_b + 2R_L + \frac{2R_1R_2}{8R_2 + 2R_1} + 2R_L + \frac{2R_1R_2}{8R_2 + 2R_1} + 2R_L + R_e \tag{3.73}$$

Table 3.8: Definition of variables local to Eq. (3.73)

Variable	Definition
R_b	frictional coefficient of the bell-mouth inlet
R_T	Tee-junction frictional coefficient
R_L	frictional coefficient of the long radius elbow
R_e	frictional coefficient of the sudden enlargement
R_1	Is the sum of $R_L$and R_T
R_2	$2R_T$

Table 3.9: Tube diameters and fitting frictional coefficients for1.905cm tube (nominal)

Fitting type	Nominal tube size (cm)	Frictional Coefficient (ξ)	Source
Bell-mouth inlet (R_b)	N/A	0.05	("Friction Losses in Pipe Fittings″, 2015)
Long radius elbow (R_L)	1.27	0.43	("Friction Losses in Pipe Fittings″, 2015)
Tee (through flow) (R_T)	1.27	0.54	("Friction Losses in Pipe Fittings″, 2015)
Sudden enlargement (R_e)	46.13	0.99	(Welty et al., 2007)

$$\xi_{enlargement} = (1 - \frac{D_i^2}{D_{bs}^2})^2 \tag{3.74}$$

The sudden enlargement coefficient is given by Eq. (3.74) (Welty et al., 2007). In the sudden enlargement equation, D_i denotes the tubes diameter while D_{bs} equivalent diameter of the basin, as described by Eq. (3.72). By performing these calculations for the specified 0.01905m tube in Section 3.2.3 and assuming a 0.20 water depth, the frictional coefficient for the sudden enlargement was calculated and it is given in Table 3.9.

The driving force and the frictional force in Eq. (3.69) and Eq. (3.70) respectively can be equated to find the velocity of the water in the tubes. This velocity can then be used to calculate the mass flow rate using Eq. (3.75) (Cengel, 1997; Bergman, Incropera & Lavine, 2011). Alternatively, if the pump is to be used, the system is set to run instead at a constant designated mass flow rate. In this case, the fluid velocity in the tube is calculated by manipulating Eq. (3.75) and solving for the velocity (with the given mass flow rate). From here, the total pressure head in the system is calculated according to Eq. (3.68). Finally, the required pumping power can be calculated according to Eq. (3.76) (Cengel, 1997; Lienhard IV & Lienhard V, 2008). This ultimate pumping power can then be divided by pump efficiency to give the expected power draw from the pump.

$$\dot{m} = \rho_w u_m A_t \tag{3.75}$$

$$\dot{W}_{pump} = \frac{\dot{m} g H_{total}}{\eta_{pump}} \tag{3.76}$$

3.3.4 Computation

Various numerical integration techniques exist, such as Euler Method, Modified Euler's Method and Runge-Kutta (with varying orders). Of these methods, Euler's Method is said to be the least accurate (Mathews & Fink, 1999). However, according to Jones & Underwood (2001), Euler's method can be used to derive adequate results for numerical integration. (Notton et al., 2014) also used this method in a solar collector model which was validated with an experimental design.

This method relies on initial conditions and a chosen timestep (h) to determine successive approximations of function outputs. An example is given by Eq. (3.77), for the temperature of water (T_w) (Jones & Underwood, 2001). The timestep, h, is set to 60 seconds for simulation purposes in this thesis.

$$T_w(t+1) = T_w(t) + h\frac{T_w}{dt} \tag{3.77}$$

Euler's method only deals with individual differential equations. The Jacobi Iteration Method is one way of extending this method to allow the numerical determination of simultaneous equations. This method works by inserting initial conditions into a set of differential equations to get outputs for a specific k'th estimate. These outputs are then re-inserted into the set of equations to give an estimate for the output for the set of equations at a (k+1) estimate. This process is then repeated until successive estimations of the points converge within a certain tolerance. That is to say, that the distance between successive coordinate estimations varies by less than an agreeably small amount. This process of successive 'guessing' can be sped up by inserting estimates for variables at (k+1) into successive points in a given set of simultaneous equations. This method is called the Gauss-Seidel Iteration (Mathews & Fink, 1999).

The hybrid PV/T desalination model in this thesis has a series of differential equations which require integration. Therefore, a combination of Euler's Method and the Jacobi iteration were used to determine numerical approximations for each of the variables in the set of nodal equations.

3.3.5 Solution Procedure

An overview of the algorithm used to determine the system temperatures, water and energy yields and efficiencies is illustrated in Figure 3.9. The figure is comprised of steps which are described in this section. In short, the process starts by initialising variables in the system. Thereafter, a loop starts which iterates through each day of the year. On each day variables, which change only on a daily basis, are calculated. Thereafter, another loop starts which loops

through each hour of each day and, similarly, some hourly variables are calculated at the start of each hour. Each hour is stepped through using a variable called *timeStepTicker* in increments of 1 up to a maximum time of (3600/h) (where h is the time step (h) shown in (3.77). For every increment of *timeStepTicker,* a function called *wholeSystem()* is executed. This function is responsible for employing the numerical methods (discussed in Section 3.3.4.) to solve the simultaneous differential equations for the different nodes within the system.

This section breaks down descriptions of the different calculations that take place in Figure 3.9 according to the frequency at which they are performed. For example, some calculations are only undertaken once in the entire simulation, some daily, some hourly and some at intervals of *timeStepTicker*.

Figure 3.9: Overview of algorithm for the PV-T system (main)

The once-off calculations are composed of 3 parts as shown in Figure 3.9. The variable initialisation takes place in a function called *VariableConstructor()*. This function sets up all the initial properties of the system and the structural properties of the system (as per design), and those variables pertaining to the material properties are stored in a structural vector called *materialProperties*. Those related to structural dimensions are stored in a structural vector called *structuralProperties*. Lastly, those variables that are constants that pertain neither to specific materials or dimensions are stored in the *constants* structural vector. These structures are used so that groups of related variables can easily be passed into functions instead of being individually passed.

Once the constants in the system have been initialised, additional data is read into the system through the function *ReadingIn()*. This function simply stores irradiation data (horizontal normal and diffused), wind speed and ambient temperature into the *weatherProperties* structural vector and the latitude, longitude and standard longitude into the *coordinates* structural vector.

The last once-off calculation is for the hourly heat transfer coefficients that do not depend on fluctuating system temperatures. In this case, only the variables $h_{c,g}$ and $h_{\Psi a}$ are calculated using the function *CalcHourlyTransfCoeffs()* as they depend on the hourly wind speed.

There are only two main variables that change every day. These variables are respectively the declination and the sunset/sunrise hour angle. These variables are each calculated with *CalcDeclination()* and *CalcSunSetRiseOmega()*. These functions fundamentally employ Eqs. (2.23) and Eq. (2.35) to perform these calculations.

The hourly calculations are broken down into three types of calculations. The first type is for angle calculation (incidence and refraction), the second is for R_b values and the last is for determining incident heat on the different components in the system.

The incidence and refraction angle variables are first calculated with the functions *CalcIncidence() CalcRefraction()*. These functions rely on Eqs. (2.19) and (2.17) respectively. The first of the two functions returns the angle of incidence for the PV panel and collector configuration and for the solar still. The second calculates the refraction angle only for the PV panel and collector configuration. The incidence angle and refraction angle for the PV panel and collector configuration are used to calculate the heat components on the glass and PV

panels in the system, while the incidence angle returned for the still is used to calculate the incident heat components within the solar still.

The R_b values for the PV panel and collector configuration and the solar still are calculated separately so that the two parts of the system can be oriented differently if need be. That is, if the azimuth indicates a subsystem is South facing, the first part of Eq. (2.30) is used, otherwise if it is North facing, the second part is used. This function returns R_b values that correspond to the R_b values of the previous hour's midpoint. In other words, for 6:00 am's irradiation values, a R_b value corresponding to 5:30 am is used. In addition, these R_b values are set to 0 when the sun is behind the earth (for hours before and after sunset) and, if it is the sunset or sunrise hour, the average R_b value for that hour is used as discussed in Section 2.2.3.1.

The heat components on the PV panel and collector configuration and solar still are calculated with functions CalcPVHeatInput*()* and *CalcStillHeatInput()*. These functions discern whether they should pass the instantaneous R_b value or pass sunrise/sunset average R_b value on towards functions that are directly responsible for calculating the different heat components in the different systems. These functions are *CalcPVTIrradiation()* and *CalcStillIrradiation()* respectively and they use equations given in Section 2.2.3 to determine the irradiation and heat components necessary for further calculations.

The simultaneous differential equations for the entire system are calculated at every increment of *timeStepTicker*. This task is carried out by the *wholeSystem()* function at intervals defined by the variable *h* (See Section 3.3.4). This function, which is where the majority of the calculations are undertaken, returns the component temperatures, power output, the water flow rate and the evaporative heat transfer coefficient at each time interval. The details of what occurs in *wholeSystem()* are shown in Figure 3.10.

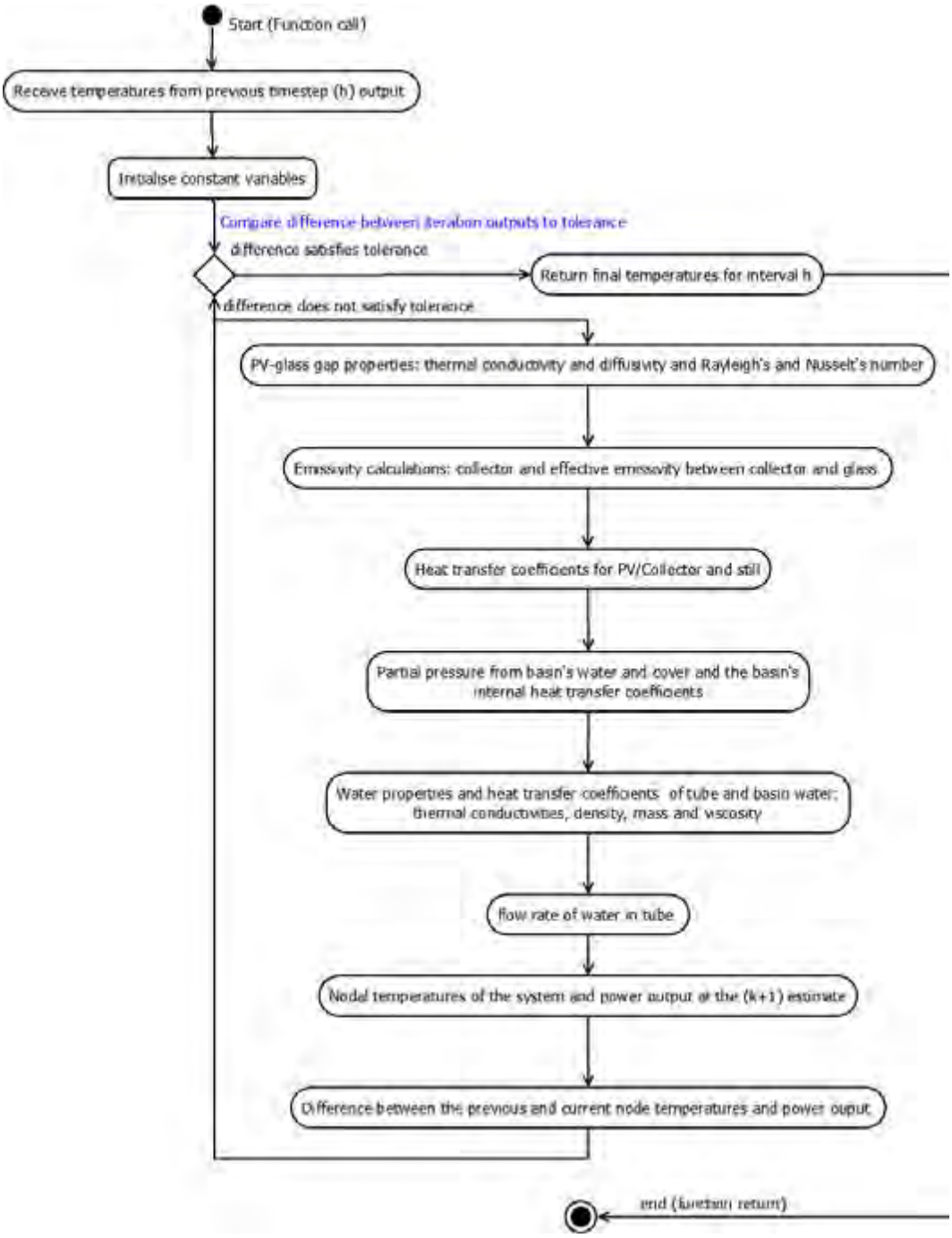

Figure 3.10: Flow diagram for the wholeSystem(...) function

To calculate the heat transfer coefficients between the PV panel and the glass and the collector and the glass, the air properties within these respective segments of the system needs to be determined. To do this, three temperature dependent correlation functions are used (Mathur & Mathur, 2006). These functions help determine the air's approximate properties at specific mean fluid temperatures and are provided for in Appendix D. The first function, is used to

approximate the thermal conductivity of air (K_a), another the thermal diffusivity of air (κ_a) and the last one, the kinematic viscosity of air (v_a) . Next, the coefficient of expansion for air (β') is calculated according to Eq. (3.8) which is used in conjunction with the interpolation derived air properties in the calculation of Rayleigh's (Ra) number according to Eq.(3.5). Thereafter, Rayleigh's number is used to calculate the Nusselt number for the air between the two surfaces (Nu_a) (Eq. (3.4)) which in turn is used to calculate the convective heat transfer coefficients between the panels and the glass. Lastly, to calculate the radiative heat transfer coefficient between these surfaces, the effective emissivity between the glass and the collector and panel is calculated using a constant emissivity for the glass and panels, and a temperature dependent interpolation derived value is used for the collector. The convective and radiative heat transfer coefficients are then used to calculate the total heat transfer coefficients between the glass and panel (h_{gp}) and glass and the collector (h_{gq}) according to Eq. (3.2).

The radiative heat loss from the top of the glass($h_{r,g}$) is calculated according to Eq. (3.12), while the convective heat loss of the panel is calculated according to Eq. (3.11) ($h_{c,g}$) with similar heat transfer coefficients being calculated for the cover of the still ($h_{r,k}$ and $h_{c,k}$). Additionally, the convective heat transfer coefficient is combined with the conductive heat transfer coefficient for the basin bottom and sides to give an overall heat transfer coefficient for the basin bottom (h_{bb}) sides (h_{bd}) as shown in Eq. (3.63).

The partial pressures for the cover and water in the solar still (P_k and P_k) are first calculated according to Eqs. (3.44) and (3.45). On condition that the cover temperature is lower than the water temperature, these partial vapour pressures are used to calculate the convective heat transfer for the still (Eq. (3.42)) within the basin which can in turn be used to determine the evaporative heat transfer in the system (Eq. (3.43)). Separate from the convective and evaporate heat transfer coefficient, the radiative heat transfer coefficient in the still is calculated according to Eq. (7.6). These three heat transfer coefficients are combined to provide an internal total heat transfer coefficient for the basin, h_{lw}.

The thermophysical properties of water within the tube and the basin (which have different mean temperatures) are then determined so that the heat transfer coefficients between the water and the tube (h_{tw}) and the water and the basin (h_{bw}) and the water mass flow rate in the system can be found. If the flow in the tube is laminar, only the thermal conductivity of the water is needed (Eq.(3.30). Otherwise, if flow is not laminar in the tube, Nusselts' number must be determined (Eq. (3.29) which requires the determination of other thermophysical properties.

The required thermophysical properties are the: thermal conductivities, densities, and viscosities of water. The thermal conductivities of the water in the tube and basin are first calculated using the appropriate average temperatures and an equation for the thermal conductivity of saline water (Eq. (7.30)). The same is done for the densities of water (so that the mass of the water in the tube and basin can be attained), specific heats and dynamic viscosities according to Eqs. (7.11), (7.25) (7.31) respectively. However, in the case of the basin, as mentioned in Section 3.3.1.2.4, the flow is always assumed laminar so only the thermal conductivity is needed for water in the still. Once the heat transfer coefficient has been found for the tube, it can be used to find the thermal conductance between the tube and the water in the tube (Eq. (3.27)). Additionally, these thermophysical properties are also then used to establish the mass flow rate in the system (Section 3.3.3).

Lastly, *wholeSystem()* calculates the main system output variables using the approximation methods laid out in Section 3.3.4. These outputs are $T_g, T_p, T_b, T_t, T_\Psi, T_w, T_{w1}, T_\kappa, T_{bs}$ and E_p, with the temperature components being approximated from the differential equations laid out in Section 3.3.1.2 and Section 3.3.2.2. This function returns these variables, along with the evaporate heat transfer coefficients, to the main function (illustrated in Figure 3.9). The evaporative heat transfer coefficient is used to calculate the water yield for this time interval which is calculated with function *CalcIntervalWaterYield()* (Eq. (3.64)). The total available energy available as well as the total energy produced by the panel in the interval are stored for this interval. These yields are summed for each day, month and year to give yield totals as required.

3.4 Model Validation

3.4.1 Required Design Changes

The models (Model 1 and Model 2) for the design presented in Section (3.2) needed to be validated against experimental data. This was necessary so as first to verify that the model does not behave in a way that is excessively dissimilar from reality. To do this, experimental data was required. However, due to a lack of readily available data, data from an existing study's experiment was used. An experimental study by Kumar & Tiwari (2008a) uses the same basic

design as the design presented in Section 3.2 and, in addition, the paper presents input data (irradiation values and ambient temperatures) and output data (still component temperatures the hourly water yield) for an experimental system for a single day, 14 April, 2006. However, this paper does not present all the design parameters for the system. Nevertheless, the same design persists in other papers by the same author and these papers present the other design parameters essential for validation (Kumar & Tiwari, 2010; Dev & Tiwari, 2010).

The dimensions and properties for the validation PV and collector configuration, those that differ from the properties and dimensions presented in Section 3.2, are given in Table 3.10. The type of PV panel is not provided in any of the papers used for the model validation. It was therefore assumed that system employs a polycrystalline silicon (pc-Si) panel due to the popularity of these types of panels (See Section 7.2). Also, the specifications regarding the bonding between the plates were not given, and the collector material type is not provided. Therefore, it was assumed that the experiments were conducted using materials used in PV/T models such one implemented by Chow (2003). The experiment by Dubey & Tiwari (2008) uses a tilt angle of 45° for the PV panel and collector configuration and the location of the site is 28°32’ N, 77°12’ E. The PV of the system employs an insulation thickness of 10cm, which is made from glass wool, to insulate the base of the PV/T collector (Kumar & Tiwari, 2010). In in a similar way, the solar still dimensions and properties of the validation design, are given in Table 3.11.

Table 3.10: *Experimental PV and collector dimensions and properties that differ from System design*

Source: (Kumar & Tiwari, 2010)

Parameter	Value
Total area of glass cover (A_g)	2× (1.9m×1.25m)
Glass cover thickness	0.004m
Absorber plate area under the PV module (A_b)	1.25m×0.55m
Insulation Thickness (δ_Ψ)	0.01m
Number of tubes per collector	10
Number of collectors	2
Power output (E_p)	75W
Tilt Angle (β_p)	45°

Table 3.11: Experimental solar still dimensions properties (aspects that differ from Section 3.2.2)

Component	Value	Source
Depth of water (δ_k)	0.05m	(Kumar & Tiwari, 2010)
Back height	1.18m	(Kumar & Tiwari, 2010)
Front height	0.06m	(Kumar & Tiwari, 2010)
Basin (walls and floor) thickness	0.005m	(Kumar & Tiwari, 2010)
Glass Cover Thermal Conductivity (k_k)	0.78 $Wm^{-1}K^{-1}$	(Dev & Tiwari, 2010)
Basin Thermal Conductivity (k_{bs})	0.0351$Wm^{-1}K^{-1}$	(Dev & Tiwari, 2010)
Basin Heat Capacity (C_{bs})	2.3$kJkg^{-1}°C^{-1}$	("Guide to Glass Reinforced Plastic…", 2015)
Density of basin (walls and floor)	1190kgm^{-3}	Derived from the weight of the basin (Kumar & Tiwari, 2010) and the volume of the basin (Dev & Tiwari, 2010)
Mass of water in basin (M_{bw})	50kg	(Dev & Tiwari, 2010)
Mass of water in tube (M_{tw})	5.68kg	See Section Table 3.11
Mass of basin (M_{bs})	21.17kg	(Dev & Tiwari, 2010)
Tilt (β_k)	30°	(Kumar & Tiwari, 2010)

Section 3.2.3 discusses major and minor frictional losses and their relation to tube diameter and system fittings. Concerning major head losses, the validation experiment also uses a copper tube but instead with a nominal tube diameter of 0.01270m and has other dimensions shown in Table 3.6 (a schedule 40 tube assumed). For the minor head losses, the fitting resistances in the system were not stipulated in the papers used for validation and so, as flow rate is fixed to a set value which does not alter for different head losses in the system (where the power requirement for that flow rate does), the same fitting resistances as in the designed system (Section 3.2) were used. See Section 3.3.3 for details regarding the frictional resistance.

Table 3.12: 1.270cm (nominal) tube dimensions (Welty et al., 2007)

Attribute	Size (m)
Nominal Diameter	0.01270
Outside Diameter (D_o)	0.02134
Inside Diameter (D_i)	0.01580
Wall thickness	0.00277

The validation model is an active system with circulation being achieved by a 60W and 16V pump as described by Dubey & Tiwari (2008). However, neither the actual power drawn by the pump nor the system water flow rate are provided in the papers used for validation. This lack of information is not presumed to be critical to the validation model as thermal efficiency does not vary significantly with different flow rates nor are flow rates a dominating determinant of system performance. A study by Bergene & Løvvik (1995) showed that there was only a 10% increase in thermal efficiency of a PV/T system when the flow rate was increased from 0.001kgs^{-1} to 0.075 kgs^{-1}. Additionally, as mentioned in Section 3.2.1.1, the performance of PV/T systems is said to be dominated by the heat transfer coefficients between the panel absorber plate and the absorber plate and the tubes. Thus, verifying the model with a 'reasonable' flow rate seemed adequate as the system's performance is more largely determined by these heat transfer coefficients, which have themselves also not been provided for in the validation literature.

A suitable flow rate for the validation model was found by averaging the optimal flow rate range as found in literature. Charalambous et al. (2007) presents optimal flow rates in the range of 0.001kgs^{-1}m^{-2} to 0.008kgs^{-1}m^{-2}. Therefore, the average flow rate of this range (0.018 kgs^{-1}, taking area into account) was considered as a 'reasonable' flow rate for this design.

3.4.2 Tools for Validation

3.4.2.1 Error Analysis

Root Mean Square Error (RMSE and Mean Bias Error (MBE) are commonly used as a means of determining the differences between theoretical and experimental results of hourly water

output (Tiwari & Tiwari, 2007b; Deniz, 2012; Sampathkumar et al., 2013). These error metrics are given by Eq. (3.78) and Eq. (3.79) (Deniz, 2012). Another error metric, shown by Eq. (3.80), is the Mean Absolute Error (MAE). As can be seen from the governing equations, RMSE is a function of MAE (with the difference being due to the square and square-root terms in RMSE equation) (Willmott & Matsuura, 2005).

Total RMSE values, compared to MAE errors, are influenced to a greater extent by large error components in the data. This is because each error influences the total RMSE value in proportion to the size of the square of each error (this has been a criticism of this error measurement compared to the MAE error). The MBE, on the other hand, gives an overall indication of the extent to which a model overestimates or underestimates with its outputs (that is, the overall error bias). This is due to the inclusion of the original signs in the error terms (Willmott & Matsuura, 2005). As other PV/T desalination systems often report RMSE values (Tiwari & Tiwari, 2007b; Deniz, 2012; Sampathkumar et al., 2013), this metric is used in this thesis

$$RMSE = \left(\frac{1}{N_{ob}} \sum_{i=1}^{n} \left| \frac{X_i - Y_i}{Y_i} \right|^2 \right)^{\frac{1}{2}} \tag{3.78}$$

$$MBE = \frac{1}{N_{ob}} \sum_{i=1}^{n} \left(\frac{X_i - Y_i}{Y_i} \right) \tag{3.79}$$

$$MAE = \frac{1}{N_{ob}} \sum_{i=1}^{n} \left| \frac{X_i - Y_i}{Y_i} \right| \tag{3.80}$$

3.4.2.2 Correlation

Correlation, see Equation (3.81) (Chapra & Canale, 2012), is one way of determining how well models fit with experimental data and it has been used in PV/T model validation (Tiwari & Tiwari, 2007b; Deniz, 2012; Singh et al., 2012; Sampathkumar et al., 2013). The output (the R-value) of this function has no units and ranges between "-1" and "1" depending on the degree of linear association between data sets. If the R-value is negative, a negative linear relationship

exists between the theoretical value and the experimental output. The 'perfection' of this negative relationship is indicated by how close the R-value is to"-1". Likewise, a positive r-value corresponds with a positive linear relationship between data and the extent of closeness being indicated by how close the value is to "+1". Values that approach 0 indicate little association between variables (Dowdy, Wearden & Chilko, 2004). It should be noted that this equation, however, is unable necessarily to determine a good fit between data sets because inherently non-linear data may even yield R-values that indicate a strong linear relationship. Consequently, it is recommended that the relationships between data is also always inspected on a plot (Chapra & Canale, 2012).

$$r_{cor} = \frac{N\sum Y_i X_i - (\sum Y_i \sum X_i)}{\sqrt{N\sum {X_i}^2 - (\sum X_i)^2}\sqrt{N\sum {Y_i}^2 - (\sum Y_i)^2}} \quad (3.81)$$

3.4.2.3 Models with Validation

Tiwari & Tiwari (2007b) undertook a study to determine the performance of a single slope solar still with varying water depth. The study reported the water mass yield RMSE and correlation values for different water depths. The experiment was conducted in India (New Delhi) with model results being validated for a single winter (January) and summer (May) months.

Tripathi & Tiwari (2004) carried out a study to determine the effect of accounting for the solar fraction within a solar still (reflection off of the walls). The study was undertaken in India (New Delhi) and consisted of an experimental and modelling component. The experimental setup was used to validate the model for a single day in March, and RMSE and correlation values were used to perform the validation.

Sampathkumar et al. (2013) performed a numerical model to ascertain the performance of a single basin hybrid PV/T desalination system with evacuated tubes. This model was then verified by building an experimental device and comparing the results from the model and the experiment. The paper quantified the RMS error for the temperatures of the inner ($T_{k\Psi}$) and outer (T_{ko}) parts of the cover, the temperature of the water (T_w) in the basin, the basin

temperature (T_{bs}) and the hourly water mass yield from the still (M_w). Also, the paper reports correlation value for the temperature of the water (T_w) in the basin and the water mass yield (M_w). The paper used a basin water depth of 5cm, as in this thesis and was conducted under India's (Coimbatore) climatic conditions for a single day in 2009.

Deniz (2012) performed a similar experimental and modelling study, with the same water depth, but under Turkish climatic conditions. This paper only reported on the RMSE and correlation values for the water mass yield (M_w). The results of this paper were also given for a single day of operation.

Singh et al. (2012) undertook a study to test the performance of an active hybrid PV/T desalination system with a double slope basin connected to two flat plate collectors. The study similarly implemented a model and validated the model through an experimental configuration and reported on correlations pertaining to the temperature of the water in the basin (T_w) and the cover temperatures (T_{ko}, T_{ki}) (Note, the cover temperatures are reported for both the east and west cover of the still). The model was validated under India's (New Delhi) climatic conditions and validation was performed for a single day in October.

3.4.3 Procedure

To validate the numerical model, parameters of Model 1, the view factor model, were changed to conform to the parameters of an experimental study (as described in Section 3.4.1). Thereafter, the RMSE values between the model outputs (water yield and solar still component temperatures) and the experimental outputs were determined using Eq. (3.78). Similarly, the correlation values for the outputs were also determined.

After validating the performance of Model 1, the RMSE and correlation values were found for Model 2, the no-view-factor model. The RMSE values and correlation values of both Model 1 and 2 were then compared to determine which of the two models predict the performance of designed hybrid PV/T desalination system more accurately.

3.5 Sensitivity Analyses

Sensitivity analyses were undertaken to determine the optimal water depth and the tilt angle (PV panels and still cover) required to achieve maximum electrical efficiency in the system. This entailed maintaining all, except one, of the parameters constant while a single parameter was varied. Before performing the sensitivity analyses, a default case simulation was run. This simulation was undertaken so as to give an indication of how system performance varies on a monthly and seasonal basis and, to demonstrate the ability of the model to establish an hourly performance profile. Thereafter, sensitivity analyses for water depth, PV tilt angle and solar still tilt angle were performed.

The default performance was established by running the system with design specification parameters with radiation data for a site in Stellenbosch, South Africa (33.935°S 18.7817°W) over the course of a year. Radiation (tilted vs. horizontal), temperature (of system components) and hourly efficiencies (thermal, electrical and total efficiency) profiles were plotted for a typical summer day (15 January 2007). Thereafter, performance results (yields and efficiencies) were summarised for every month of the year.

For water depth sensitivity analysis, the water depth was varied between 0.02m and 0.04m while all other parameters were kept constant (Panel Tilt angle: 34º, Still Cover Tilt angle: 34° and Flow Rate: 0.018kgs^{-1}). For each depth, the total water yield and electrical energy yield were plotted alongside the thermal and electrical efficiencies of the system over the course of the year.

For the PV sensitivity analysis, the tilt angle was varied in a similar way to that of the water depth, this time varying PV tilt angle between 10º and 60º with the other parameters held constant (water depth: 0.2m, Still Cover Tilt angle: 34° and Flow Rate 0.018kgs^{-1}). The same output yields and efficiencies were plotted as for water depth sensitivity analysis. The cover tilt angle sensitivity analysis was undertaken in the same way as the PV panel tilt angle sensitivity analysis. This time, however, the PV tilt angle was held constant, and the solar still cover tilt angle was varied (water depth: 0.2m, Panel Tilt angle: 34º and Flow Rate0.018kgs^{-1}).

4 Results and Discussion

4.1 Introduction

This chapter provides results and discussions of model validation for Model 1 (the view-factor model) and Model 2 (the no-view-factor model) (Section 4.2), a default case run (also for both models, Section 4.3) and sensitivity analyses (for Model 1 only, Section 4.4) for the hybrid PV/T desalination system model/s. The chapter starts with a presentation of the validation results (Section 4.2) of Model 1 and Model 2. Results are then discussed with reference to hourly water yield profiles, RMSE and correlation values.

After model validation, the performance of Model 1 under default parameters (panel tilt angle: 34°, still cover tilt angle: 34°, water depth: 0.2m, flow rate: 0.018 kgs^{-1}) at the site location (33.935°S 18.7817°W) for the year of 2007 is analysed (Section 4.3). The performance of the system is shown (Section 4.3.1) for a single summer's day (15 January 2007) and it is indicated with respect to plotted irradiation, temperature profiles, hourly efficiencies and the internal heat transfer coefficients within the basin. Importantly, these internal heat transfer coefficients are given for both Model 1 and Model 2. This was done to show how the view factor affects internal heat transfer coefficients of the still (this could not be done in the validation section because internal heat transfer coefficient data was not available for the experiment). After providing the daily results, monthly results are presented with respect to yields and efficiencies (Section 4.3.2).

After the default case run results have been presented, sensitivity analyses are given (Section 4.4). These analyses were performed using Model 1 for water depth and tilt angle as described in Section 3.2. Model 1 was used because validation (Section 4.2) indicates a higher accuracy than Model 2. Furthermore, the inclusion of a view factor is said become more important in solar still tilt angle sensitivity analysis when a steeper tilt angle is used (El-Maghlany, El-Samadony & Kabeel, 2015). This section first presents (Section 4.4.1) a sensitivity analysis for a water depth variation between 0.02m and 0.4m with other parameters held constant (Panel tilt angle: 34º, still cover tilt angle: 34° and flow rate: 0.018kgs^{-1}). Thereafter, the tilt angle of the panel is varied while keeping the solar still cover angle and other variables constant (Cover angle: 34°, Water depth at 0.02m, Flow Rate: 0.018kgs^{-1}). Likewise, the solar still cover angle

is varied while keeping panel tilt angle and other variables constant (Panel tilt angle variation: Section 4.4.2, Cover tilt angle variation: Section 4.4.3).

4.2 Model Performance

The hourly water yields of the experiment, Model 1 and Model 2 are shown in Figure 4.1 As can be seen from this graph, the water yields of Model 1 track the experimental yields more closely than Model 2. Furthermore, the hourly water yield of Model 1 peaks at about the same hourly water yield peak as the experiment. Also, Model 1 has a yield decay in later hours of the day that is more similar to the experimental yield decay than that of Model 2. It should also be noted that the hourly yields of both Model 1 and Model 2 peak at the same time as the experimental yield (14:00).

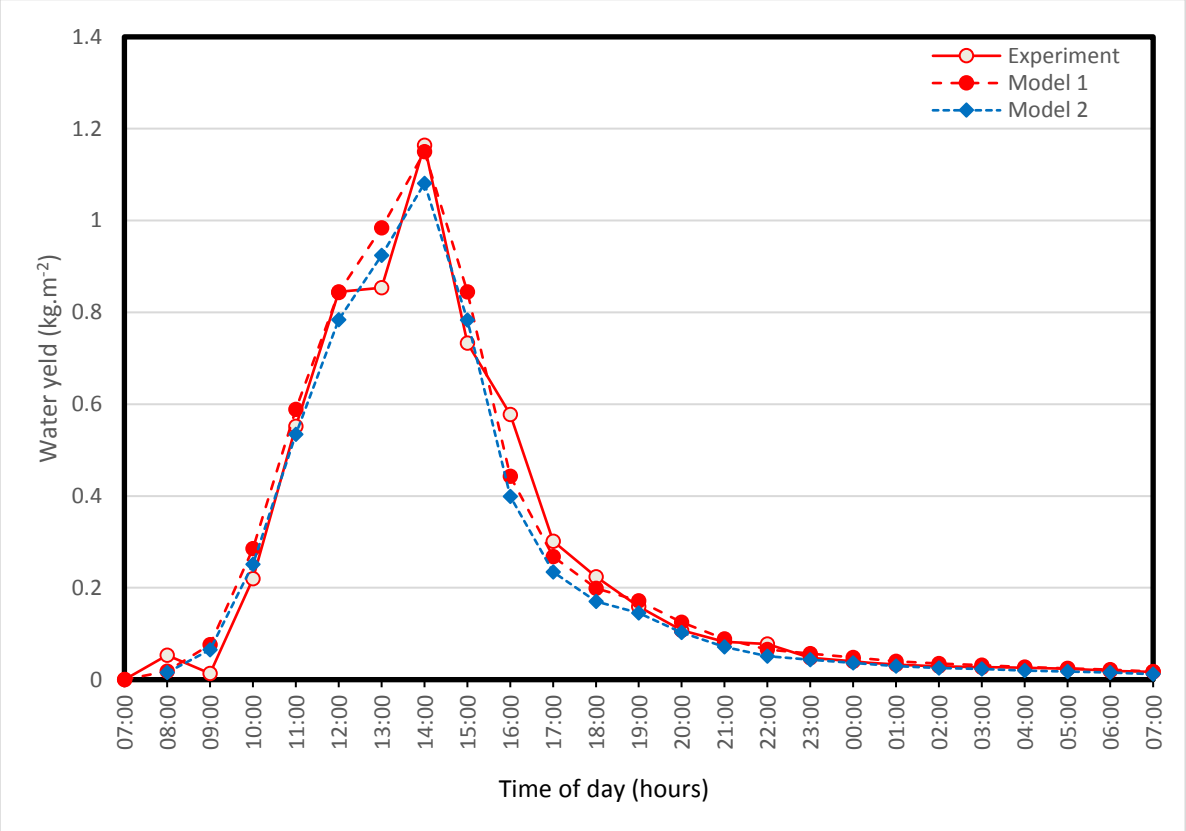

Figure 4.1: Hourly water yields for experimental data (Kumar, Tiwari & Gaur, 2010) and Model 1and Model 2

The yield accuracy of both models is quantified numerically with RMSE and correlation values as shown in

Table 4.1**.** As can be seen from this table, the RMSE values for yield improve from 28.9% in Model 2 to 22.0 % in Model 1. Also, the correlation values improve from 0.9890 in Model 2 to 0.9896 in Model 1.

Table 4.1: RMSE and correlation values for water yield

Model	RMSE (%)	Correlation Coefficient (dimensionless)
Model 1	22.0	0.9896
Model 2	28.9	0.9890

The validation of simple solar stills and PV/T systems were discussed in Section 3.4.2.3. Previous studies provide a range of RMSE and correlation values that give an indication of this present study's accuracy in predicting hourly water yields within a solar still. For example, one solar still study had water yield RMSE and correlation values of 48.5% and 0.9778 respectively (Tiwari & Tiwari, 2007b), while another had RMSE and correlation values of 32.1% and 0.9970 respectively (Tripathi & Tiwari, 2004). For a study with a solar still coupled with evacuated tubes, RMSE and correlation values of 39.7% and 0.9804 were found (Sampathkumar et al., 2013). No RMSE and correlation values were found for a hybrid PV/T desalination system. However, these values from similar studies give an indication of what range of values is reasonable for this study. In light of this, RMSE and correlation values of this thesis are in agreement with those from the mentioned studies.

Furthermore, the results from Table 4.1 indicate that the use of a view factor in modelling a hybrid PV/T desalination system reduces the RMSE of water yield by about 7%. This improvement in model accuracy is consistent with a study by Madhlopa (2014), which found an RMSE improvement when a view factor was incorporated into a solar still model. However, the results were not reported in comparable units. Nonetheless, this present study's results seem to concur with the trend of improved model performance with the inclusion of the radiative view factor in the solar still.

4.3 Default Case

4.3.1 Daily Performance

The solar radiation received on the horizontal and the tilted surfaces are shown in Figure 4.2. This graph shows how available radiation increases throughout the course of the day and falls off in the evening. More significantly, it also shows how the surface tilt angle effectively decreases the amount of received hourly radiation for this summer's day. This is consistent with literature as the tilt angle of a surface is optimised to receive maximum radiation over the course of an entire year when it is set to the latitude of a particular location. That is, to maximise radiation in summer, the slope should be lower than the latitude (by about 10° to 15°) and in order maximise radiation in winter, the tilt angle should be higher than the latitude (by about 10° to 15°) (Duffie & Beckman, 2013). As a result of this annual optimisation, there is a slight loss in radiation over summer months.

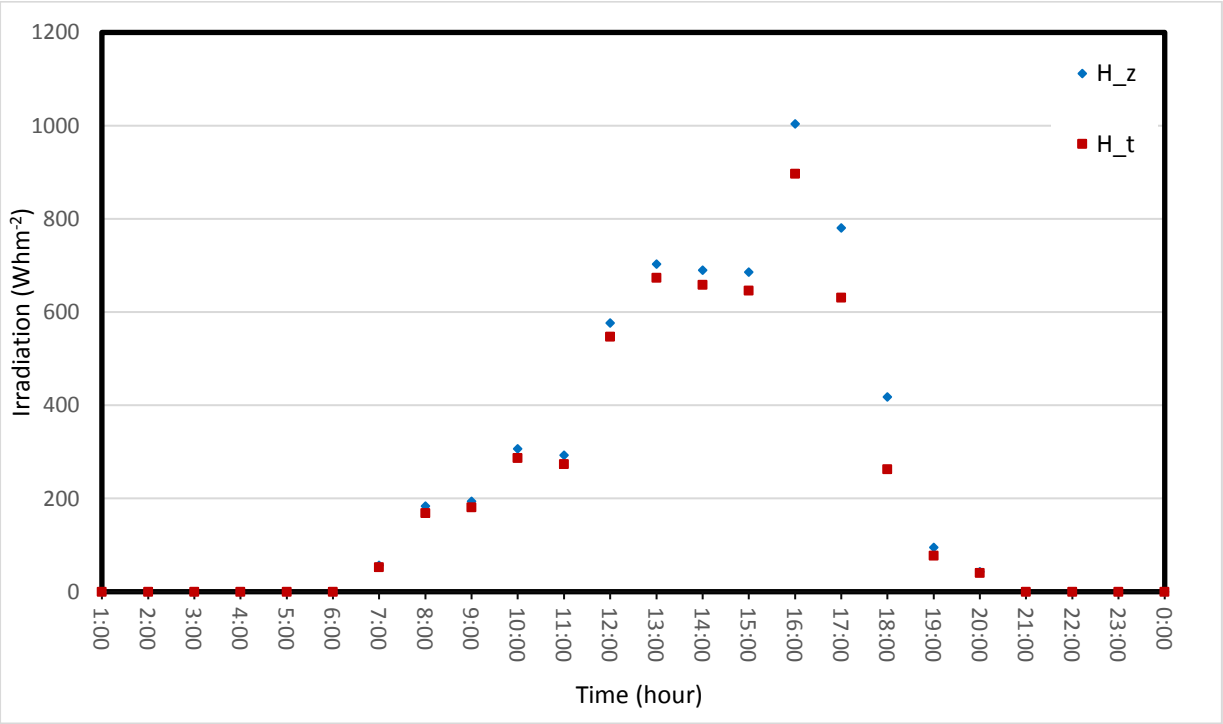

Figure 4.2: Global Horizontal Irradiation and Global Tilted Irradiation (summer: 15 January 2007)

The temperature profiles for the system for the selected summer day is shown in Figure 4.3. These results show general trends as highlighted below:

- The temperatures of the components rise during the day as radiation is received from the sun and falls off at night.
- In the hybrid PV/T desalination system, during the hottest times of day, the relative order of magnitude in temperatures is panel glass, panel, tube and the temperature of the water in the tube. The temperature stratification in the system can be accounted for by thermal conductivity and capacitance of the different components of the system. That is, as certain components receive heat, some heat goes towards heating the component and some flows towards other components. The thermal resistivity and capacities of each component thus determine how much heat flows out of each node and how much heat goes towards raising the temperature of each node.
- During the day, the temperature of the water in the tube rises higher than the temperature of the water in the basin, but once the sun sets, this temperature falls away quickly while the basin water stays warm. The temperature of the tube water rises higher than the temperature of the basin water because it is heated further by incidence heat from the collector. After sunset, however, heat quickly dissipates from the tube water because, compared to the basin water, it is a smaller thermal mass (at a 0.2m depth, the mass of water in the tube is 15kg, and the mass of the water in the basin is 205kg). The thermal inertia in PV/T systems is one of the reasons why dynamic models are chosen over steady-state models (Zondag et al., 2002).
- The inner cover of the solar still reaches higher temperatures than the outer cover of the still. The solar still's inner cover temperature gets warmer than the outer cover because the inner cover receives heat from the surface of the water (convective, radiative, evaporative) and heat is removed more quickly from the outer cover because of convection and radiation. This temperature trend is consistent with literature (Al-Hinai, Al-Nassri & Jubran, 2002; Kumar, Tiwari & Gaur, 2010).

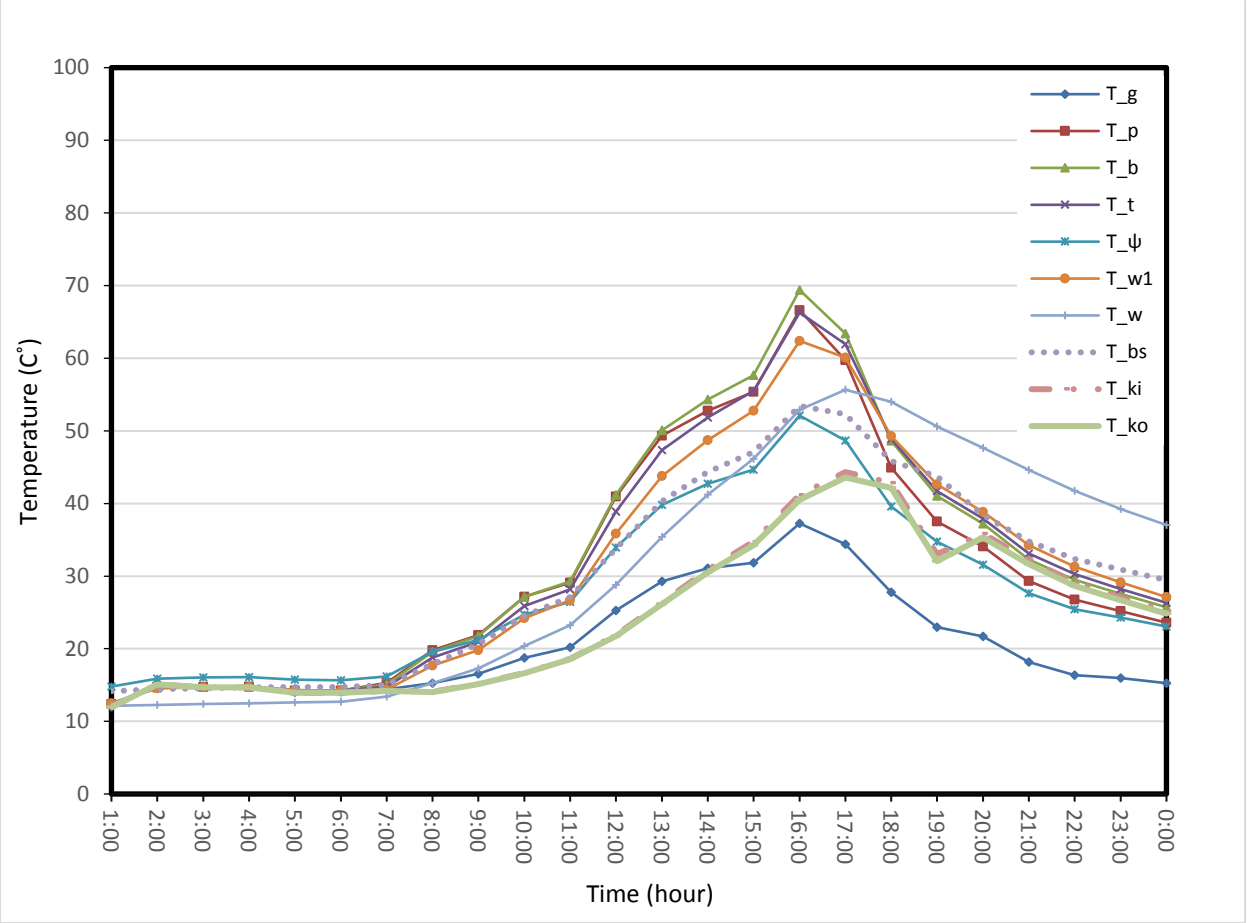

Figure 4.3: Hybrid PV/T Desalination System Component Temperature Profile (summer: 1 January 2007)

The hourly efficiencies and panel temperatures are given in Figure 4.4. This figure shows that the electrical efficiency drops off as the panel temperature rises and that the thermal efficiency steadily rises throughout the day to peak at sunset. The drop-off in electrical efficiency with an increase in panel temperature can be accounted for by the fact that PV panels become more inefficient the warmer they get (see Section 2.3.3). On the other hand, the rise in thermal efficiency occurs because more heat is stored in the water as the day progresses and so less additional heat is required to evaporate water and thus bring about a water yield. This is particularly evident at sunset where radiation is minimal, but the basin water temperature is high and so hourly thermal efficiency is high.

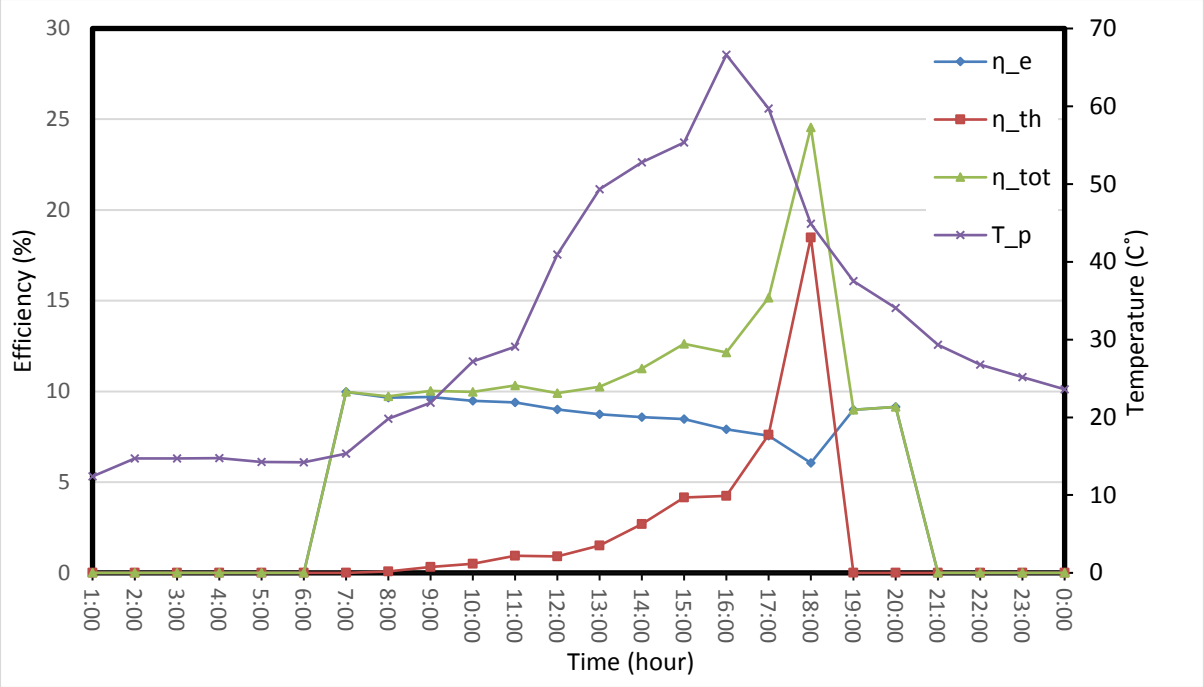

Figure 4.4: Temperature Profile of Panel and Thermal, Electrical and Total Efficiencies (summer: 1 January 2007)

The internal heat transfer coefficients for Model 1 and Model 2 are shown in Figure 4.5. This graph shows how the radiative heat transfer coefficient of Model 2 is considerably higher than the radiative heat transfer coefficient of Model 1. From this figure, it can be seen that in Model 1 the radiative heat transfer coefficient peaks at about 2.1 $W.m^{-2}K$, while Model 2's radiative heat transfer coefficient peaks at about 8.3 $W.m^{-2}K$. The smaller radiative heat transfer coefficient in the view factor model is consistent with previous studies (Madhlopa, 2014; El-Maghlany, El-Samadony & Kabeel, 2015) and also explains why the hourly water yields of Model 1 are higher than the yields of Model 2 in model validation (Section 4.2). These water yields are higher because the water temperature in the basin is warmer in Model 1 than in Model 2 as less heat is lost to the cover (the thermal radiative thermal resistance is greater with the view factor) (El-Maghlany, El-Samadony & Kabeel, 2015). These factors, therefore, result in an overall temperature difference between the water and the cover which is greater in Model 1 than in Model 2, which in turn results in a higher water yield (Tiwari & Tiwari, 2008).

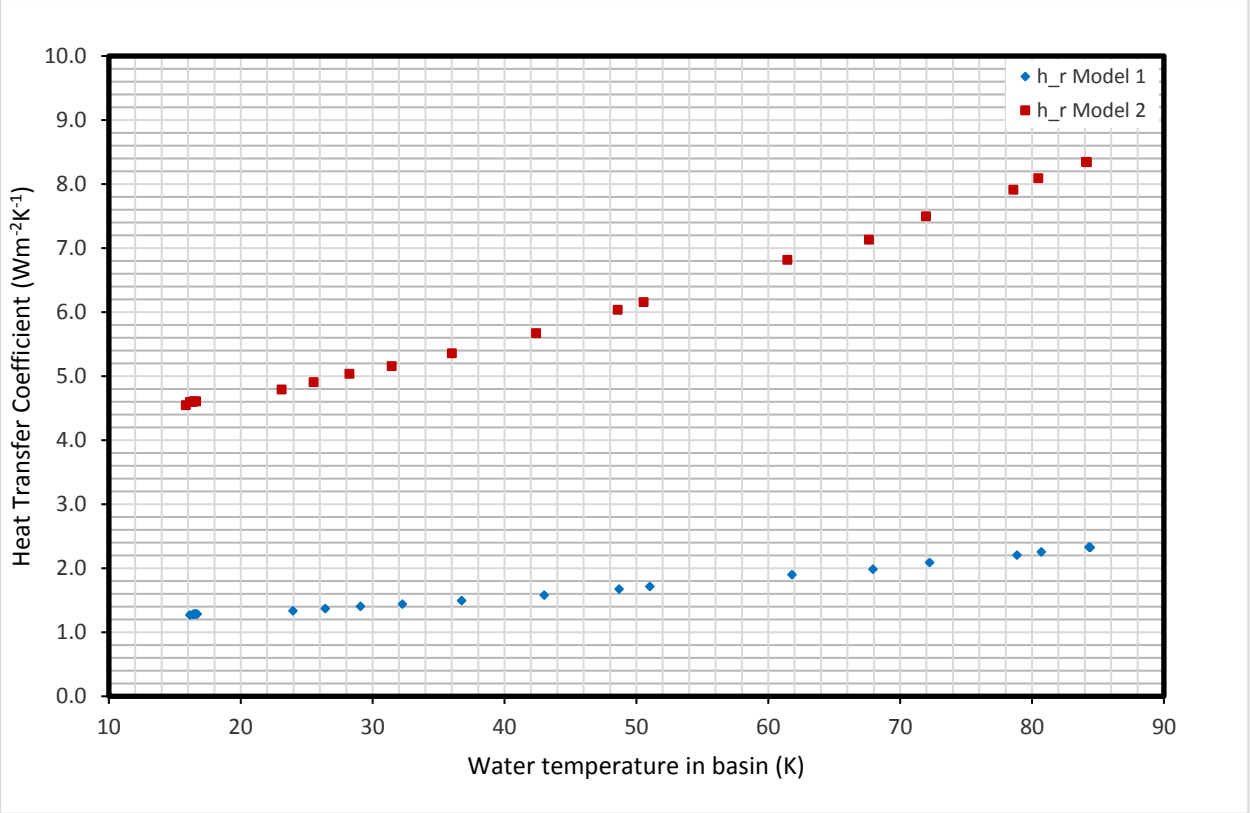

Figure 4.5: Radiative Heat Transfer Coefficients for Model 1 and Model 2 in solar still (summer: 1 January 2007)

The internal convective heat transfer coefficients are shown in Figure 4.6. This figure indicates that while Model 1 and Model 2 have similar heat transfer coefficients for all ranges of basin water temperature, the convective heat transfer coefficients of Model 1 are consistently higher. Lastly, the internal evaporative heat transfer coefficient is shown in Figure 4.7. This graph indicates that there is a sharp increase in the evaporative heat transfer coefficient with increased basin water temperatures. The assessed literature does not comment on the difference between evaporative and convective heat transfer coefficients between Model 1 and Model 2. However, the trend of these heat transfer coefficients, at least for Model 2, is consistent with literature (Tiwari & Tiwari, 2008). One study found that radiative heat transfer heat transfer coefficients dominate until 32°C, beyond which point the evaporate heat transfer coefficient begins to dominate (Tiwari & Tiwari, 2007a). A similar observation is made for this present study's heat transfer coefficients (for Model 2) (Tiwari & Tiwari, 2007b).

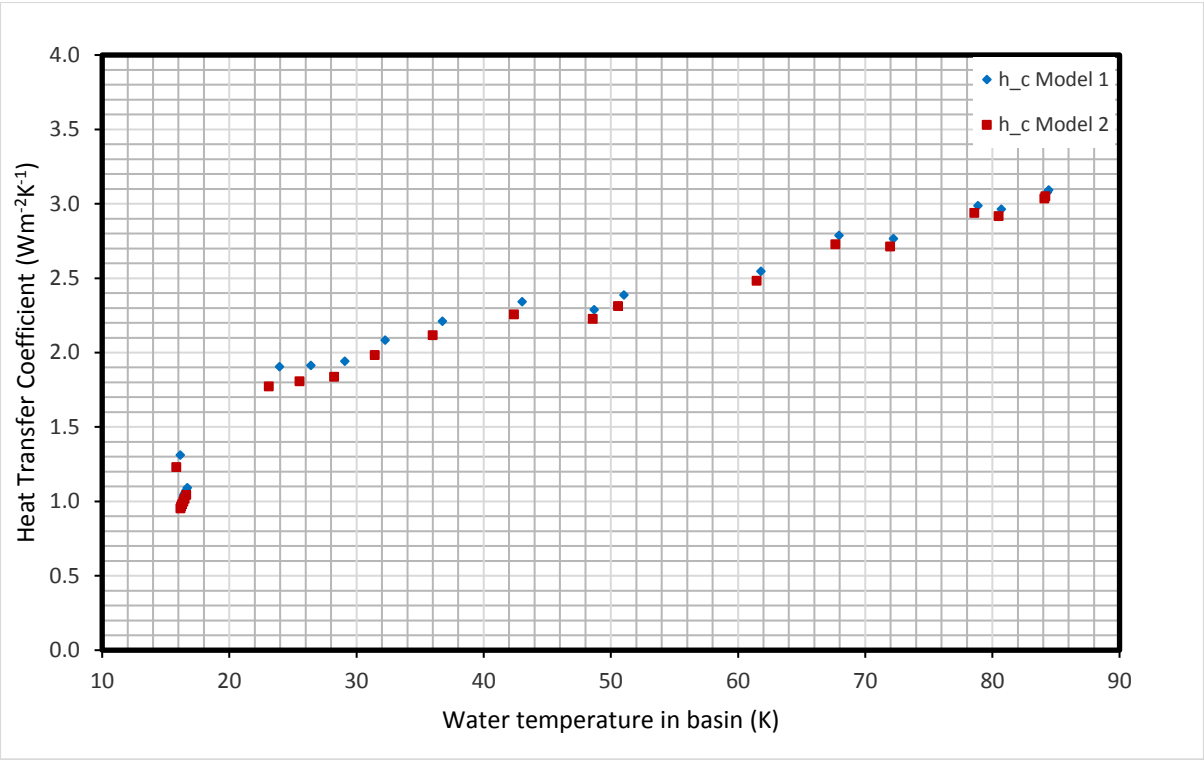

Figure 4.6: Convective Heat Transfer Coefficients for Model 1 and Model 2 in solar still (summer: 1 January 2007)

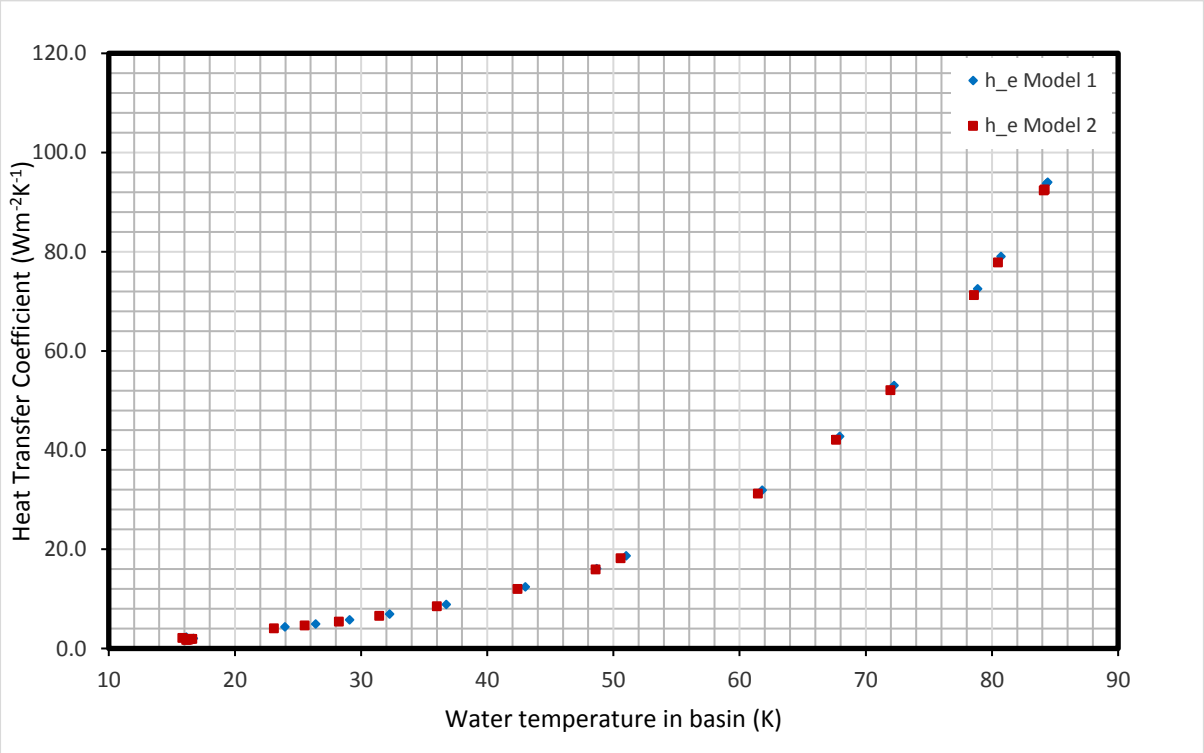

Figure 4.7: Evaporative Heat Transfer Coefficients for Model 1 and Model 2 in solar still (summer: 1 January 2007)

4.3.2 Monthly Performance

The monthly water yields are shown in Figure 4.8. As can be seen, the water yield peaks during summer months and falls off during winter months, with a water yield range of 151kgm^{-2} to 271kgm^{-2}. This can be attributed to a drop in radiation over the winter months which is said to be the most significant determining factor of still productivity (Nafey et al., 2000). In addition, wind speeds and ambient temperatures also affect still yields (Al-Hinai, Al-Nassri & Jubran, 2002), and these averages are also seasonally variant. These low water yields are related to the thermal efficiency (Figure 4.9), which is also shown to drop in winter months. The fluctuation of water yield with seasons is consistent with literature, which has reported a range of 30kgm^{-2} to 220kgm^{-2} (Kumar & Tiwari, 2009), with a design based on the same design specifications used in validation (Section 3.2.1). The differences in the range could be ascribed to different design parameters and climatic conditions.

The monthly electrical yields are also given in Figure 4.8. In this graph, it is seen that the electrical yield also falls off during the winter months and that a monthly energy production range of 13kWhm^{-2} to 18.2kWhm^{-2} exists. The low production rates over winter periods could also be attributed to low radiation levels over these periods (Duffie & Beckman, 2013). Despite the lower electrical energy yields over winter, there is an increase in electrical efficiency for this season, as shown Figure 4.9. This is likely due to lower winter ambient temperatures and radiation values result in less incident solar radiation on the panels (See Eq. (2.52)). Additionally, lower radiation levels mean lower water temperatures (less direct radiation on the basin and on the panel) and so a greater temperature difference between the water and the panels. This means that heat removal from the panels is better during the winter period than in the summer period (See Eq. (3.64)). The seasonal trend in electrical and water yields of the hybrid PV/T desalination is consistent with literature, which presents a monthly energy production range of 8.5 to 23.3kWhm^{-2} (Kumar & Tiwari, 2009). The discrepancies between this present study's monthly electrical energy production range and the range found in literature could, as with the differences in water yield outputs, be ascribed to different design parameters and climatic conditions.

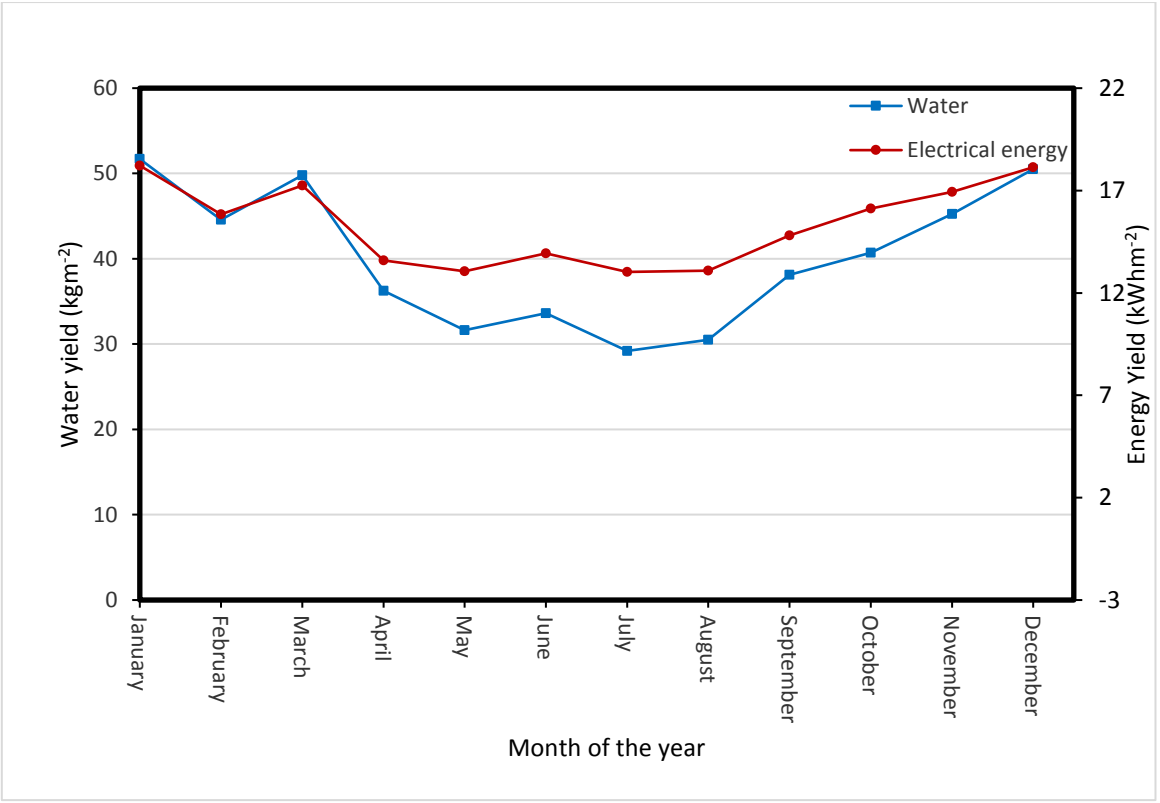

Figure 4.8: Monthly Water and Electrical Energy Yields (2007)

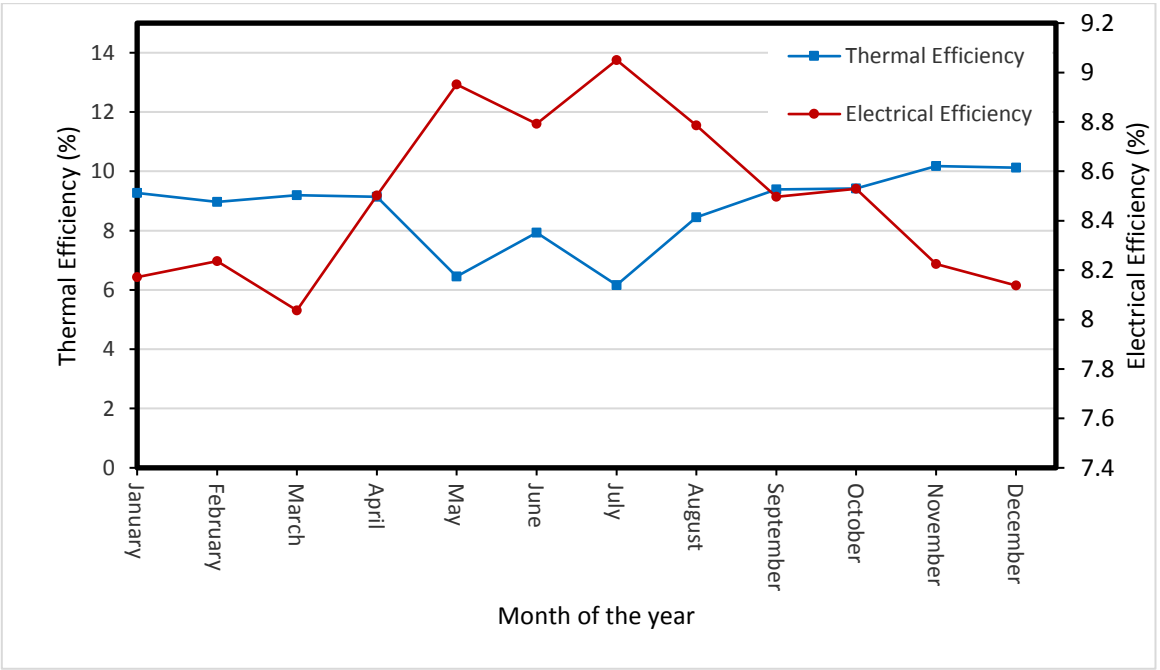

Figure 4.9: Monthly Average Thermal and Electrical efficiencies (2007)

4.4 Sensitivity Analyses

4.4.1 Water Depth

The water yields of the system for different water depths in the basin are shown in Figure 4.10. As can be seen in this graph, the water yields reduce with an increase in water depth, and so an optimal depth for water yield corresponds to 0.02m for the chosen parameter range. This drop in yield with depth increase can be explained by a similar drop in thermal efficiency, which is shown in Figure 4.11. The thermal efficiency drops because a greater water depth means a larger volume of water in the basin and thus a higher thermal capacitance. This larger thermal capacitance results in lower basin water temperatures (Chow, He & Ji, 2007) and these lower water temperatures imply a smaller temperature difference between the basin water's surface and the inner cover of the still. As such, lower evaporation rates, and so water yields, occur (Tiwari & Tiwari, 2008). The relationship between water depth and water yield output is confirmed in literature (Al-Hinai, Al-Nassri & Jubran, 2002; Kumar & Tiwari, 2008a). For illustrative purposes one solar still study found that a depth increase from 0.04m to 0.18m resulted in a yield decrease from 1.7 $kgday^{-1}$ to 1.3 $kgday^{-1}$ and a thermal efficiency decrease from 18.9% to 11.3% (Tiwari & Tiwari, 2006). In comparison, this present study's daily yield rates change from 8.4$kgday^{-1}$ to 6.9$kgday^{-1}$, and the thermal efficiencies vary from 18.4% to 15.4% for the same range of depth variations. These daily yields are quite different from each other as hybrid PV/T desalination systems are known to have higher yields. It should also be noted that the study was undertaken for summer months, while this present study calculates daily yield averages over the entire year (in different climatic conditions and locations). A study of an active hybrid system in Delhi indicated daily yields of about 4$kgday^{-1}$, 3$kgday^{-1}$ and 2.5$kgday^{-1}$ for the month of March (Spring) (Kumar & Tiwari, 2008a). These yields are lower than the yields of this present study, but these yield differences could be ascribed to different climatic conditions and design parameters.

The electrical yield (Figure 4.10) and efficiencies (Figure 4.11) on the other hand improve with greater water depth as cooler water in the basin implies cooler water in the tubes which improves the heat removal capabilities of the water (Chow, He & Ji, 2007). As a higher electrical energy yield is the primary concern for this thesis, a deeper water depth is thus more favourable (i.e. a 0.4m water depth is conducive to optimal efficiency). However, as the water

depth increases, there is a reduction in the extent to which electrical efficiency improves and in addition, the water yield decreases. As such, a weighting factor could be used to select an optimal depth depending on the preference for electrical energy yield over water yield. No literature was found quantifying the energy output of PV/T desalination systems with water depth variation.

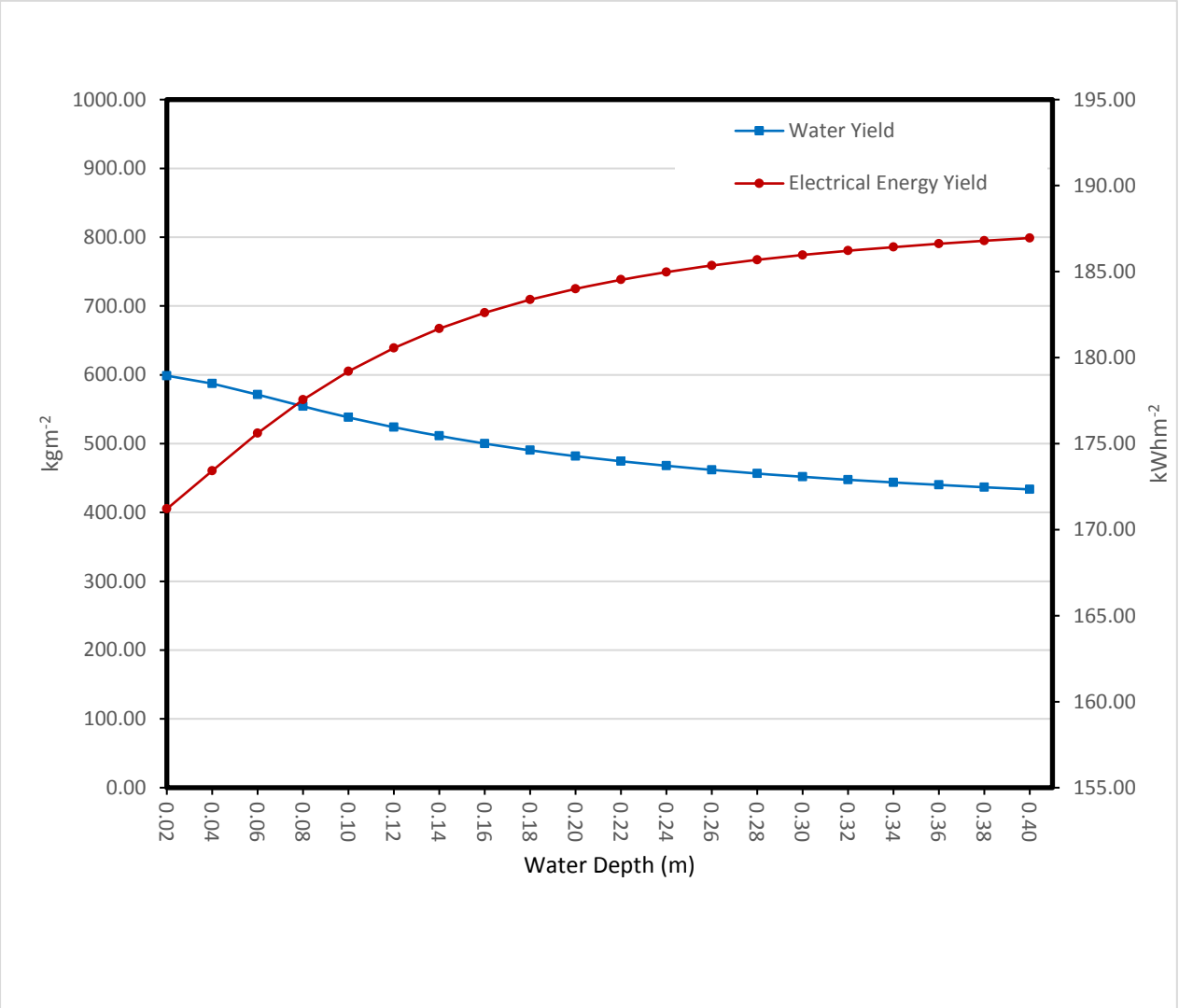

Figure 4.10: Annual Water and Electrical Energy Yields with Water Depth Variation (2007)

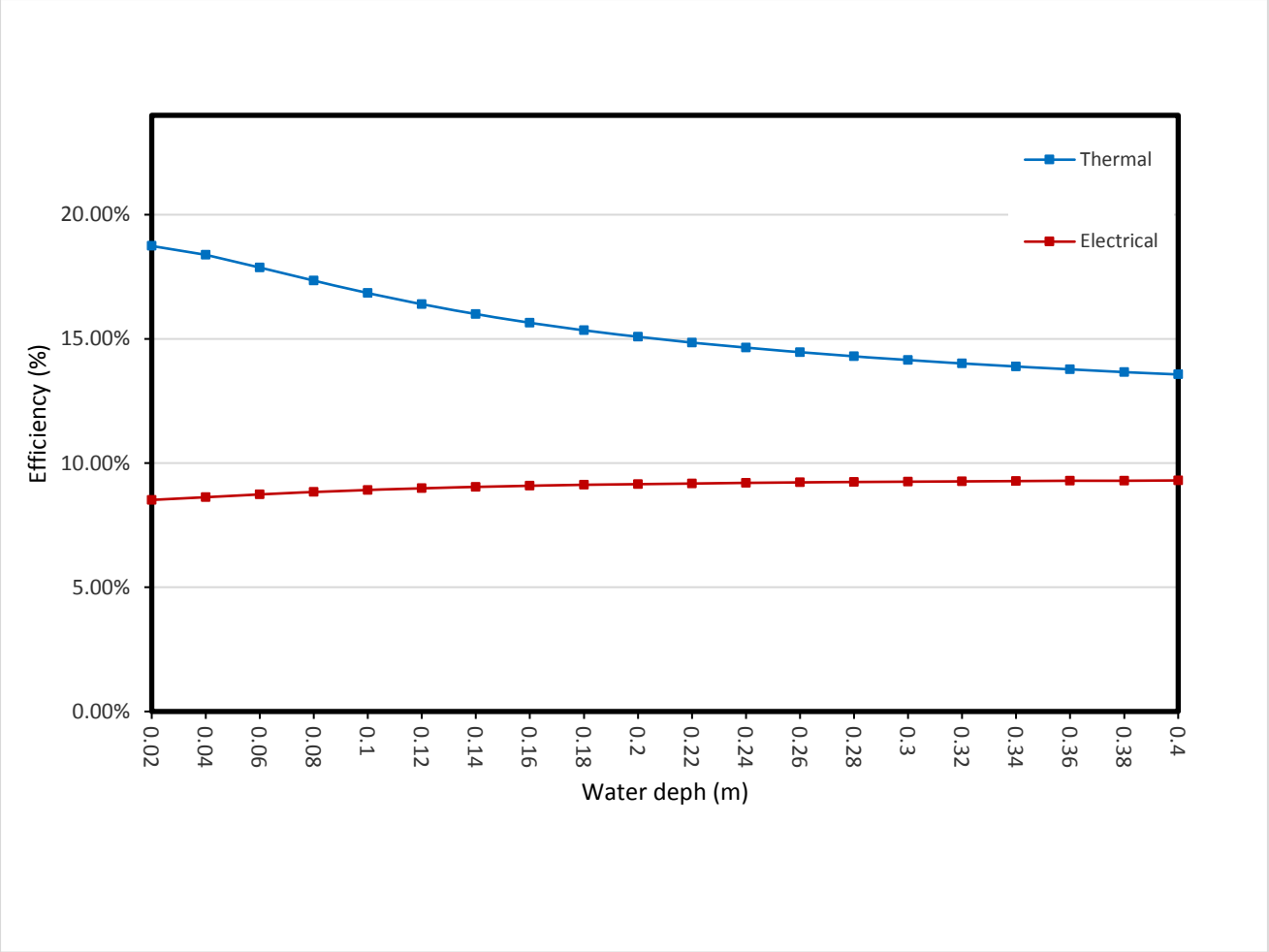

Figure 4.11: Thermal and electrical efficiencies with solar still depth variation (2007)

4.4.2 Panel Tilt Angle

Figure 4.12 shows how changing the tilt angle of a surface increases the available radiation on the surface over the course of a year. As can be seen from this figure, the optimal tilt angle for maximum radiation is 30º, which is close to the latitude of the location (approximately 34º south). As such, the results are consistent with literature (Khalifa, 2011; Duffie & Beckman, 2013).

Figure 4.13 illustrates how water and electrical energy yield varies as the panel tilt angle is altered. As can be seen in this figure, both the water and the electrical energy yields rise to an optimal point (30°), peak, and then decay. The slight deviation from the recommended average tilt angle could be ascribed to the fact that tilt angle should be optimally selected for specific

locations so as to account for the localised climatic conditions of that environment (cloudiness and altitude) (Yadav & Chandel, 2013). The same variation of available radiation with increased PV tilt angle also explains why both the thermal and electrical efficiencies rise to a maximum at 30º and fall thereafter as shown in Figure 4.14.

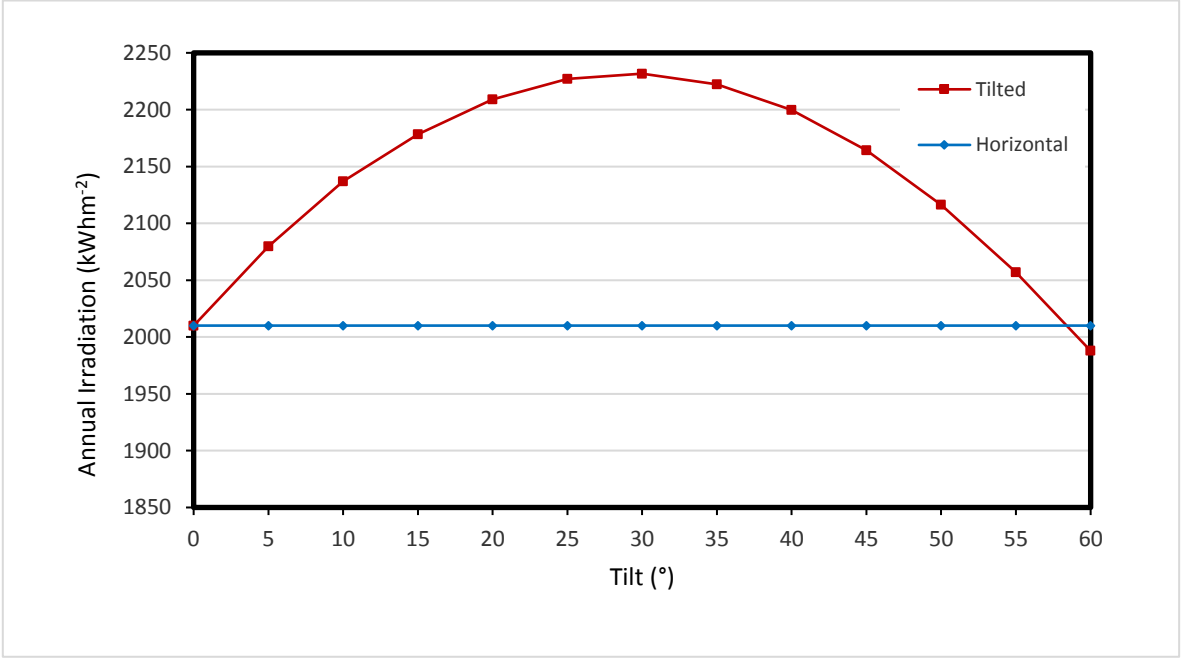

Figure 4.12: Tilted and Horizontal Annual Irradiation (2007)

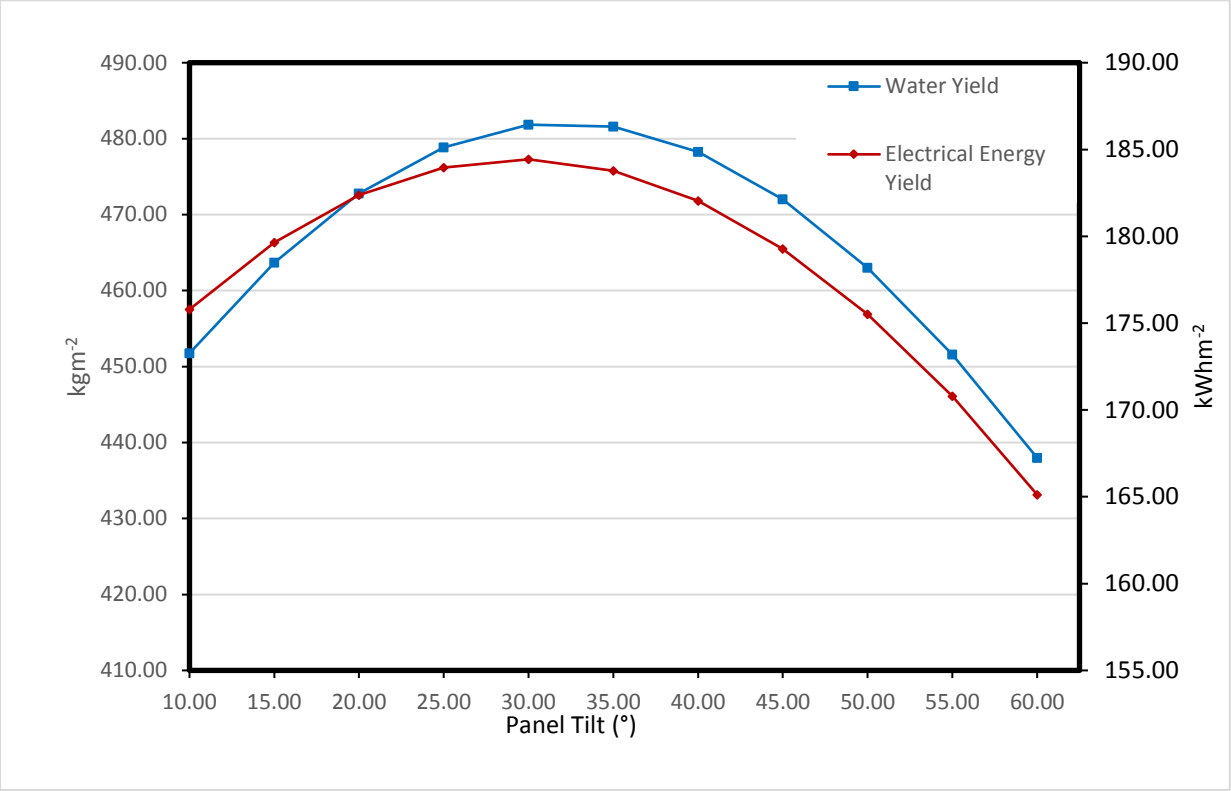

Figure 4.13: Water and energy yield with panel tilt angle variation (2007)

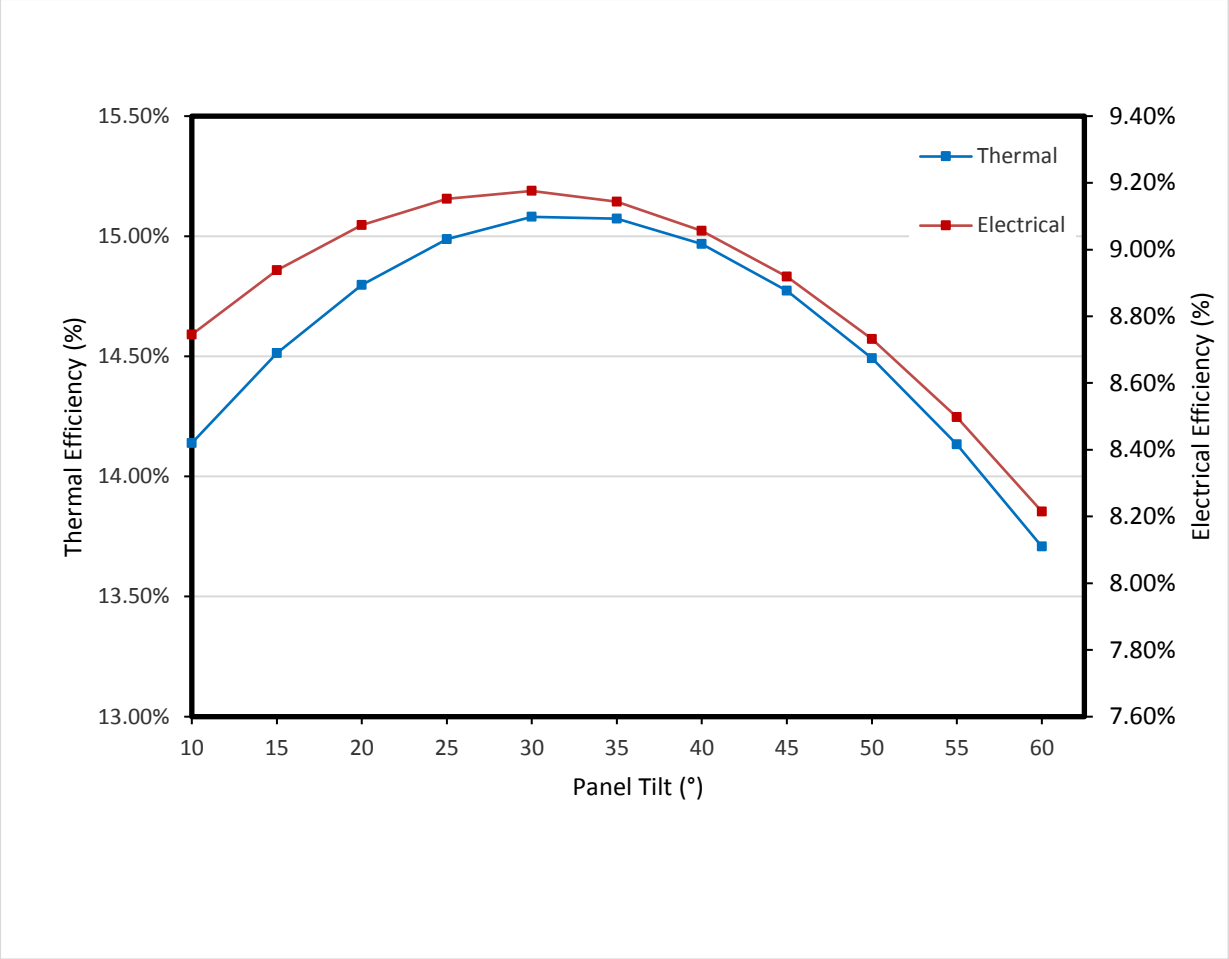

Figure 4.14: Thermal and electrical efficiencies with panel tilt angle variation (2007)

4.4.3 Solar Still Cover Tilt Angle

The water yields change with varying still cover tilt angle as shown in Figure 4.15. As can be seen in this figure, the water yield increases with increments in tilt angle, peaking at 40° but then decaying afterwards. Related to this, the efficiency curves are shown in Figure 4.16. These indicate how a steeper tilt angle raises the average thermal efficiency until a cover tilt angle of 40° is reached, and, thereafter the efficiency falls away. According to literature on solar stills, increasing the tilt angle beyond a certain optimal point decreases the water yield of the still . This reduction in yield can be ascribed, in part, to an increase in heat transfer area of the still cover and higher reflection losses that occur as the tilt angle is increased (Khalifa, 2011). According to literature, a higher tilt angle is favoured in winter seasons and lower a tilt angle in summer seasons (Nafey et al., 2000; Khalifa, 2011; Duffie & Beckman, 2013) while optimised annual yield can be achieved by setting the tilt angle to the latitude (Sampathkumar

et al., 2010). In light of this, the optimal tilt angle of 40° seems higher than the expected 34° (latitude) optimal tilt angle.

The electrical energy yield, unlike the water yield, initially drops off for small tilt angles (until 30º), and starts to rise thereafter. Similarly, the electrical efficiency drops until 30º and starts to improve for all steeper tilt angles. The electrical yield (Figure 4.15) and efficiency (Figure 4.16) initially drop with increments to the cover tilt angle because lower tilt angles mean higher water temperatures (as described above) and this limits the heat removal capabilities of the water (as discussed in Section 4.3.2). However, beyond about 30º, the yield and efficiency begin to rise because the non-optimal tilt angles allow less radiation into the still, and so the water does not get as warm. This increases the temperature differential between the water and the collector which means that more heat is removed from the collector and adjacent panels. As a result, higher electrical efficiencies are achieved at a steeper still covers tilt angle.

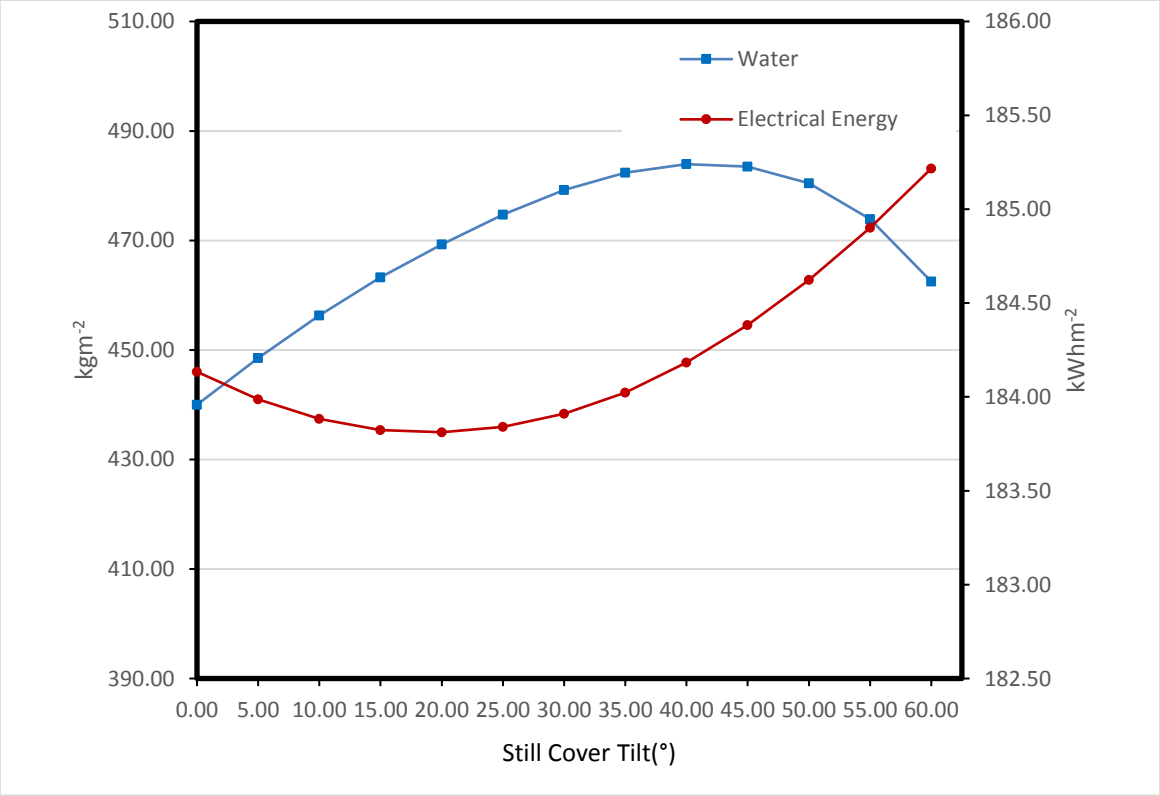

Figure 4.15: Water and energy yield with still cover tilt angle variation (2007)

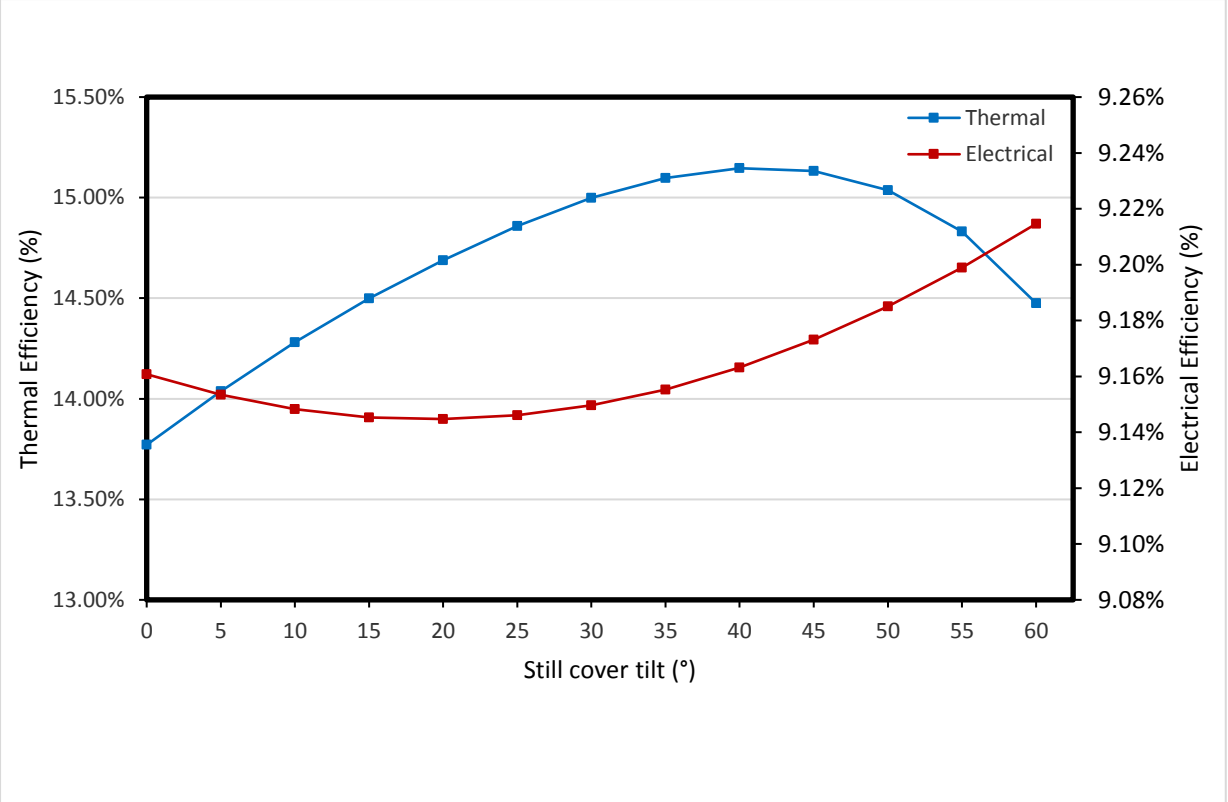

Figure 4.16: Thermal and electrical efficiencies for different still tilt angles (2007)

5 Conclusions and Recommendations

5.1 Introduction

Chapter 1 sought to illustrate how increasingly important photovoltaic generation and desalination are becoming. It was shown that PV systems help provide off-grid electricity access to unelectrified areas which affords people vital communication and education opportunities. Also, the close link between the global economy the availability of fossil fuel supplies was highlighted with reference to how vulnerable the economy is to future supply shortages and fuel price volatility. Furthermore, the link between the combustion of fossil fuels and climate change was discussed and the consequent importance of alternative energy sources - such as PV systems - was mentioned. Aside from access to energy, the lowering of aquifers, the salinisation of fresh water supplies and climate change were seen to be drivers of future water scarcity. In light of this, solar stills were presented as a simple technology that can help provide clean water access.

PV systems have low efficiencies as much of the incident radiation on the panels is lost as heat. In addition, solar stills have low water yields, but these yields can be improved by adding heat to them. As such, PV/T desalination systems were looked at as a way of utilising the waste heat from PV panels to enhance the daily water yields of solar stills. Numerical modelling was presented as a way of optimising the operational parameters of PV/T systems and solar stills. However, solar still models seldom account for the view factor in determining the radiative heat exchange within stills and no studies were felt which included the view factor in hybrid PV/T desalination systems. As such, the aim of this thesis was to construct a numerical model for a hybrid PV/T desalination system and determine its accuracy. To do this, the following objectives were defined: 1) Design a hybrid PV/T desalination system, 2) Create a mathematical model for the system 3) Validate the model against experimental data and 4) Run sensitivity analyses with the model.

The model was implemented using numerical methods in Matlab, and results from simulations are presented in Chapter 4. This section presents conclusions from those results and recommendations for future work.

5.2 Conclusions

5.2.1 Model Performance

The model was seen to predict experimental hourly water yields adequately. To illustrate, the view factor model (Model 1) was seen to have an RMSE value of 22.0%, while the no-view-factor model (Model 2), was seen to have an RMSE value of 28.9%. In addition, the correlation value between the outputs of the experiment and Model 1 was higher (0.9896) than the correlation value between the outputs of the experiment and Model 2 (0.9890). From this, it can be concluded that the model used in this thesis is valid and, furthermore, that the inclusion of a view factor improves the accuracy of hybrid PV/T desalination models.

5.2.2 Effect of Depth of Water on Distillate and Electrical Energy Yields

Water yields were seen to be higher with lower water depths than with higher water depths. This is because low water depths result in high basin water temperatures and consequently, a higher temperature differential between the still cover and basin water. As a result, the highest annual water yield was seen to be 598.77kgm^{-2}, which occurred at an optimal depth of 0.02m.

Conversely, higher water depths were seen to increase the electrical energy yield of the system as they result in cooler basin water temperatures. This cooler water removes heat from the panels more efficiently and so improves the electrical efficiency of the panels. As such, the highest annual electrical energy yield was seen to be 186.95 kWhm^{-2}, which occurred at an optimal depth of 0.4m.

It is therefore concluded that, for a hybrid PV/T desalination system, low water depths are better when water yield is a priority and high water depths when electrical energy yield is a priority.

5.2.3 *Effect of PV Panel Tilt Angle on Water and Electrical Energy Yields*

As the panel tilt angle increased, the annual water yield was seen to peak and then decline. This occurred because there is an optimal tilt angle for the site which maximises received radiation over the course of the year. The maximum annual water yield was seen to be 481.84 kgm^{-2} at an optimal panel tilt angle of 30°.

The same trend was found for electrical energy yield. A maximum annual yield of 184.44 $kWhm^{-2}$ was found which also occurred a panel tilt angle of 30°.

As such, it can be concluded that a hybrid PV/T desalination system located around 34° Latitude, can maximise outputs on an annual basis by setting the panel tilt angle to 30°.

5.2.4 *Effect of Solar Still Cover Tilt Angle on Water and Electrical Energy Yields*

As the solar still cover tilt angle was increased, the annual water yield rose to a peak point and subsequently declined. The decline in yield beyond the peak point could be ascribed to an increased surface area in solar still and higher reflection losses which occur at steeper cover tilt angles. As a result, the maximum annual water yield was seen to be 483.94kgm^{-2} which occurred at an optimal tilt angle of 40°.

With regard to the electrical yield, increasing solar still cover tilt angle initially decreased the annual electrical yield, and thereafter, the electrical yield began to rise again. This could be ascribed to the fact that initial increments in cover tilt angle optimised the received radiation in the basin and so increased the water temperature which in turn inhibited the ability of the water to remove heat from the panels. After the initial electrical energy drop, radiation input into the still became less optimal and so the annual electrical energy yield increased because water was able to remove heat from the panels in a more efficiently (it was cooler). As such, a maximum electrical energy yield of 185.22 $kWhm^{-2}$ occurred at a tilt angle of 60° (the upper limit of the cover tilt angle sensitivity range).

It can, therefore, be concluded that a hybrid PV/T desalination systems located around 34° can maximise its water yield if the cover tilt angle is set to 40°. Furthermore, for maximum electrical energy yield, the cover should be as steep as possible.

5.3 Recommendations

5.3.1 Construct an Experimental System

This thesis relied on experimental data from another study, and as such, not all pertinent meteorological data and parameters were present for validation purposes. For example, wind direction would have been useful in determining the convective heat transfer coefficients for the system more accurately. Furthermore, parameters such as the thermal conductivity of the absorber tube weld and the water flow rate had to be estimated from literature. In addition, relying on experimental data from a previous study meant that the quality of the data could not be assured (i.e. how well was the chamber sealed to prevent vapour leakage, etc.) Lastly, literature indicates that if electrical energy yield is a priority for a PV/T system, panels should cover collector plates entirely (Dubey & Tiwari, 2008). However, experimental data for such a configuration could not be found, and so a partially covered system was designed. In light of these shortfalls, an experimental configuration would help ensure that all relevant data is measured, system parameters are known, quality measures are in place and that the system is designed according to the needs of the model.

5.3.2 Improve the Model Accuracy by Accounting for the Solar Fraction

The model could be extended to incorporate the concept of Solar Fraction (See Section 3.4.2.3). This type of model accounts for reflection off of the walls on the solar still and is said to improve the accuracy of solar still models (Tiwari & Tiwari, 2007b).

6 References

Abdulkadir, M., Samosir, A.S. & Yatim, A. 2012. Modeling and simulation based approach of photovoltaic system in simulink model. *ARPN Journal of Engineering and Applied Sciences.* 7(5):616-623.

Acciani, G., Falcone, O. & Vergura, S. 2010. Analysis of the thermal heating of poly-Si and a-Si photovoltaic cell by means of FEM. *Cell.* 4:4.

Al-Hinai, H., Al-Nassri, M. & Jubran, B. 2002. Effect of climatic, design and operational parameters on the yield of a simple solar still. *Energy Conversion and Management.* 43(13):1639-1650.

Armstrong, S. & Hurley, W.G. 2010. A thermal model for photovoltaic panels under varying atmospheric conditions. *Applied Thermal Engineering.* 30(11–12):1488-1495. DOI:http://dx.doi.org.ezproxy.uct.ac.za/10.1016/j.applthermaleng.2010.03.012.

Bakelli, Y., Arab, A.H. & Azoui, B. 2011. Optimal sizing of photovoltaic pumping system with water tank storage using LPSP concept. *Solar Energy.* 85(2):288-294.

Baldwin, D.S., Rees, G.N., Mitchell, A.M., Watson, G. & Williams, J. 2006. The short-term effects of salinization on anaerobic nutrient cycling and microbial community structure in sediment from a freshwater wetland. *Wetlands.* 26(2):455-464.

Benghanem, M. 2011. Optimization of tilt angle for solar panel: Case study for Madinah, Saudi Arabia. *Applied Energy.* 88(4):1427-1433.

Bergene, T. & Løvvik, O.M. 1995. Model calculations on a flat-plate solar heat collector with integrated solar cells. *Solar Energy.* 55(6):453-462.

Bergman, T.L., Incropera, F.P. & Lavine, A.S. 2011. *Fundamentals of heat and mass transfer.* 7th Edition ed. U.S.: John Wiley & Sons.

Botzen, W.J.W., Gowdy, J.M. & van den Bergh, C.J.M. 2008. Cumulative CO2 emissions: shifting international responsibilities for climate debt. *Climate Policy.* 8(6):569-576.

Callister, W.D. & Rethwisch, D.G. 2007. *Materials science and engineering: an introduction.* Seventh Edition ed. Utah: Wiley New York.

Cengel, Y.A. 1997. *Introduction to thermodynamics and heat transfer.* New York: McGraw-Hill.

Chaâbane, M., Masmoudi, M. & Medhioub, K. 2004. Determination of Linke turbidity factor from solar radiation measurement in northern Tunisia. *Renewable Energy.* 29(13):2065-2076.

Chapra, S.C. & Canale, R.P. 2012. *Numerical methods for engineers.* Sixth edition ed. McGraw-Hill.

Charalambous, P., Maidment, G., Kalogirou, S. & Yiakoumetti, K. 2007. Photovoltaic thermal (PV/T) collectors: A review. *Applied Thermal Engineering.* 27(2):275-286.

Chow, T.T. 2010. A review on photovoltaic/thermal hybrid solar technology. *Applied Energy.* 87(2):365-379.

Chow, T. 1997. Chilled water cooling coil models from empirical to fundamental. *Numerical Heat Transfer, Part A Applications.* 32(1):63-83.

Chow, T. 2003. Performance analysis of photovoltaic-thermal collector by explicit dynamic model. *Solar Energy.* 75(2):143-152.

Chow, T., He, W. & Ji, J. 2006. Hybrid photovoltaic-thermosyphon water heating system for residential application. *Solar Energy.* 80(3):298-306.

Chow, T.T., He, W. & Ji, J. 2007. An experimental study of façade-integrated photovoltaic/water-heating system. *Applied Thermal Engineering.* 27(1):37-45. DOI:http://dx.doi.org.ezproxy.uct.ac.za/10.1016/j.applthermaleng.2006.05.015.

Chukwuka, C.O. 2013. A study of the solar energy systems and storage devices. University of Cape Town.

Da Rosa, A.V. 2009. *Fundamentals of renewable energy processes.* Second Edition ed. USA: Academic Press.

Da Silva, R. & Fernandes, J. 2010. Hybrid photovoltaic/thermal (PV/T) solar systems simulation with SIMULINK/MATLAB. *Solar Energy.* 84(12):1985-1996.

Davis, S.J., Caldeira, K. & Matthews, H.D. 2010. Future CO2 emissions and climate change from existing energy infrastructure. *Science (New York, N.Y.).* 329(5997):1330-1333. DOI:10.1126/science.1188566 [doi].

Dawoud, M.A. 2005. The role of desalination in augmentation of water supply in GCC countries. *Desalination.* 186(1–3):187-198. DOI:http://dx.doi.org/10.1016/j.desal.2005.03.094.

Deniz, E. 2012. An Experimental and Theoretical Analysis of a Vacuum Tube Solar Collector-assisted Solar Distillation System. *Energy Sources, Part A: Recovery, Utilization, and Environmental Effects.* 34(17):1637-1645.

Dev, R. & Tiwari, G. 2010. Characteristic equation of a hybrid (PV-T) active solar still. *Desalination.* 254(1):126-137.

Diabate, L., Remund, J. & Wald, L. 2003. Linke turbidity factors for several sites in Africa. *Solar Energy.* 75(2):111-119.

Dobrzański, L. & Drygała, A. 2008. Surface texturing of multicrystalline silicon solar cells. *Journal of Achievements in Materials and Manufacturing Engineering.* 31(1):77-82.

Dowdy, S., Wearden, S. & Chilko, D. 2004. *Statistics for research.* Third Edition ed. USA: John Wiley & Sons.

Dubey, S. & Tiwari, G. 2008. Thermal modeling of a combined system of photovoltaic thermal (PV/T) solar water heater. *Solar Energy.* 82(7):602-612.

Duffie, J.A. & Beckman, W.A. 2013. *Solar Engineering of Thermal Processes.* 4th Edition ed. University of Wisconsin-Madison, Solar Energy Laboratory, Madison, WI: John Wiley & Sons, Inc.

El-Maghlany, W.M., El-Samadony, Y. & Kabeel, A. 2015. Glass cover inclination angle effect on the radiation shape factor within conventional solar still. *Desalination and Water Treatment.* :1-9.

El-Sebaii, A. 1998. Parametric study of a vertical solar still. *Energy Conversion and Management.* 39(13):1303-1315.

Erdil, E., Ilkan, M. & Egelioglu, F. 2008. An experimental study on energy generation with a photovoltaic (PV)–solar thermal hybrid system. *Energy.* 33(8):1241-1245.

Europe Solar Production n.d. *ESP 6M 240-255 Wp Polycrystalline Photovoltaic Module Premium Quality Solar Module Data sheet.* Available: http://www.europe-solarproduction.com/media/400/ESP-Polycrystalline-Solar-Module-Datasheet-ESP-6P-series_4mm.pdf [2015 October 11].

Falk, A., Durschner, C. & Remmers, K. 2007. *Photovoltaics for professionals: solar electric systems marketing, design and installation.* Berlin: Routledge.

Fischer, G., Tubiello, F.N., van Velthuizen, H. & Wiberg, D.A. 2007. Climate change impacts on irrigation water requirements: Effects of mitigation, 1990–2080. *Technological Forecasting and Social Change.* 74(7):1083-1107. DOI:http://dx.doi.org/10.1016/j.techfore.2006.05.021.

Fofonoff, N.P. & Millard, R. 1991. Calculation of physical properties of seawater. *WOCE Operations Manual, T.Joyce, Editor, WOCE Hydrographic Programme Offce, WHPO.* :91-91.

Fraisse, G., Ménézo, C. & Johannes, K. 2007. Energy performance of water hybrid PV/T collectors applied to combisystems of Direct Solar Floor type. *Solar Energy.* 81(11):1426-1438.

Friction Losses in Pipe Fittings. 2015. Available: http://www.metropumps.com/ResourcesFrictionLossData.pdf [2015, May 18].

Furkan, D. & Mehmet Emin, M. 2010. Critical factors that affecting efficiency of solar cells. *Smart Grid and Renewable Energy.* 2010:47.

Guide to Glass Reinforced Plastic (GRP). 2015. Available: https://www.ecfibreglasssupplies.co.uk/t-GlassReinforcedPlastics.aspx [2016, January 8].

Halliday, D., Resnick, R. & Walker, J. 1997. *Fundementals of physics.* 5th edition ed. Canada: John Wiley & Sons, Inc.

Hamrouni, N., Jraidi, M. & Chérif, A. 2009. Theoretical and experimental analysis of the behaviour of a photovoltaic pumping system. *Solar Energy.* 83(8):1335-1344.

Hasan, M.A. & Sumathy, K. 2010. Photovoltaic thermal module concepts and their performance analysis: A review. *Renewable and Sustainable Energy Reviews.* 14(7):1845-1859.

He, W., Chow, T., Ji, J., Lu, J., Pei, G. & Chan, L. 2006. Hybrid photovoltaic and thermal solar-collector designed for natural circulation of water. *Applied Energy.* 83(3):199-210.

Hersch, P. & Zweibel, K. 1982. *Basic photovoltaic principles and methods.* No. SERI/SP-290-1448 ed. Golden, CO (USA): Solar Energy Research Inst.

Holman, J.P. 2010. *Heat Transfer.* 10th ed. New York: McGraw-Hill.

Höök, M., Hirsch, R. & Aleklett, K. 2009. Giant oil field decline rates and their influence on world oil production. *Energy Policy.* 37(6):2262-2272. DOI:http://dx.doi.org/10.1016/j.enpol.2009.02.020.

Houcque, D. 2005. *Introduction to MATLAB for Engineering Students.* Northwestern University.

Houser, T. 2010. Copenhagen, the accord, and the way forward. *Peterson Institute for International Economics.* P B 1 0 - 5.

Huang, B., Lin, T., Hung, W. & Sun, F. 2001. Performance evaluation of solar photovoltaic/thermal systems. *Solar Energy.* 70(5):443-448.

Hummel, R.E. 2011. *Electronic properties of materials.* Third Edition ed. New York: Springer Science & Business Media.

Incropera, F. & DeWitt, P. 2002. *Introduction to heat transfer.* 4th ed. New York: John Wiley & Sons.

International Energy Agency (IEA) 2011a. *Energy for all: financing access for the poor, Special early excerpt of the World Energy Outlook 2011.* Paris: IEA.

International Energy Agency (IEA) 2011b. *Renewable Energy technologies: Solar Energy Perspectives.* Paris: IEA.

International Energy Agency (IEA) 2014. *World energy outlook 2014 executive summary.* France: International Energy Association.

IPCC 2011. *Special Report on Renewable Energy Sources and Climate Change Mitigation.* United Kingdom and New York, NY, USA: Cambridge University Press.

Jafar, M. 2000. A model for small-scale photovoltaic solar water pumping. *Renewable Energy.* 19(1):85-90.

Jones, A. & Underwood, C. 2001. A thermal model for photovoltaic systems. *Solar Energy.* 70(4):349-359.

Kacira, M., Simsek, M., Babur, Y. & Demirkol, S. 2004. Determining optimum tilt angles and orientations of photovoltaic panels in Sanliurfa, Turkey. *Renewable Energy.* 29(8):1265-1275. DOI:http://dx.doi.org.ezproxy.uct.ac.za/10.1016/j.renene.2003.12.014.

Kalogirou, S.A. 2001. Use of TRNSYS for modelling and simulation of a hybrid pv–thermal solar system for Cyprus. *Renewable Energy.* 23(2):247-260.

Kalogirou, S.A. & Tripanagnostopoulos, Y. 2006. Hybrid PV/T solar systems for domestic hot water and electricity production. *Energy Conversion and Management.* 47(18):3368-3382.

Kanagawa, M. & Nakata, T. 2008. Assessment of access to electricity and the socio-economic impacts in rural areas of developing countries. *Energy Policy.* 36(6):2016-2029.

Karekezi, S., McDade, S., Boardman, B., Kimani, J. & Lustig, L. 2012. *Chapter 2: Energy, Poverty and Development.* United States: Cambridge University Press.

Key Features. 2016. Available: http://www.mathworks.com/products/matlab/features.html#key_features [2016, January 3].

Khalifa, A.J.N. 2011. On the effect of cover tilt angle of the simple solar still on its productivity in different seasons and latitudes. *Energy Conversion and Management.* 52(1):431-436.

Khawaji, A.D., Kutubkhanah, I.K. & Wie, J. 2008. Advances in seawater desalination technologies. *Desalination.* 221(1–3):47-69. DOI:http://dx.doi.org.ezproxy.uct.ac.za/10.1016/j.desal.2007.01.067.

Kitcher, C. 2012. *A Practical Guide to Renewable Energy: Microgeneration Systems and Their Installation.* Routledge.

Kumar, S. & Tiwari, A. 2008a. An experimental study of hybrid photovoltaic thermal (PV/T)-active solar still. *International Journal of Energy Research.* 32(9):847-858.

Kumar, S. & Tiwari, A. 2010. Design, fabrication and performance of a hybrid photovoltaic/thermal (PV/T) active solar still. *Energy Conversion and Management.* 51(6):1219-1229.

Kumar, S. & Tiwari, G. 2009. Life cycle cost analysis of single slope hybrid (PV/T) active solar still. *Applied Energy.* 86(10):1995-2004.

Kumar, S., Tiwari, G. & Gaur, M. 2010. Development of empirical relation to evaluate the heat transfer coefficients and fractional energy in basin type hybrid (PV/T) active solar still. *Desalination.* 250(1):214-221.

Kumar, S. & Tiwari, A. 2008b. An experimental study of hybrid photovoltaic thermal (PV/T)-active solar still. *International Journal of Energy Research.* 32(9):847-858. DOI:10.1002/er.1388.

Lienhard IV, J.H. & Lienhard V, J.H. 2008. *A heat transfer textbook.* Third Edition ed. Cambridge, Massachusetts, USA: Phlogiston Press.

Madhlopa, A. & Clarke, J. 2013. Computation of irradiance in a solar still by using a refined algorithm. *Renewable Energy.* 51:13-21.

Madhlopa, A. 2009. Development of an advanced passive solar still with separate condenser. Doctor of Philosophy in Mechanical Engineering. The University of Strathclyde.

Madhlopa, A. 2014. Modelling radiative heat transfer inside a basin type solar still. *Applied Thermal Engineering.* 73(1):707-711. DOI:http://dx.doi.org/10.1016/j.applthermaleng.2014.07.065.

Markvart, T. 2000. *Solar electricity.* 2nd ed. John Wiley & Sons.

Mathews, J.H. & Fink, K.D. 1999. *Numerical methods using MATLAB.* 3rd ed. Prentice hall Upper Saddle River, NJ.

Mathioulakis, E., Belessiotis, V. & Delyannis, E. 2007. Desalination by using alternative energy: Review and state-of-the-art. *Desalination.* 203(1–3):346-365. DOI:http://dx.doi.org/10.1016/j.desal.2006.03.531.

Mathur, J. & Mathur, S. 2006. Summer-performance of inclined roof solar chimney for natural ventilation. *Energy and Buildings.* 38(10):1156-1163.

McMahon, D. 2007. *MATLAB demystified.* McGraw-Hill.

Mehleri, E.D., Zervas, P.L., Sarimveis, H., Palyvos, J.A. & Markatos, N.C. 2010. Determination of the optimal tilt angle and orientation for solar photovoltaic arrays. *Renewable Energy.* 35(11):2468-2475. DOI:http://dx.doi.org.ezproxy.uct.ac.za/10.1016/j.renene.2010.03.006.

Messenger, R. & Venre, J. 2003. *Photovoltaic systems engineering.* 2nd ed. CRC press.

Meyers, H. & Myers, H. 1997. *Introductory solid state physics.* Second ed. Cornwall: CRC press.

Moradian, A. 2013. Performance Study of a Photovoltaic Thermal System. *Rramt.* 35.

Myers, D.R. 2013. *Solar radiation: practical modeling for renewable energy applications.* CRC Press.

Nafey, A.S., Abdelkader, M., Abdelmotalip, A. & Mabrouk, A.A. 2000. Parameters affecting solar still productivity. *Energy Conversion and Management.* 41(16):1797-1809. DOI:http://dx.doi.org.ezproxy.uct.ac.za/10.1016/S0196-8904(99)00188-0.

New License for MATLAB Home. 2016. Available: https://www.mathworks.com/store/link/products/home/new [2016, January 3].

Niang, I., Ruppel, O.C., Abdrabo, M.A., Essel, A., Lennard, C., Padgham, J. & Urquhart, P. 2014. Africa. In V.R. Barros, and others, Ed. Cambridge, United Kingdom and New York, NY, USA: Cambridge University Press. 1199-1265.

Notton, G., Motte, F., Cristofari, C. & Canaletti, J. 2014. Performances and numerical optimization of a novel thermal solar collector for residential building. *Renewable and Sustainable Energy Reviews.* 33:60-73.

Notton, G., Cristofari, C., Mattei, M. & Poggi, P. 2005. Modelling of a double-glass photovoltaic module using finite differences. *Applied Thermal Engineering.* 25(17–18):2854-2877. DOI:http://dx.doi.org/10.1016/j.applthermaleng.2005.02.008.

Odendaal, N. 2015, June 2. *Load-shedding a reality until 2023, says former Eskom adviser.* Available: http://www.engineeringnews.co.za/article/load-shedding-a-reality-until-2023-says-former-eskom-adviser-2015-06-02 [2016, January 26].

Palyvos, J.A. 2008. A survey of wind convection coefficient correlations for building envelope energy systems' modeling. *Applied Thermal Engineering.* 28(8–9):801-808. DOI:http://dx.doi.org/10.1016/j.applthermaleng.2007.12.005.

Papadopoulou, E. 2011. *Photovoltaic Industrial Systems: An Environmental Approach.* Berlin: Springer Science & Business Media.

Pegels, A. 2010. Renewable energy in South Africa: Potentials, barriers and options for support. *Energy Policy.* 38(9).

Preston-Thomas, H. 1990. The International Temperature Scale of 1990(ITS-90). *Metrologia.* 27(1):3-10.

Pricing Info. 2016. Available: http://www.trnsys.com/order/pricing.php [2016, January 3].

Sampathkumar, K., Arjunan, T., Eswaramoorthy, M. & Senthilkumar, P. 2013. Thermal Modeling of a Solar Still Coupled with Evacuated Tube Collector under Natural Circulation Mode—An

Experimental Validation. *Energy Sources, Part A: Recovery, Utilization, and Environmental Effects.* 35(15):1441-1455.

Sampathkumar, K., Arjunan, T.V., Pitchandi, P. & Senthilkumar, P. 2010. Active solar distillation—A detailed review. *Renewable and Sustainable Energy Reviews.* 14(6):1503-1526. DOI:http://dx.doi.org.ezproxy.uct.ac.za/10.1016/j.rser.2010.01.023.

Sandnes, B. & Rekstad, J. 2002. A photovoltaic/thermal (PV/T) collector with a polymer absorber plate. Experimental study and analytical model. *Solar Energy.* 72(1):63-73.

Serway, R.A. & Jewett, J.W. 2004. *Physics for Scientists and Engineers.* 6th edition ed. California: Thompson Brooks/Cole.

Sharqawy, M.H., Lienhard, J.H. & Zubair, S.M. 2010. Thermophysical properties of seawater: a review of existing correlations and data. *Desalination and Water Treatment.* 16(1-3):354-380.

Singh, G., Dwivedi, V., Yadav, J. & Tiwari, G. 2012. Experimental validation of thermal model of hybrid photovoltaic thermal (HPVT) double slope active solar still. *Desalination and Water Treatment.* 45(1-3):182-190.

Singh, H.N. & Tiwari, G.N. 2005. Evaluation of cloudiness/haziness factor for composite climate. *Energy.* 30(9):1589-1601. DOI:http://dx.doi.org/10.1016/j.energy.2004.04.036.

Skoplaki, E., Boudouvis, A. & Palyvos, J. 2008. A simple correlation for the operating temperature of photovoltaic modules of arbitrary mounting. *Solar Energy Materials and Solar Cells.* 92(11):1393-1402.

Skoplaki, E. & Palyvos, J.A. 2009. On the temperature dependence of photovoltaic module electrical performance: A review of efficiency/power correlations. *Solar Energy.* 83(5):614-624. DOI:http://dx.doi.org.ezproxy.uct.ac.za/10.1016/j.solener.2008.10.008.

Sorrell, S., Speirs, J., Bentley, R., Brandt, A. & Miller, R. 2009. *Global oil depletion-an assessment of the evidence for a near-term peak in global oil production.* UKERC.

Stiftung, H.B. 2007. *A Failure of leadership -How action on climate change will be overwhelmed by the energy crisis.* Global Witness.

Tait, L., Merven, B. & Senatla, M. 2013. *Investigating the current and future roles of paraffin in South Africa.* University of Cape Town.

Tilley, R.J. 2013. *Understanding solids: the science of materials.* Second Edition ed. Sussex: John Wiley & Sons.

Tina, G. & Abate, R.2008. Experimental verification of thermal behaviour of photovoltaic modules. *Electrotechnical Conference, 2008. MELECON 2008. the 14th IEEE Mediterranean.* IEEE. 579.

Tiwari, A.K. & Tiwari, G. 2007a. Annual performance analysis and thermal modelling of passive solar still for different inclinations of condensing cover. *International Journal of Energy Research.* 31(14):1358-1382.

Tiwari, A.K. & Tiwari, G. 2007b. Thermal modeling based on solar fraction and experimental study of the annual and seasonal performance of a single slope passive solar still: the effect of water depths. *Desalination.* 207(1):184-204.

Tiwari, G. & Tiwari, A.K. 2008. *Solar distillation practice for water desalination systems.* Anshan Pub.

Tiwari, A.K. & Tiwari, G.N. 2006. Effect of water depths on heat and mass transfer in a passive solar still: in summer climatic condition. *Desalination.* 195(1):78-94.

Tripanagnostopoulos, Y., Nousia, T., Souliotis, M. & Yianoulis, P. 2002. Hybrid photovoltaic/thermal solar systems. *Solar Energy.* 72(3):217-234.

Tripathi, R. & Tiwari, G. 2004. Performance evaluation of a solar still by using the concept of solar fractionation. *Desalination.* 169(1):69-80.

TRNSYS. Available: http://energy-models.com/software/trnsys [2016, January 2].

van Helden, W.G.J., van Zolingen, R.J.C. & Zondag, H.A. 2004. PV thermal systems: PV panels supplying renewable electricity and heat. *Progress in Photovoltaics: Research and Applications.* 12(6):415-426.

What is TRNSYS? 2016. Available: http://www.trnsys.com/ [2016, 3 January].

Welty, J.R., Wicks, C.E., Rorrer, G. & Wilson, R.E. 2007. *Fundamentals of momentum, heat, and mass transfer.* 5th edition ed. John Wiley & Sons.

Willmott, C.J. & Matsuura, K. 2005. Advantages of the mean absolute error (MAE) over the root mean square error (RMSE) in assessing average model performance. *Climate Research.* 30(1):79.

Yadav, A.K. & Chandel, S.S. 2013. Tilt angle optimization to maximize incident solar radiation: A review. *Renewable and Sustainable Energy Reviews.* 23:503-513. DOI:http://dx.doi.org/10.1016/j.rser.2013.02.027.

Yergin, D. 2006. Ensuring energy security. *Foreign Affairs.* :69-82.

Yunus, A.C. 2003. *Heat transfer: a practical approach.* 2nd Edition ed. McGraw - Hil.

Zakharchenko, R., Licea-Jiménez, L., Pérez-Garcıa, S., Vorobiev, P., Dehesa-Carrasco, U., Pérez-Robles, J., Gonzalez-Hernández, J. & Vorobiev, Y. 2004. Photovoltaic solar panel for a hybrid PV/thermal system. *Solar Energy Materials and Solar Cells.* 82(1):253-261.

Zondag, H. 2008. Flat-plate PV-Thermal collectors and systems: A review. *Renewable and Sustainable Energy Reviews.* 12(4):891-959.

Zondag, H., De Vries, D.D., Van Helden, W., Van Zolingen, R. & Van Steenhoven, A. 2002. The thermal and electrical yield of a PV-thermal collector. *Solar Energy.* 72(2):113-128.

Zondag, H.A., de Vries, D.W., van Helden, W.G.J., van Zolingen, R.J.C. & van Steenhoven, A.A. 2003. The yield of different combined PV-thermal collector designs. *Solar Energy.* 74(3):253-269. DOI:http://dx.doi.org.ezproxy.uct.ac.za/10.1016/S0038-092X(03)00121-X.

7 Appendices

7.1 Appendix A: Heat Transfer

There are three principal mechanisms by which heat transfer occurs. These are namely, conduction, convection and radiation. All of these are pertinent to thermal modelling and are so discussed in this section.

Conductive heat transfer occurs when a temperature gradient exists within a material. When such a condition is met, heat flows from a region of high temperature (T_{hot}) to a region of low temperature (T_{cold}) in proportion to the heat transfer coefficient of the material and area perpendicular to heat transit. Additionally, the rate of heat transfer is inversely proportional to the thickness of the material (δ) traversed (Holman, 2010). This relationship is termed Fourier's Law and is shown by Eq. (7.1)(Incropera & DeWitt, 2002). This equation can be written in terms of the heat transfer coefficient as shown by Eq. (7.2). The heat transfer coefficient being given in Eq. (7.3)(Incropera & DeWitt, 2002).

$$q = \frac{k}{\delta} A_{sur}(T_{hot} - T_{cold}) \tag{7.1}$$

$$q = hA_{sur}\Delta T \tag{7.2}$$

$$h = \frac{k}{\delta} \tag{7.3}$$

The second mechanism for heat transfer is convection. Convection is a mechanism of heat transfer that occurs between a solid surface region and moving liquids or gases that come into contact with the surface (Yunus, 2003). Convection is contingent on two mechanisms for heat transfer. The first is diffusion. Diffusion heat transfer results from random molecular motion and an aggregated energy transfer between molecules. The second form of heat transfer results from macroscopic motion within the fluid (Incropera & DeWitt, 2002). The equation that governs convection is termed, Newton's Law of Cooling and it is shown by Eq. (7.4)(Holman, 2010). Heat gain in a fluid can either be termed sensible or latent heat. Sensible heat refers to

heat that results in a temperature change in a fluid and is related to the kinetic energy of molecules. Latent heat refers to heat that contributes to a phase change of a substance (Yunus, 2003).

$$q = hA_{sur}(T_{sur} - T_s) \tag{7.4}$$

Convection can be forced or natural. With natural convection, hot fluids rise and cool fluids sink to replace the fluid and so natural circulation takes place. Forced convection is different in that, in addition to natural convection, fluid movement is induced by another mechanism (such as by a fan or a pump) (Incropera & DeWitt, 2002).

Radiative heat transfer is the final form of energy transfer. Radiative heat transfer occurs for all bodies with any temperature above absolute 0° K and requires no transfer medium (Incropera & DeWitt, 2002). The heat transfer is happens according to Stefan-Boltzmann's equation as shown in Eq. (7.5)(Yunus, 2003). This equation depends on the temperature differential between the surface and its surroundings and is directly proportional to the area of the surface. Additionally, two other terms need to be defined. Stephan Boltzmann's constant (σ) and the emissivity of the surface (ε). The constant is given in the nomenclature section of this study, while the emissivity of the surface indicates how similarly the surface emits heat compared to a blackbody (perfect emitter with an emissivity of 1) (Yunus, 2003). Eq. (7.5) can also be written in terms of the heat transfer coefficient. To do this, the heat transfer coefficient is written as a function of the temperature of surface and sky temperature (T_s) as shown by Eq. (7.6)(Incropera & DeWitt, 2002). Kumar & Tiwari (2008a) presents formulas for approximating the sky temperature (T_s) to the ambient temperature (T_a). This formula is presented in Eq. (7.7).

$$q = \varepsilon\sigma A_{sur}({T_{sur}}^4 - {T_s}^4) \tag{7.5}$$

$$h_r = \varepsilon\sigma(T_{sur} + T_s)({T_{sur}}^2 + {T_s}^2) \tag{7.6}$$

$$T_s = 0.0552{T_a}^{1.5} \tag{7.7}$$

An analogous comparison between electrical and thermal resistance can be made. This conversion is given by Eq. (7.8) (Incropera & DeWitt, 2002). This equation represents the conductive heat transfer coefficient (h) which is shown in Eq. (7.9).

$$R = \frac{\delta}{kA_{sur}} \tag{7.8}$$

$$h = \frac{1}{RA_{sur}} \tag{7.9}$$

7.2 Appendix B: Types of Solar Cells

Three main types of solar cell types exist. These are namely: multi-crystalline silicon cells, monocrystalline silicon cells and thin film silicon cells (Falk, Durschner & Remmers, 2007). Monocrystalline cells are common and, together with polycrystalline type cells, account for about 93% of the solar cell market share. The remaining share belongs to thin film modules which are comprised of amorphous silicon ($\alpha - Si$ at a 4.2 share), copper-indium-diselenide (CIS at a 0.7% share) and cadmium-telluride (CdTe at a 1% share) solar cell types. Table 7.1 provides an indication of the efficiency ranges of the different types of solar cells and the approximate areas needed to supply a 1 kWp (Falk, Durschner & Remmers, 2007).

Table 7.1: Solar Cell efficiency ranges and surface area requirements for a 1kWp

Source: Adapted from Falk, Durschner & Remmers (2007)

Cell Material	Efficiency (%)	Required surface area for 1 kWp (m^2)
Monocrystalline silicon	11-16	7-9
Polycrystalline silicon (EFG)	10-14	8-9
Polycrystalline silicon	8-10	9-11
Thin Film copper-indium-diselenide	6-8	11-13
Amorphous silicon	4-7	16-20

The performance of solar cells changes with cell temperature (discussed in Section 2.3.3) and different types of solar cells perform differently with temperature fluctuations. For example, crystalline solar cells experience an efficiency decrease of roughly 0.5% per degree rise in temperature while amorphous types exhibit a temperature decay of about 0.2% per degree rise in temperature. This makes amorphous types more preferable for hot conditions (Falk, Durschner & Remmers, 2007).

7.3 Appendix C: Water properties

7.3.1 Assumptions

- The system stays at approximately atmospheric pressure, and so this variable can be neglected in water property calculations. According to Sharqawy, Lienhard & Zubair (2010), the pressure in thermal desalination does not usually more than 10% of atmospheric pressure.
- The salinity of the water does not change with time. It is set to 35g.kg^{-1} of sea water, which is a salinity that corresponds to an oceanographic range (Sharqawy, Lienhard & Zubair, 2010).
- The water level does not change (i.e. it is constantly topped up). According to Sharqawy, Lienhard & Zubair (2010), brine discharge can be 1.5-2 times saltier. However, if the saline water is replaced at regular intervals (daily), this assumption becomes more valid.

7.3.2 Overview

This section presents equations that model the change of water density, the thermal conductivity, the dynamic viscosity and latent heat of vaporisation for saline water. Sharqawy, Lienhard & Zubair (2010) presents a series of regression equations for these thermophysical properties of saline water. Comparisons and recommendations are made for the range of applicability of each equation. According to this source, the difference between the properties of pure water and sea water vary by only 5 to 10%. However, these values significantly affect the performance of distillation processes, and it is thus necessary to have a more accurate estimation of their respective variations with changes in salinity, temperature and system pressure.

This study uses the International Practical Temperature Scale of 1968 (IPTS-68) which has its temperatures written as t_{68} (Fofonoff & Millard, 1991). It was assumed that measurements in this experiment would be conducted in the International Temperature Scale of 1990 (ITS-1990), which has its temperatures written as t_{90}, as this temperature scale supersedes the IPTS-

68 scale (Preston-Thomas, 1990). The two scales can be related by a linear conversion as shown by Eq. (7.10)(Fofonoff & Millard, 1991).

$$t_{68} = 1.00024 t_{90}$$

Note, that for convention purposes, an uppercase T denotes an absolute temperature scale (in Kelvin), while a lower case t denotes a Celsius temperature. Also, t_{90} is written as t because it is the assumed standard (Sharqawy, Lienhard & Zubair, 2010).

7.3.3 Density of Water

Sharqawy, Lienhard & Zubair (2010) recommends the use of Eq. (7.11) for the calculation of salt water density. It is recommended because it tolerates high temperatures (up to 180°C) and a broad salinity salinity(s_p) range (between 10gkg^{-1} and 160 gkg^{-1}. Additionally, this equation has a small error of about 1%. The operating specification of hybrid PV/T desalination systems falls well within this range and so this equation was chosen (Dev & Tiwari, 2010).

$$\rho_{sw} = (A_1 F_1 + A_2 F_2 + A_3 F_3 + A_4 F_4) \times 10^3 \quad (7.11)$$

$$B = (2S_p - 150)/150 \quad (7.12)$$

$$A_1 = 4.032 G_1 + 0.115 G_2 + 3.26 \times 10^{-4} G_3 \quad (7.13)$$

$$A_2 = -0.108 G1 + 1.571 \times 10^{-3}\, G2 - 4.23 \times 10^{-4} G3 \quad (7.14)$$

$$A_3 = -0.012 G1 + 1.74 \times 10^{-3} G2 - 9 \times 10^{-6}\, G3 \quad (7.15)$$

$$A_4 = 6.92 \times 10^{-4} G1 + 8.7 \times 10^{-5} G2 - 5.3 \times 10^{-5}\, G3 \quad (7.16)$$

$$\mathrm{A} = \frac{(2t_{68} - 200)}{160} \quad (7.17)$$

$$F_1 = 0.5 \tag{7.18}$$

$$F_2 = A \tag{7.19}$$

$$F_3 = 2A^2 - 1 \tag{7.20}$$

$$F_4 = 4A^3\text{-}3\text{A} \tag{7.21}$$

$$G_1 = 0.5 \tag{7.22}$$

$$G_2 = B \tag{7.23}$$

$$G_3 = 2B^2\text{-}1 \tag{7.24}$$

7.3.4 Specific Heat

Sharqawy, Lienhard & Zubair (2010) provides an equation for the correlation between specific heat and temperature. This is presented in Eq. (7.25). The range of validity for T_{68} is between 273°C and 453.15°C and, a salinity(s_p) between 0 gkg^{-1} and 180 gkg^{-1}. The accuracy of the approximation is estimated at about 0.28%.

$$C_{sw} = A + BT_{68} + CT_{68}{}^2 + DT_{68}{}^3 \tag{7.25}$$

$$A = 5.328 - 9.76 \times 10^{-2}S_p + 4.04 \times 10^{-4}S_p{}^2 \tag{7.26}$$

$$B = -6.913 \times 10^{-3}\text{+}7.351\times 10^{-4}S_p - 3.15 \times 10^{-6}S_p^2 \tag{7.27}$$

$$C = 9.6 \times 10^{-6}\text{-}1.927\times 10^{-6}S_p\text{+}8.23\times 10^{-9}S_p{}^2 \tag{7.28}$$

$$D = 2.5 \times 10^{-9} + 1.666 \times 10^{-9}S_p - 7.125 \times 10^{-12}S_p{}^2 \tag{7.29}$$

7.3.5 Thermal Conductivity

The thermal conductivity of water generally diminishes with an increase in the amount of dissolved salts. An equation which presents the correlation between the conductivity and the salinity of water is provided for by Eq. (7.30). This equation is said to have an accuracy of approximately 3%, with a temperature range of 0° to 180°C and a salinity between 0 and 160g/kg (Sharqawy, Lienhard & Zubair, 2010).

$$\log_{10}(K_{sw}) = \log_{10}(240 + 0.0002S_p) + 0.434\left(2.3 - \frac{343.5+0.037S_p}{T_{68}}\right)\left(1 - \frac{T_{68}}{647+0.03S_p}\right)^{0.333} \quad (7.30)$$

7.3.6 Dynamic Viscosity

The dynamic viscosity of salt water can be calculated according to Eq. (7.31). This equation is valid for temperature ranges between 20°C and 150°C. This equation requires the dynamic viscosity of fresh water which is given by Eq.(7.32) and the ionic strength of salt water which can be approximated by Eq. (7.33). A Salinity (s_p) range of between 15gkg^{-1} and 130 gkg^{-1} is acceptable with this equation. The equation may result in an error of approximately 0.4% (Sharqawy, Lienhard & Zubair, 2010).

$$\log_{10}\left(\frac{\mu_{sw}}{\mu_w}\right) = 0.0428I + 0.00123I^2 + 0.000131I^3 + (-0.03724I + 0.01859I^2 - 0.00271I^3)\log_{10}(\mu_w \times 10^3) \quad (7.31)$$

$$\mu_w = 4.2844 \times 10^{-5} + (0.157(t + 64.993)^2 - 91.296)^{-1} \quad (7.32)$$

$$I = \frac{19.915S_p}{(1 - 1.00487S_p)} \quad (7.33)$$

7.3.7 Latent Heat of Vaporisation

The latent heat of vaporisation for seawater is provided for by Eq. (7.34). This equation uses the fractional content of salt in the water to determine the latent heat of vaporisation for fresh water (given by Eq. (7.35). It uses an approximation to ideal sea water which varies little from actual seawater. The equation tolerates a range of temperatures between 0°C and 200°C, and it has an error of approximately 0.02% (Sharqawy, Lienhard & Zubair, 2010).

$$L_{sw} = L_w \times (1 - \frac{S}{1000}) \tag{7.34}$$

$$L_w = 2.501 \times 10^6 - 2.369 \times 10^3 \mathrm{t} + 2.678 \times 10^{-1} t^2 - 8.103 \times 10^{-3} t^3 - 2.079 \times 10^{-5} t^4 \tag{7.35}$$

7.4 Appendix D: Air Properties

Temperature dependent correlations for the thermophysical properties of air exist in literature (Mathur & Mathur, 2006). They assume that the temperature of the air between the glass and the panel/collector is the mean of the temperatures between the panel and the glass. The density of air is first given by Eq. (7.36), followed by the dynamic viscosity of air given by Eq. (7.37). Next, the specific heat of air is given is by Eq. (7.38) and the thermal conductivity of air by Eq. (7.39)

$$\rho_f = [1.1614 - 0.00353(T_m - 300)] \tag{7.36}$$

$$\mu_f = [1.846 + 0.00472(T_m - 300)] \times 10^{-5} \tag{7.37}$$

$$C_f = [1.007 + 0.00004(T_m - 300)] \times 10^{3} \tag{7.38}$$

$$K_f = [0.0263 + 0.000074(T_m - 300)] \tag{7.39}$$

7.5 Appendix E: Code

This section presents the code used in this thesis. The two main pieces of code for functions Main and WholeSystem are given in Section 7.5.1 and Section 7.5.2 accordingly. These functions correspond the activity diagrams given in Figure 3.9 and Figure 3.10 respectively. The rest of the supporting code is given in 7.5.3 through to Section 7.5.4. It should be noted that section does not provide the code used to extract data to excel files nor the code used to construct graphs. Also, as highlighted in the nomenclature, the subscript 'c' (and not 'q') is used to indicate the collector and 'i' (and not 'Ψ'), for insulation.

7.5.1 Main(…)

```
%Calculates the performance of a PV/T desalination system
function []=main(parameters,filename)

[materialProperties,structuralProperties,constants]=variableConstructor(parameters);%Load the properties relevant to the base case model
orientation=constants.orientation;% Load the orientation of the system
[weatherProperties,coordinates]=ReadingIn();%Update the weather properties to the appropriate values from excel
[materialProperties.H_cg,materialProperties.h_ci,materialProperties.h_ai]=CalcHourlyTransfCoeffs(materialProperties,structural
Properties,weatherProperties); % Calculate the heat transfer coefficient only dependent on wind speed (for the entire year)
salinity=constants.salinity;%load salinity
h=constants.timestep;%load the timestep
Outputs=  [12.1,12.1,12.1,12.1,12.1,12.1,12.1,12.1,12.1,0,0,12.1];%initialise the component temperatures

%Initialise Storage Vectors (note shown)

year='2007';%Year of the simulation
startHour=1;%start hour of the day for the simulation
endHour=24;%end hor of the day for the simulation
yearDailyEp=zeros(((endHour-startHour+1)),365); %Uses the amount of hours in the day to determine the number of entries in the database
yearDailyEnergyYield=zeros(1,365);
yearDailyEnergyAvailable=zeros(1,365);
previousAlpha_gPV=0;
heatTransferCoefficients=[0 0 0];%initialize heat transfer coefficients (coefficients to Excel file)
HourlyTransferCoefficients=[];
A_g=structuralProperties.A_g;%Load the area of the glass cover of the panel
A_gp=structuralProperties.A_gp;%Load the area of the glass above the panel only (not the exposed collector)
A_k= structuralProperties.A_k;%Load the area of the glass cover of the still
monthlyElecEfficiency=0;
monthlyThermalEfficiency=0;

for month=1:12
```

```
    startDay=doy(['1' '-' num2str(month) '-' year]);%Start day of the simulation (as a day of the year)
    endDay=doy(['31' '-' num2str(12) '-' year]);%End day of the simulation (as a day of the year)

    for dayofyear=startDay:endDay
        averageDailyElecEff=0;%Initialize
        averageDailyThermalEff=0;%Initialize
        inthervalHWaterYield=[]; %kgs of water per interval of h.
        inthervalHEnergyYield=[]; %kWh of energy yield per interval of h.
        intervalHEnergyAvailable=[]; %kWh of tilted irradiance available per interval of h.
        storageCounter=0; %reset the counter
        storedEp=zeros(1,(endHour-startHour+1));%Power stored
        storageTimeVector=[];%Time vector. Used to store time for printing purposes
        storedElecEfficiency=[];%Electrical Efficiency for each time interval of h
        storedThermalEfficiency=[];%Thermal Efficiency for each time interval of h
        storedThermalEfficiency_removal=[];%Thermal (heat removal from the panels) efficiency for each time interval of h
        oldRbSunRise=0;%Stores previous Rb value in case there a spike in Rb values occur (previous Rb then used)
        oldRbSunSet=0;%Stores previous Rb value in case there a spike in Rb values occur (previous Rb then used)
        declination=CalcDeclination(dayofyear);%Calculate the day's declination
        omegaRiseSet=CalcSunSetRiseOmega(coordinates.latitude,declination);% %Calculate the hour angles for sunset and
sunrise for the day
        previousAlpha_g=0; %previous alphas used for if spikes in values occur
        previousAlpha_k=0;
        previousAlpha_w=0;
        previousAlpha_b=0;
        sunHasRisen=0;%Makes sure first omega comparison made with positive version of sunset/sunrise
        for hour=startHour:endHour%1:24
            hourCount=(dayofyear-1)*24+(hour);%Calculate the hour of the year
            for timeStepTicker=1:(3600/h)
                if (timeStepTicker==1)  %at the start of every hour, find the Rb value at the midpoint of the previous hour (once) and
calculate hourly variables
                    midMinute=(hour-2)*60+30;%The minute the corresponds the to midpoint of the previous hour (hour-1 takes us to
the current hour (because 1 referenced), hour-2 takes us to the previous hour)

[Rb,oldRbSunRise,oldRbSunSet,isSunriseHour,isSunsetHour]=CalcRb(dayofyear,structuralProperties,coordinates,omegaRise
Set,midMinute,declination,oldRbSunRise, oldRbSunSet,orientation,'PVT');%Calculate Rb (PV part of the system)

[RbStill,oldRbStillSunRise,oldRbStillSunSet,isSunriseStillHour,isSunsetHourStill]=CalcRb(dayofyear,structuralProperties,coordi
nates,omegaRiseSet,midMinute,declination,oldRbSunRise, oldRbSunSet,orientation,'still'); %Calculate Rb (Solar still part of the
system)

[incidenceAnglePV,incidenceAngleStill]=CalcIncidence(structuralProperties,declination,coordinates,midMinute,dayofyear,orient
ation,orientation);%Calculate incidence angles for still and PV/T parts of the system
                    [refractionAnglePV]=CalcRefraction(incidenceAnglePV,structuralProperties);%Calculate the refraction angle for the
PV part of the system
                    [refractionAngleStill]=CalcRefraction(incidenceAngleStill,structuralProperties);%Calculate the refraction angle for
the PV part of the system
                    [H_g,sunHasRisen,H_z,H_t_pv,H_p,H_c,previousAlpha_g]=CalcPVHeatInput(dayofyear,Rb,oldRbSunRise,
hourCount,oldRbSunSet,isSunriseHour,isSunsetHour ,sunHasRisen,weatherProperties,structuralProperties,materialProperties,
constants,incidenceAnglePV, refractionAnglePV,previousAlpha_gPV,3);%Calculate the heat absorbed by the components of
the PV/T system
```

```
[previousAlpha_w,previousAlpha_b]=calcEffectiveAlphaInStill(materialProperties,previousAlpha_k,previousAlpha_w,previousAlpha_b,structuralProperties,incidenceAngleStill,refractionAngleStill,isSunriseHour,isSunsetHour);%Calculate the absorptivity factors in the still

[~,H_t_still,H_k,H_w,H_bs,previousAlpha_k]=CalcStillHeatInput(dayofyear,RbStill,oldRbStillSunRise,oldRbStillSunSet,isSunsetHour,isSunriseHour,
hourCount,weatherProperties,structuralProperties,materialProperties,constants,incidenceAngleStill,refractionAngleStill,previousAlpha_k,previousAlpha_w,previousAlpha_b); %Calculate the heat absorbed by the components of the still
            end;
            [Outputs,mdot,h_ew,heatTransferCoefficients,T_a,powerNeeded_pump]
=wholesystem(materialProperties,structuralProperties,weatherProperties,constants,hourCount,H_g,H_p,H_c,H_k,H_w,H_bs,Outputs,h,hour,powerNeeded_pump);%Perform all key calculations
            ouputForHTime=CalcIntervalWaterYield(h_ew,Outputs(6),Outputs(8),h,salinity); %Calculate water yield for time slither (h)
            inthervalHWaterYield=[inthervalHWaterYield;ouputForHTime];%Add the water yield to a running total
            energy= ((Outputs(10)-powerNeeded_pump)*(h/(3600))*10^-3)/(structuralProperties.A_gp);%Energy output (kWh in interval of h) per m^2
            inthervalHEnergyYield=[inthervalHEnergyYield;energy];%Store the energy yield
            energy= H_t_pv*(h/(3600))*10^-3;%Tilted irradiation (kWh in interval h)
            intervalHEnergyAvailable=[intervalHEnergyAvailable;energy];%Store the energy yield
        end

        HourlyTransferCoefficients=cat(1,HourlyTransferCoefficients,heatTransferCoefficients); %store the hourly heat transfer coefficients
        %Store all the outputs (temperatures, irradiance and power output) at the end of each hour (code not shown)
        %Sum and store energy available, energy yield and water yield at the end of every hour (code not shown)

        [Eff_e,Eff_t,Eff_t_removal]=
CalcEfficiencies(H_t_pv,H_t_still,Outputs(6),Outputs(7),Outputs(10),mdot,materialProperties,constants,structuralProperties,h,storedWaterMassYield(storageCounter));%Calculate the efficiencies
        %Store the efficiencies (not shown)

        storageTimeVector=BuildFormattedTimeString(storageTimeVector,hour,timeStepTicker);%Build a string to output variables

VariablePrinter(hour,dayofyear,storedElecEfficiency,storageCounter,mdot,Rb,oldRbSunRise,oldRbSunSet,H_t_pv,H_t_still,T_a);%Pring the hourly variables (to show in matlab)
    end
    storedTotalEfficiency=storedElecEfficiency+storedThermalEfficiency; %Calculate the total efficiency
    averageDailyMdot=(storedMdot(storedMdot~=0))/sum(storedMdot~=0);%average out the flow rate for the day
    dayMeanMdot=[dayMeanMdot averageDailyMdot];%store the day's average flow rate

    denom=1;
    if (sum(storedThermalEfficiency~=0)~=0) %If no days registered a thermal efficiency (irradiation below threshold value), use 1 in denom
        denom=sum(storedThermalEfficiency~=0);
    end

    denom=1;
```

```
        if (sum(storedThermalEfficiency_removal~=0)~=0) %If no days registered a thermal efficiency (irradiation below
threshold), use 1 in denom
            denom=sum(storedThermalEfficiency_removal~=0);
        end

averageDailyThermalEff_removal=sum(storedThermalEfficiency_removal(storedThermalEfficiency_removal~=0))/denom;%Cal
culate the efficiency (heat removal from the panels)
        dayMeanThermalEff_removal=[dayMeanThermalEff_removal averageDailyThermalEff_removal];%Store the thermal
efficiency
        avg=sum(storedTotalEfficiency(storedTotalEfficiency~=0))/sum(storedTotalEfficiency~=0);%averge non-zero elements
(Total efficiency)
        dayMeanTotalEff=[dayMeanTotalEff avg];%Store the total efficiency
        totalDailyWaterYield=sum(storedWaterMassYield); %Total the daily water yield
        yearDailyWaterYield(dayofyear) =totalDailyWaterYield;%Store the water yield for the day
        yearDailyEp(:,dayofyear)=storedEp; %Store the day's power outputs
        [averageEp]=CalcDailyAverageEp(yearDailyEp);%Calculate the average power output
        %total and store the day's energy yield
        %produced electrical energy
        totalDailyEnergyYield=sum( storedEnergyYield)/(A_gp); %Total the daily energy yield (change to per m^2)
        yearDailyEnergyYield(dayofyear)=totalDailyEnergyYield; %add the day's energy to stored values
        totalDailyEnergyAvailable=sum( storedTotalEnergyAvailable); %Total the daily energy available (for a whole day)
        yearDailyEnergyAvailable(dayofyear)=totalDailyEnergyAvailable; %Store energy available (as a daily value)

        monthlyWaterYield=monthlyWaterYield+totalDailyWaterYield;%Total the water yield for the month
        monthlyEnergyYield=monthlyEnergyYield+totalDailyEnergyYield;%Total the energy yield for the month
        monthlyElecEfficiency=monthlyElecEfficiency+averageDailyElecEff;%Total the efficiencies for the month
        monthlyThermalEfficiency=monthlyThermalEfficiency+averageDailyThermalEff;%Total the efficiencies for the month
        %
    end
    monthThermalEff_removalMean=sum(dayMeanThermalEff_removal)/daysInMonth(month);%Calculate an average thermal
efficiency (heat removal)
    dayMeanThermalEff_removal=[];%Clear the efficiency
    monthEnergyAvailableAverage=sum( yearDailyEnergyAvailable);
    yearDailyEnergyAvailable=[];% clear the daily energy levels
    monthEnergyTotal=sum(monthlyEnergyYield);
    monthEnergyAverage=monthEnergyTotal/daysInMonth(month);
    monthWaterTotal=sum(monthlyWaterYield);
    monthWaterAverage=monthWaterTotal/daysInMonth(month);
    monthMdotTotal=sum(dayMeanMdot);
    monthMdotAverage=monthMdotTotal/daysInMonth(month);
    monthElecEffAverage=sum(monthlyElecEfficiency)/daysInMonth(month);
    monthElecThermalAverage=sum(monthlyThermalEfficiency)/daysInMonth(month);
    monthTotalEquivalentEfficiency=monthElecEffAverage/0.43+monthElecThermalAverage;
    monthlySummary=[ monthWaterTotal monthWaterAverage monthEnergyTotal monthEnergyAverage monthElecEffAverage
monthElecThermalAverage monthTotalEquivalentEfficiency
monthMdotAverage,monthThermalEff_removalMean,monthEnergyAvailableAverage];
    %Calculate tracking variables
    monthlyWaterYield=0;
    monthlyEnergyYield=0;
    dayMeanElecEff=[];
```

```
    dayMeanThermalEff=[];
    dayMeanTotalEff=[];
    yearDailyEnergyYield=[];
    yearDailyEnergyAvailable=[];
end
end
```

7.5.2 WholeSystem(…)

```
%This function calculates the new temperatures the outputs of the system
%iteratively. In order to do this, it has to calculate other system
%properties too.
function [outputsFuture,appropriateMdot,h_ew,internalHeatTransferCoefficients,T_a,powerNeeded_pump]
=wholesystem(materialProperties,structuralProperties,weatherProperties,constants,hourCount,H_g,H_p,H_c,H_k,H_w,H_bs,ini
tialVariables,h,hour,powerNeeded_pump)
tolerance=0.5;%Tolerance of successive estimations (numerical method)
%Load the appropriate variables used in this function from materialProperties, structuralProperties, weatherProperties and
constants (not shown)
%Initialise Variables for estimation (not shown)
i=1;
outputsFuture=[];
internalHeatTransferCoefficients=[0 0 0];% For returning the internal heat transfer coefficients
compliantOutputs=[0 0 0 0 0 0 0 0 0 0 0 0];% elements set to one when they are within estimation tolerance
allTrue=ones(1,12);%check if all outputs are within the proper estimation tolerance
while (compliantOutputs ~=allTrue)
%Calculate the thermophysical air (panel air gap) and water (in the still and tubes) (not shown)
    h_rg=emissivity_g*boltzConst*((273+T_g(i) )^2+(273+T_sky )^2)*((273+T_g(i))+(275+T_sky));
    Beta=((T_g(i)+T_p(i))/2+273.5)^-1;
    Ra=CalcRa(Beta,T_p(i),T_g(i),thickness_ag_panel,kv_A,thd_A,g);
    Nu_a=CalcNusseltPV(tilt_PVT,Ra);%Nusselts number for air
    h_gp=boltzConst*e_eff_pg *((273+T_g(i))^2+(273+T_p(i))^2)*((273+T_g(i))+(273+T_p(i)))+(Nu_a*K_A)/thickness_ag_panel;
    %Calculate the emissivity of the the collector (not shown)
    Beta=((T_g(i)+T_c(i))/2+273.5)^-1;
    Ra=CalcRa(Beta,T_c(i),T_g(i),thickness_ag_collector,kv_A,thd_A,g);
    Nu_a=CalcNusseltPV(tilt_PVT,Ra);
    emissivity_eff_cg=(1/emissivity_c +1/emissivity_g -1)^(-1);
    h_gc=boltzConst*emissivity_eff_cg*((273+T_g(i))^2+(273+T_c(i))^2)*((273+T_g(i))+(273+T_c(i)))+(Nu_a*K_A)/thickness_ag
    _collector;
    h_rk=emissivity_k*boltzConst*((T_ko(i)+273.15)^2+(T_sky+273.15)^2)*(T_ko(i)+T_sky+546.30);
    P_w=exp(25.317-(5144/(273+T_w(i))));%Partial pressure from the water in the basin
    P_k=exp(25.317-(5144/(273+T_ki(i))));%Partial pressure from the inner cover of the basin

    if (T_w(i)-T_ki(i)>0)
        h_cw=0.884*(T_w(i)-T_ki(i)+((P_w-P_k )*(T_w(i)+273.15)/(268.9*(10)^(3)-P_w)))^(1/3);
    else
        h_cw=0;
    end

    h_rw=e_eff_wk*boltzConst*((T_w(i)+273.15)^2+(T_ki(i)+273.15)^2)*(T_w(i)+T_ki(i)+546.30);
```

```
    if (T_w(i)-T_ki(i)>0)
        h_ew=16.273*(10)^(-3)*h_cw*(P_w-P_k)/(T_w(i)-T_ki(i));
    else
        h_ew=0;
    end
    h_lw=h_cw+h_rw+h_ew;
    internalHeatTransferCoefficients=[h_rw h_cw h_ew];
    thickness_bs=structuralProperties.thickness_bs;
    h_bb=(1/(K_bs/thickness_bs )+1/((h_cb)))^(-1);%heat transfer coefficient from the basin bottom (neglect the radiation
component)
    h_bs=(waterContactArea/A_bb)*h_bb; %heat transfer to from the side of the basin (walls);


 %Calculate the mass of basin water (not shown)

[velocity_wt,appropriateMdot,powerNeeded_pump]=CalculatePumpFlowRate(constants,fittingR_t,fittingR_bs,g,mewTube,densi
ty_wt,L_t_tot,D_i,L_b,D_b,T_w(i),T_w1(i),a_1,a_2,A_t,A_bs,height_c,hour,E_p(i),powerNeeded_pump);
    K_tw=CalcThermalConductivtyWater(T_w1(i),S_p);
    h_tw=CalcH_w(velocity_wt,mewTube,D_i,K_tw,T_w(i),T_t(i));
    mewBasin=CalcViscosityWater(T_w(i),S_p);
    K_bw=CalcThermalConductivtyWater(T_w(i),S_p);
    h_bw=CalcH_w(velocity_wt,mewBasin,D_b,K_bw,T_w(i),T_bs(i));
    length_t_collector=structuralProperties.length_t_collector;
    hA_tw=(1/(h_tw*(pi*D_i*length_t_collector))+1/((c_bo*length_t_collector)))^(-1);
    C_w1=CalcSpecificHeatWater(T_w1(i),S_p);%Calulate the specific heat capcity of water in the tube
    C_w=CalcSpecificHeatWater(T_w(i),S_p);

    [E_p(i+1),G_p(i+1)]=CalcPanelPower(T_p(i),constants,materialProperties,H_p,A_gp);%Calculate panel power and heat
    T_ko(i+1)=(H_k*A_k+h_kk*A_k*T_ki(i)+h_ck*A_k*T_a+h_rk*A_k*T_sky)/(h_ck*A_k+h_rk*A_k +h_kk*A_k );%outer cover
    T_ki(i+1)=(h_lw*A_bb*T_w(i)+h_kk*A_k*T_ko(i+1))/(h_lw*A_bb+h_kk*A_k );%inner cover
    T_bs(i+1)=T_bs(i)+h*((H_bs*A_bb+h_bw*A_bw*(T_w(i)-T_bs(i))-h_bb*A_bb*(T_bs(i)-T_a)-h_bs*A_bb*(T_bs(i)-
T_a))/(M_bs*C_bs ));%basin
    T_g(i+1)=T_g(i)+h*((H_g*(A_gp+A_gc)+h_gp*A_gp*(T_p(i)-T_g(i) )+h_gc*A_gc*(T_c(i)-T_g(i) )-h_cg*A_g*(T_g(i)-T_a )-
h_rg*A_g*(T_g(i)-T_sky))/(M_g*C_g ));%glass
    T_p(i+1)=T_p(i)+h*((G_p(i+1)*A_gp-h_gp*A_gc*(T_p(i)-T_g(i+1) )-h_bp*A_bp*(T_p(i)-T_c(i) )-hA_pt*(T_p(i)-
T_t(i) ))/(M_p*C_p ));%panel
    T_c(i+1) =T_c(i)+ h*( (H_c*(A_gc)+h_bp*A_bp*(T_p(i+1)-T_c(i))-h_ct*A_ct*(T_c(i)-T_t(i))-h_bi*A_ci*(T_c(i)-T_i(i) )-
h_gc*A_gc*(T_c(i)-T_g(i) ))/(M_b*C_b ));
    T_t(i+1)=T_t(i)+h*((h_ct*A_ct*(T_c(i+1)-T_t(i) )+hA_pt*(T_p(i+1)-T_t(i))-h_it*A_it*(T_t(i)-T_i(i) )-hA_tw*(T_t(i)-
T_w1(i)))/(M_t*C_t )); %tube
    T_i(i+1)=T_i(i)+h*((h_bi*A_ci*(T_c(i+1)-T_i(i) )+h_it*A_it*(T_t(i+1)-T_i(i) )-h_ai*A_g*((T_i(i)-T_a )))/(M_i*C_i ));  %insulation
    T_w(i+1)=T_w(i)+h*((2*appropriateMdot*C_w1*((T_w1(i)-T_w(i)))+H_w*A_bb-h_bw*A_bw*(T_w(i)-T_bs(i+1))-
h_lw*A_bb*(T_w(i)-T_ki(i+1)))/(M_bw*C_w)); %water in basin
    T_w1(i+1)=T_w1(i)+h*((hA_tw*(T_t(i+1)-T_w1(i) )-2*appropriateMdot*C_w1*(T_w1(i)-T_w(i+1)))/(M_tw*C_w1)); %average
water temp in tube

    outputsPresent= [T_g(i) T_p(i)  T_c(i) T_t(i) T_i(i) T_w(i)  T_w1(i) T_ki(i) T_bs(i) E_p(i)  G_p(i) T_ko(i)];
    outputsFuture=[T_g(i+1) T_p(i+1)  T_c(i+1) T_t(i+1) T_i(i+1) T_w(i+1)  T_w1(i+1) T_ki(i+1) T_bs(i+1) E_p(i+1)  G_p(i+1)
T_ko(i+1)];
    compliantOutputs=  (abs(outputsFuture-outputsPresent)<tolerance);%check for compliancy of outputs with the tolerance
```

```
    i=i+1;

end
```

7.5.3 VariableConstructor(…)

```
function [materialProperties,structuralProperties,constants]=variableConstructor(parameters,filename)

tilt_PVT=parameters(2);
tilt_still=parameters(3);
heightOfWater_basin=parameters(4);
mdot=parameters(5);
accountForVF=1;
%Set the time step as a consant
h=60; %seconds
collectors=2;%number of collectors
orientation=1;%1 for north facing and 2 for Southfacing
S_p=35;%Salinity of the water
Tm=10;%number of tubes in each collector
length_g=2;%m length of panel
breadth_g=1;%width of panel
A_g=collectors*length_g*breadth_g; %area of glass above both collectors
length_p_pipe=1;%m %pipe under the panel
length_c_pipeFull=2;%whole length of the pipe
length_c_pipePart=length_c_pipeFull-length_p_pipe;%less the length of the panel
width_p=1;%Width of panel
A_gp=width_p*length_p_pipe; %area of panel under the glass
A_gc=length_c_pipeFull*breadth_g+length_c_pipePart*breadth_g;% area of collector under glass
additional_pipefactor=3;% how many addiitonal meters of pipe needed (not under the collector)
length_t_collector=collectors*((Tm*length_c_pipeFull)+2*(width_p));%Length of pipe under the collecor
length_t_total=length_t_collector+additional_pipefactor;%Total tube length (tube under the panel, Collector and the extra pipe
to the still)
length_bs=1;%length of the basin
width_bs=1;%windth of the basin
h_bp=100;%K_ad/thickness_ad;w/m^2k Chow(2003)
thickness_ad=0.00005;%0.05 mm Chamberlous (2006) review
K_ad=h_bp*thickness_ad;
K_i=0.038;% W/mk% wool
D_i=0.0186;%m
D_o=0.0213;%m
thickness_bo=D_o*(2-sqrt(2))/4;%thickness of the bond
W_bo=((2)^(1/2)/4)*D_o;%Width of the bond
pipeSpace=Tm*D_o; %Total space taken up by the pipe (width)
freeSpace=width_p-pipeSpace;%Space availble for spacing
W=freeSpace/Tm;%spacing permitted per pipe segment
k_w=628;%W/m.k
length_k=length_bs/cos(tilt_still);
depth_k=0.004;
width_k=1;
```

```
volume_k=length_k*depth_k*width_k;
A_k=length_k*width_k;
thickness_g=0.004;%Thicknes of the glass
extCoef=4;%Excitation coefficient
thickness_ag_panel=0.025;%thickness of panel and glass gap(Chow, He et al. 2006)
Q_g=[];
Q_p=[];
thickness_b=0.002;%thickness of collector
thickness_i=0.05;%thickness of insulation
density_cell=2320; %kg.m^3 (Falcone 2010)
thickness_p=0.003;%thickness of panel (Kitcher 2012)
thickness_ag_collector=thickness_ag_panel+thickness_p+thickness_ad;%thickness of the collector to glass airgap
M_p=density_cell*thickness_p*A_gp;%mass of the panel
density_b=2702;%density of the collector
A_gp=width_p*length_p_pipe; %area of panel under the glass
M_b=density_b*thickness_b*(A_gp+A_gc);%mass of the collector
density_t=8960; %density of the tube
cross_area_tube=pi()*(D_o/2)^2-pi()*(D_i/2)^2;%cross area of the tube
M_t=density_t*cross_area_tube*length_t_total;%mass of the tube
density_i=32;%density of the insulation
M_i=density_i*A_g*thickness_i;%mass of insulation
density_g=2500;%density of the glass
density_k=density_g;%density of the still cover
M_k=density_k*volume_k;%mass of the glass cover
M_g=density_g*A_g*thickness_g;%mass of the glass cover
alpha_bs=0.8;%absorbtivity of the basin
%M_wb=7;%mass of water in the
M_wt=7;%mass of water in the tube
C_w=4200;% heat capcity of the water (default)
x_p=W/4;%average heat path distance to the panel
refractiveIndexAir=1;
refractiveIndexGlass=1.526;
K_p=34;%thermal conductivity of panel
hA_pt=(2*K_p*thickness_p*length_p_pipe*K_ad*D_o)/(x_p*K_ad*D_o+2*K_p* thickness_p*thickness_ad );
efficiency_ref=0.15;%Referene panel efficiency
T_ref=20;%reference temperature
heatPerformCoef=0.0046;%performance coefficient for the panel
packingFactor=0.9375;%packing factor of panel
K_k=1.4;%thermal conductivity of the cover
h_kk=K_k/depth_k ;%heat transfer coefficient of the cover
C_p=678;%Heat capacity of the panel  (Acciani, Falcone & Vergura, 2010)
absorp_p=0.80;%Absorptivity of the panel
absorp_c=0.89; %Absorptivity of the collector
emssivity_w=0.95;% emissivity of water
emissivity_g=0.80; %emissivity of the glass
emissivity_p=0.85; %emissivity of the panel
emissivity_eff_pg=(1/emissivity_p +1/emissivity_g -1)^(-1);%effecitive emissivity between the panel and the glass
emissivity_k=emissivity_g; %emissivity from the glass cover of the still
K_t=401;% thermal conductivity of the tube (implicit in the C_bo factor)
K_b=K_t;% thermal conductivity of the absorber (copper)
```

```
x_b=(W-D_o)/4; %average heat path to the absorber
A_bp=A_gp*(1-D_o/W);%area of the absorber under the panel
h_ct=(2*K_b)/x_b;%heat transfer coefficient between the collector and the tube
h_bi=2*K_i/thickness_i;%heat transfer coefficient between the collector and the insulation
A_it=collectors*((pi/2+1)*D_o*length_c_pipeFull);%area of insulation in contact with the tube
h_ai=[];%heat tranfer coefficients between the insulator and air
h_it=h_bi;% heat transfer coefficient between the insulation and the tube
A_ct=collectors*thickness_b*length_c_pipeFull;%area of the collector in contact with the tube
A_ci=A_g*(1-(D_o/W));%area of the collector in contact with the insulation
A_t=pi*(D_i/2)^2;%area of inner tube (frontal)
V_t=A_t*length_t_total;%Volume of the entire tube
V_bs=length_bs*width_bs*heightOfWater_basin;%volume of the water in the basin
gReflectivity=0.2;%ground reflectivity
C_b=903;%heat capacity of the backplate
C_t=385;%heat capacity of the tube
C_i=835;%heat capacity of fibreglass insulation
C_g=750;%heat capacity of the glass
boltzConst=5.67*10^-8;%Boltzmann constant
gravity=9.81;
%these deal with the specific gravity of water
SG_temps=[0 1.7 4.4 10  15.6    21.1    26.7    32.2    37.8    48.9    60  71.1    82  93.3    100 104 116 127 138 149 160 171
182 193 204 216 227 238 248 260 271 282 293 304 316]; %temperatures
SG_outputs4=[1  1   1   0.999   0.999   0.998   0.996   0.995   0.993   0.989   0.983   0.977   0.97    0.963   0.958   0.955   0.947
0.938   0.928   0.918   0.908   0.896   0.885   0.873   0.859   0.849   0.832   0.817   0.801   0.785   0.765   0.746   0.72    0.703
0.678];
a = polyfit(SG_temps,SG_outputs4,2);
a_1=a(1);
a_2=a(2);
%weather properties
DifRad=[];%Diffused irradiation
DirectNormal=[];%direct normal irradiation
windSpeed=[];%wind speed
ambientTemp=[];%ambient temperature
%coordinates
long=0;
lat=0;
longSt=0; % longitude of the time zone
c_bo=100;%thermal conductance of the bond
h_cg=[];%heat transfer coefficients between the collector and the glass
h_ci=[];%heat transfer coefficient between the collector and insulation
%Frictional factors:
r_mouth=0.05;
r_elbow=0.43;
r_tee=0.54;
r_enlargement=0.99;
R1=r_tee+r_elbow;
R2=2*r_tee;
R_collector=(R1*R2)/((Tm-2)*R2+2*R1);%Total T resitances depend on the number of tubes.\
r_t=6*r_elbow+2*R_collector;
r_bs=r_mouth+r_enlargement;%fitting resitance in the basin
```

```
b_b=1;% breadth of basin
D_b=4*((heightOfWater_basin*b_b)/(b_b+2*heightOfWater_basin));%equivalent diameter of the basin
A_bs=pi()*(D_b/2)^2;%equivalent frontal area seen by water in transit
A_bw=(D_b)*pi()*length_bs; %area of water in contact with basin
A_bb=length_bs*width_bs;%area of the basin bottom
height_of_stand=1.5;%given parameter
height_c=height_of_stand+heightOfWater_basin;%use the design height
mew=631*10^(-6);%water viscosity (defailt)
L_w=2390*10^3;% Latent heat water (vaporization)
dV_w=453*10^-6;%dynamic viscosity of water (default)
kv_A=20.92*10^(-6);%kinematic viscosity of water (default)
G_sc=1367;%Solar Constant
thickness_bs=0.005;%thickenss of the basin
heightToCover_bs=0.57;% height from the top of the basin to the top of the cover
frontHeight_bs=0.4;%front height of the basin
backHeight_bs=frontHeight_bs+length_bs*tan(tilt_still);%back height of the basin
sideArea_bs=frontHeight_bs*length_bs;%side area of the basin
triangularArea_bs=0.5*length_bs*heightToCover_bs;%side triangular area of the basin
frontArea_bs=width_bs*frontHeight_bs;%front area of the basin
backArea_bs=backHeight_bs*width_bs;%back area of the basin
bottomArea_bs=thickness_bs*A_bb;%bottom area of the basin
A_side_bs=(2*sideArea_bs+2*triangularArea_bs+bottomArea_bs+frontArea_bs+backArea_bs);%side area of the basin
totalSurfaceArea_bs=(2*sideArea_bs+2*triangularArea_bs+bottomArea_bs+frontArea_bs+backArea_bs);%surface area of the
basin
materialVolume_bs=thickness_bs*totalSurfaceArea_bs;%Volume of the material making up the basin
density_bs=1700;%density of the basin
M_bs=density_bs*materialVolume_bs;%mass of the basin
waterContactArea=2*heightOfWater_basin*width_bs+2*heightOfWater_basin*length_bs;%water contact area in the basin
C_k=C_g;%heat capacity of the cover
C_bs=2300;%heat capacity of the basin
K_bs=0.028;%thermal conductivity of the basin
if (accountForVF==1) %check if the view factor is needed, if it is, calculate the emissiviity with it.
   W_wk=CalculateViewFactor(backHeight_bs,frontHeight_bs,width_bs,length_bs);
   emissivity_eff_wk=1/((1-emssivity_w)/emssivity_w +(A_bb*(1-emissivity_k))/(A_k*emissivity_k )+1/W_wk );
else
   emissivity_eff_wk=(1/emssivity_w +1/emissivity_k -1)^(-1);%calculate a simple emissivity without the vf
end;
pumpEfficiency=0.75;%Percent
%Load the appropriate variables into the MaterialProperties Structure (not shown)
% Load the appropriate variables into the StructuralProperties Structure (not shown)
%Load the appropriate variables into the weatherProperties Structure (not shown)
%Load the appropriate variables into the constants Structure (not shown)
%Load the appropriate variables into the coordinates Structure (not shown)
```

7.5.4 CalcStillHeatInput(…)

```
%this function is concerned with the heat input into the  solar still
function
[H_globalHoriz,H_globalTilted,H_k,H_w,H_bs,previousAlpha_k]=CalcStillHeatInput(dayofyear,RbStill,oldRbStillSunRise,oldRbS
tillSunSet,isSunsetHour,isSunriseHour,hourCount,weatherProperties,structuralProperties,materialProperties,constants,incidenc
eAngle,refractionAngle,alpha_g,effectiveAbsorptivity_w,effectiveAbsorptivity_b)
```

```
if  ((abs(oldRbStillSunRise)~=0) && (isSunriseHour==1) )
    %use the average for the sunrise hour
    [H_globalHoriz,H_globalTilted,H_k,H_w,H_bs,previousAlpha_k]=
CalcStillIrradiation(dayofyear,oldRbStillSunRise,hourCount,weatherProperties,structuralProperties,materialProperties,constants
,incidenceAngle,refractionAngle,alpha_g,effectiveAbsorptivity_w,effectiveAbsorptivity_b);
elseif ((abs(oldRbStillSunRise) ~=0) && (oldRbStillSunSet ~=0) && (isSunsetHour==1))
    %use the average for sunset hour
    [H_globalHoriz,H_globalTilted,H_k,H_w,H_bs,previousAlpha_k]=
CalcStillIrradiation(dayofyear,oldRbStillSunSet,hourCount,weatherProperties,structuralProperties,materialProperties,constants,i
ncidenceAngle,refractionAngle,alpha_g,effectiveAbsorptivity_w,effectiveAbsorptivity_b);
else
    %else use instantaneous Rb
    [H_globalHoriz,H_globalTilted,H_k,H_w,H_bs,previousAlpha_k]=
CalcStillIrradiation(dayofyear,RbStill,hourCount,weatherProperties,structuralProperties,materialProperties,constants,incidenceA
ngle,refractionAngle,alpha_g,effectiveAbsorptivity_w,effectiveAbsorptivity_b);
end
end
```

7.5.5 CalcAnisotrpicFactors(…)

```
%Calculates the Ai factor. Takes into account weather the Hb value is for a
%tilted or horizontal surface. Tilted surface figures have an Rb factor of
%1 and thus this is used to determine wether or not to correct for this
%when calculating the Ai factor
function [Ai]=CalcAnisotrpicFactors(Hb,dayofYear,constants,Rb)
B=CalcB(dayofyear);
G_sc=constants.G_sc;
G_on=G_sc*(1.000110+0.034221*cos(B)+0.001280*sin(B)+0.000719*cos(2*B) +0.000077*sin(2*B));
Ai=Hb/G_on;%ansitopic index (ratio of beam irradiation at surface to beam exteraterrestial beam irradaition. i.e. how much has
stayed in line)
if (Hb>0) %prevent division by 0
f=sqrt(Hb/(Hb+Hd));
else
    f=0;
end
end
```

7.5.6 CalcAlpha(…)

```
%Calculates the total absorbativity of the glass
function [alpha]=CalcAlpha(transMisvAb,incidenceAngle,refractionAngle,previousAlpha)
%1) Calcualte the components of reflectivity
    reflectPerp=(sin(refractionAngle-incidenceAngle))^2/(sin(refractionAngle+incidenceAngle))^2;
    reflectParallel=(tan(refractionAngle-incidenceAngle))^2/(tan(refractionAngle+incidenceAngle))^2;
%2) Calculates components of absorbatance
    alphaPerp=(1-transMisvAb)*(1-reflectPerp)/(1-reflectPerp*transMisvAb);
    alphaParallel=(1-transMisvAb)*(1-reflectParallel)/(1-reflectParallel*transMisvAb);
%3 Return average alpha
  alpha=(alphaPerp+alphaParallel)/2;
if ((alpha<0) || (alpha>1)) %if there is an abnormality in the alpha, use the previous one
```

```
    alpha=previousAlpha;
end
end
```

7.5.7 BuildFormattedString(...)

```
%Formats the strings for the graph (time)
function [storageTimeVector]=BuildFormattedTimeString(storageTimeVector,hour,minute)
   strhour=sprintf('%02d',hour);
    storageTimeVector=[storageTimeVector;strhour];
end
```

7.5.8 CalcBeta(...)

```
%Calculate the B factor
function [B]=CalcB(dayofyear)
B=(dayofyear-1)*2*pi/365;
end
```

7.5.9 CalcDailyAverageEp(...)

```
%Calculates the average daily power production
function [averageEp]=CalcDailyAverageEp(yearDailyEp)
  %Calculate the average for every day's Ep
  transEp=transpose(yearDailyEp);
[DAYS,TIME] = size(transEp);
averageEp=zeros(1,DAYS);
for  d=1:DAYS %for every day
 colTot=0;
 nonZero=0;
   for t=1:TIME  %total every time entry and divide by the number of non-zero elements
       if (transEp(d,t)>0)
      colTot= colTot+transEp(d,t);%count non-zero elements
      nonZero=nonZero+1;%count non-zero elements for averaging purposes
       end
   end
  averageEp(1,d)= colTot/nonZero;%Calculate the average for that day and store it
end
end
```

7.5.10 CalcDeclination(...)

```
%Calculate the thermal diffusivity of air
function thd_A=CalcThermalDiffusivityAir(T_p,T_g)
tempAv=((T_p+T_g)/2)+273.5;
density_a=(1.1614-0.00353*(tempAv-300));
C_a=(1.007+0.00004*(tempAv-300))*10^3;
K_a=(0.0263+0.000074*(tempAv-300));
thd_A=K_a/(density_a*C_a);
end
```

7.5.11 CalcDensityAir(...)

```
%Calcuates the density of air
function density_A=CalcDensityAir(temp)
%In degrees celcius
 temps=[0 20 40 60 80 100 120 140 160 180 200 250 300 350 400];
KA_outputs=[1.293 1.205 1.127 1.067 1 0.946 0.898 0.854 0.815 0.779 0.746 0.675 0.616 0.566 0.524];
p = polyfit(temps,KA_outputs,2);
density_A=p(1)*temp^2+p(2)*temp^1+p(3);
end
```

7.5.12 CalcDensityWater(...)

```
%Calculate the thermal diffusivity of air
function thd_A=CalcThermalDiffusivityAir(T_p,T_g)
tempAv=((T_p+T_g)/2)+273.5;
density_a=(1.1614-0.00353*(tempAv-300));
C_a=(1.007+0.00004*(tempAv-300))*10^3;
K_a=(0.0263+0.000074*(tempAv-300));
thd_A=K_a/(density_a*C_a);
end
```

7.5.13 CalcEffectiveAlphaInStill(...)

```
function
[effectiveAbsorptivity_w,effectiveAbsorptivity_b]=calcEffectiveAlphaInStill(materialProperties,absorptivity_g,previousAlpha_w,pr
eviousAlpha_b,structuralProperties,incidenceAngle,refractionAngle,isSunriseHour,isSunsetHour)
if (isSunriseHour) || (isSunsetHour) %if it is the sunset or sunrise hour, use the previous absorbtivities to avoid abnormalities in
incidence angles around these times
    effectiveAbsorptivity_w=previousAlpha_w;
    effectiveAbsorptivity_b=previousAlpha_b;
else
    alpha_b=materialProperties.alpha_b;
    depth_w=structuralProperties.heightOfWater_basin;
    %Calculate the glass reflectivity
    reflectPerp=(sin(refractionAngle-incidenceAngle))^2/(sin(refractionAngle+incidenceAngle))^2;
    reflectParallel=(tan(refractionAngle-incidenceAngle))^2/(tan(refractionAngle+incidenceAngle))^2;
    R_g= (reflectPerp+reflectParallel)/2;
    R_w=R_g;
    mew_theta=[0.237 0.193 0.167 0.179 0.124];
    theta=[0.032 0.45 3.0 35.0 255.0];
    %Calculate the attenuation that results from variation in water depth
    Flux_attenuation=0;
    for j=1:5
        Flux_attenuation=Flux_attenuation+mew_theta(j)*exp(-theta(j)*depth_w);
    end
    effectiveAbsorptivity_w=(1-R_g)*(1-absorptivity_g)*(1-R_w)*(1-Flux_attenuation);
    %Safeguard against sunrise/sunset angles:
```

```
    if ((effectiveAbsorptivity_w>1) || (effectiveAbsorptivity_w<0))
        effectiveAbsorptivity_w=0;
    end
    effectiveAbsorptivity_b=alpha_b*(1-R_g)*(1-absorptivity_g)*(1-R_w)*Flux_attenuation;
    if ((effectiveAbsorptivity_b>1) || (effectiveAbsorptivity_b<0))
        effectiveAbsorptivity_b=0;
    end
end
```

7.5.14 CalcEfficiencies(...)

```
%Calculates the efficiencies of the system

function
[electrical_eff,thermal_eff,Eff_t_removal]=CalcEfficiencies(H_t_pv,H_t_still,T_w,T_w1,Ep,mdot,materialProperties,constants,str
ucturalProperties,h,hourWaterYield)

T_w2=2*T_w1-T_w;
A_gp=structuralProperties.A_gp;
A_g=structuralProperties.A_g;
if (Ep ~=0) %check if we need to calculate the efficiency
    electrical_eff= (Ep/(H_t_pv*A_gp)*100);
else
    electrical_eff=0;
end
if ((H_t_pv >100) && (H_t_still >100))%threshold for thermal efficiency calculation
    C_w=materialProperties.C_w;
    salinity=constants.salinity;
    Tm=structuralProperties.Tm;
    A_k=structuralProperties.A_k;
    L_sw=CalcLatentHeatSW(T_w,salinity);
    thermal_eff=((hourWaterYield*L_sw)/(H_t_pv*(A_g)*3600+(H_t_still*A_k)*3600))*100;%thermal efficiency
    Eff_t_removal=((mdot*C_w*(T_w2-T_w1))/H_t_pv)*100;%heat removal thermal efficiency
else
    thermal_eff=0;
    Eff_t_removal=0;
end
end
```

7.5.15 CalcThermalDiffusivityAir(...)

```
%Calculate the thermal diffusivity of air
function thd_A=CalcThermalDiffusivityAir(T_p,T_g)
tempAv=((T_p+T_g)/2)+273.5;
density_a=(1.1614-0.00353*(tempAv-300));
C_a=(1.007+0.00004*(tempAv-300))*10^3;
K_a=(0.0263+0.000074*(tempAv-300));
thd_A=K_a/(density_a*C_a);
end
```

7.5.16 CalcH_w(...)

```
%Calculate the heat transfer coefficeint for water
 function [H_w]=CalcH_w(velocityMean,kinematicViscosity,diameter,K_w,T_w,T_x)
Re=CalcRe(velocityMean,kinematicViscosity,diameter) ;
Nu=0;
if (Re<2300) %If Laminar
    Nu=4.36;
else %if Turbulent
    Pr=CalcPr(T_w,T_w,'water');%calculate prandls number
    if (T_w>T_x)
        Nu=0.023*Re^(0.8)*Pr^(0.3);%cooling of the fluid
    else
        Nu=0.023*Re^(0.8)*Pr^(0.4);%heating of the fluid
    end
end
H_w=(Nu*K_w)/diameter;
end
```

7.5.17 CalcHourlyHeatTransferCoefficients(...)

```
%returns the values of explcitly known hourly variables (not depedent on
%temperatures of the system). Note, this code allows for the calculation of
%heat transfer coefficients based on "windward" or "leeward". The current calculation is not dependent on this.
function [h_cg,h_ci,h_ai]=CalcHourlyTransfCoeffs(materialProperties,structuralProperties,weatherProperties)% This needs lots
of change
dataLength=length(weatherProperties.WindSpeed);
h_cg=zeros(0,dataLength);
h_ai=zeros(0,dataLength);
h_ci=zeros(0,dataLength);
thickness_i= structuralProperties.thickness_i;
K_i=materialProperties.K_i;
for i=1:dataLength;
    %testNortherlySouhterly
    northerly=testNotherly(weatherProperties.WindDirection(i));
    if (northerly==1)
        h_cg(i)=weatherProperties.WindSpeed(i)*5.7+11.4;
        h_ci(i)=5.7;
        h_ai(i)=(thickness_i/K_i+1/h_ci(i))^(-1);
    else %southerly
        h_cg(i)=5.7;
        h_ci(i)=weatherProperties.WindSpeed(i)*5.7+11.4;
        h_ai(i)=(thickness_i/K_i+1/h_ci(i))^(-1);
    end
end
weatherProperties.IncidenceAngles=zeros(0,dataLength);%incidence angles
Q_g=zeros(0,dataLength);%irradiation data
```

```
end
```

7.5.18 CalcIncidence(...)

```
%Calculates the incidence angles of sunlight on the PVT and solar still
%parts of the system
function
[incidenceAngle_PVT,incidenceAngle_still]=CalcIncidence(structuralProperties,declination,coordinates,standardtimeMin,dayofyear,orientationPVT,orientationStill)
%Load coordinate related data (not shown)

[~,hourAngle]=CalcOmega(dayofyear,longLoc,longSt,standardtimeMin);
%PVT incidence angle calculations
tilt_PVT=structuralProperties.tilt_PVT;
if (orientationPVT==1)% north facing
   incidenceAngle_PVT=(acos(cos(declination)*cos(latitude+tilt_PVT)*cos(hourAngle)+ sin(declination)*sin(latitude+tilt_PVT)));
elseif (orientationPVT==2) %South facing
   incidenceAngle_PVT=acos(sin(declination)*sin(latitude-tilt_PVT)+ cos(declination)*cos(latitude-tilt_PVT)*cos(hourAngle));
end
tilt_still=structuralProperties.tilt_still;
if (orientationStill==1)% north facing
   incidenceAngle_still=(acos(cos(declination)*cos(latitude+tilt_still)*cos(hourAngle)+ sin(declination)*sin(latitude+tilt_still)));
elseif (orientationStill==2) %south facing
   incidenceAngle_still=acos(sin(declination)*sin(latitude- tilt_still)+ cos(declination)*cos(latitude- tilt_still)*cos(hourAngle));
end
```

7.5.19 CalcIntervalWaterYield(...)

```
%Calculate the water yield for an interval
function [intervalHYield]=CalcIntervalWaterYield(h_ew,T_w,T_k,h,salinity)
L_sw=CalcLatentHeatSW(T_w,salinity);
intervalHYield=((h_ew*(T_w-T_k))/L_sw)*h;
end
```

7.5.20 CalcKinematicViscosityAir(...)

```
%Calculate the kinematic viscosity of air
function kv_A=CalcKinematicViscosityAir(T_p,T_g)
tempAv=((T_p+T_g)/2)+273.5;
density_a=(1.1614-0.00353*(tempAv-300));
dynamicViscosity_a=(1.846+0.00472*(tempAv-300))*10^(-5);
kv_A=dynamicViscosity_a/density_a;
end
```

7.5.21 CalcLatentHeatSW(...)

```
%Calculate the latent heat of salt water
function L_sw=CalcLatentHeatSW(temp,salinity)
L_w=2.501*(10)^6-2.369*(10)^3*temp+2.678*(10)^(-1)*temp^2-8.103*10^(-3)*temp^3-2.079*10^(-5)*temp^4;
L_sw=L_w*(1-salinity/1000);
```

```
end
```

7.5.22 CalcOmegaRange(...)

```
%Function chooses the appropriate values of omega to deal with at
%sunrise/sunset
function
[omega1,omega2]=CalcOmegaRange(currentHourOmega,omegaRiseSet,closestHourOmega,isSunriseHour,isSunsetHour)
omega1=0;
omega2=0;
radiansPerHour=(15/180)*pi();
omegaSunrise=-omegaRiseSet;%introduce sign for sunrise omega
omegaSunset=omegaRiseSet;
if ((isSunriseHour==1) && (isSunsetHour==0))%if the sun rises in the next hour, integrate from time of sunrise to the next hour
   omega1=omegaSunrise;
   omega2=omegaSunrise+radiansPerHour;%the next hour
elseif ((isSunsetHour==1) && (isSunriseHour==0))%if the sun has risen and the sun will set within the next hour
   omega1=omegaSunset-radiansPerHour;
   omega2=omegaSunset;
elseif ((isSunsetHour==0) && (isSunriseHour==0)) %if it is neither of these two, the range quesiton is not relevant. Should
never get here.
   omega1=0;
   omega2=0;
end
end
```

7.5.23 CalcPanelPower(...)

```
%Calculate the panel power and heat
function [Ep,Gp]=CalcPanelPower(T_p,constants,materialProperties,Htp,A_gp)
T_ref=constants.T_ref;
efficiency_ref=materialProperties.efficiency_ref;
heatPerformCoef=materialProperties.heatPerformCoef;
r_c=materialProperties.packingFactor;
eff_cell_now=efficiency_ref*(1-heatPerformCoef*(T_p-T_ref ));
Ep=eff_cell_now*Htp*A_gp*r_c; %Calulate the total power
Gp=Htp-Ep; %subtract the total power used by the cell from the total power received on the cell for heat available
end
```

7.5.24 CalcPr(...)

```
%Calculates the Prandl number
function [Pr]=CalcPr(Temp1,Temp2,medium)%use average temeprature between shield and cover
averageTemp=(Temp1+Temp2)/2;%Calculate the average temp
averageTempKelvin=averageTemp+273.5;%change to kelvin
if strcmp(medium,'air')
   temps=[273.15 275 280 285 290 295 300 305 310 315 320 325 330 335 340 345 350 355 360 365 370 373.3 375 380 385];
```

```
    PR_outputs=[12.99 12.22 10.26 8.81 7.56 6.62 5.83 5.20 4.62 4.16 3.77 3.42 3.15 2.88 2.66 2.45 2.29 2.14 2.02 1.91 1.80
1.76 1.70 1.61 1.53];
    p = polyfit(temps,PR_outputs,2);
    Pr=p(1)*averageTempKelvin^2+p(2)*averageTempKelvin^1+p(3);
elseif strcmp(medium,'water')
    temps=[100  150 200 250 300 350 400 450 500];
    PR_outputs=[0.786   0.758   0.737   0.72    0.707   0.7 0.69    0.684   0.683];
    p = polyfit(temps,PR_outputs,2);
    Pr=p(1)*averageTempKelvin^2+p(2)*averageTempKelvin^1+p(3);
end
end
```

7.5.25 CalcPVHeatInput(...)

```
%Calcilate the Heat input on the PV panel
function
[H_g,sunHasRisen,H_globalHoriz,H_globalTiled,H_p,H_c,previousAlpha]=CalcPVHeatInput(dayofyear,Rb,oldRbSunRise,hour
Count,oldRbSunSet,isSunriseHour,isSunsetHour ,sunHasRisen,weatherProperties,structuralProperties,materialProperties,cons
tants,thisMinuteIncidenceAnglePV, thisMinuteRefractionAnglePV,previousAlpha,complexityLevel)
%oldRbsunrise and oldRbsunset are used to demerine whether or not to calculate with averages or not
if  ((abs(oldRbSunRise)~=0) && (isSunriseHour==1) )
    %use the average for the sunrise hour
    [H_g,sunHasRisen,H_globalHoriz,H_globalTiled,H_p,H_c,previousAlpha]=
CalcPVTIrradiation(dayofyear,oldRbSunRise,hourCount,sunHasRisen,weatherProperties,structuralProperties,materialPropertie
s,constants,thisMinuteIncidenceAnglePV, thisMinuteRefractionAnglePV,previousAlpha,complexityLevel);
elseif ((abs(oldRbSunRise) ~=0) && (oldRbSunSet ~=0) && (isSunsetHour==1))
    %use the average for sunset hour
    [H_g,sunHasRisen,H_globalHoriz,H_globalTiled,H_p,H_c,previousAlpha]=
CalcPVTIrradiation(dayofyear,oldRbSunSet,hourCount,sunHasRisen,weatherProperties,structuralProperties,materialProperties
,constants,thisMinuteIncidenceAnglePV, thisMinuteRefractionAnglePV,previousAlpha,complexityLevel);
else
    %else use 'instantaneous' Rb
    [H_g,sunHasRisen,H_globalHoriz,H_globalTiled,H_p,H_c,previousAlpha]=
CalcPVTIrradiation(dayofyear,Rb,hourCount,sunHasRisen,weatherProperties,structuralProperties,materialProperties,constants
,thisMinuteIncidenceAnglePV, thisMinuteRefractionAnglePV,previousAlpha,complexityLevel);
end
end
```

7.5.26 CalcPVTIrradiation(...)

```
%Calculate the irradiation absorbed by different parts of the PV/T system
function
[Gg,sunHasRisen,H_globalHoriz,H_globalTilted,Hp,Hc,alpha_g]=CalcPVTIrradiation(dayofyear,Rb,hourCount,sunHasRisen,we
atherProperties,structuralProperties,materialProperties,constants,incidenceAngle,refractionAngle,previousAlpha,complexityLev
el) %depends on incidence angle which accounts for specific minute time
beamfactor=0;
diffusedfactor=0;
groundfactor=0;
tilt=structuralProperties.tilt_PVT;
Hb=weatherProperties.DirectNormal(hourCount);%use the hour count to reference the appropriate data
Hd=weatherProperties.DifRad(hourCount);
transMisvAb=CalcTransmisvAb(structuralProperties,materialProperties,refractionAngle);
```

```
alpha_g=CalcAlpha(transMisvAb,incidenceAngle,refractionAngle,previousAlpha);%juse the previous alpha if alpha spikes
gReflectivity=materialProperties.groundReflectivity;
if (Rb ~=1) %don't use the anistropic model if you only have tilted surface (validation) data (difficulty calculating the factors)
    [Ai,f]=CalcAnisotrpicFactors(Hb,Hd,dayofyear,constants);
    beamfactor=Hd*Ai;
    diffusedfactor=(1-Ai)*(1+f*sin(tilt/2)^3)*((1+cos(tilt))/2);
    groundfactor=(Hb+Hd)*gReflectivity*(1-cos(tilt))/2;
else
    %else, if tilted irradaition given, use anistropic model
    beamfactor=0;
    diffusedfactor=1;
    groundfactor=0;
end
H_globalTilted=(Hb+beamfactor)*Rb+Hd*diffusedfactor+groundfactor;
H_globalHoriz=(Hb+Hd);
Gg=alpha_g*H_globalTilted;
%calc 3 absorbatance factors (beam, diff and ground)
[ta_beam,ta_beam_collector]=calcTA(structuralProperties,materialProperties,transMisvAb,incidenceAngle,refractionAngle,com
plexityLevel);

%calculate diff incidence angle and refraction angle
difIncidenceAngle=degtorad(59.7-0.1388*(radtodeg(tilt))+0.001497*(radtodeg(tilt))^2);
difRefractanceAngle=CalcRefraction(difIncidenceAngle,structuralProperties);
transMisvAbDiff=CalcTransmisvAb(structuralProperties,materialProperties,difRefractanceAngle);
[ta_diff,ta_diff_collector]=calcTA(structuralProperties,materialProperties,transMisvAbDiff,difIncidenceAngle,difRefractanceAngle
,complexityLevel);

%Calculate ground incidence angle and refraction angle (recalculate)
grndIncidenceAngle=degtorad(90-0.5788*(radtodeg(tilt))+0.0026993*(radtodeg(tilt))^2);%convert to degrees for the formula
grndRefractanceAngle=CalcRefraction(grndIncidenceAngle,structuralProperties);
transMisvAbGnd=CalcTransmisvAb(structuralProperties,materialProperties,grndRefractanceAngle);
[ta_ground,ta_ground_collecor]=calcTA(structuralProperties,materialProperties,transMisvAbGnd,grndIncidenceAngle,grndRefra
ctanceAngle,complexityLevel);

Hp=(Hb+ beamfactor)*Rb*ta_beam+Hd*diffusedfactor*ta_diff+groundfactor*ta_ground; %%changed the last cos term sign to
neg
Hc=(Hb+ beamfactor)*Rb*ta_beam_collector+Hd*diffusedfactor*ta_diff_collector+groundfactor*ta_ground_collecor; %Calculate
the heat absoprted by the collector plate
end
```

7.5.27 CalcNusseltPV(...)

```
%Calculate Nusselts number for the PV panel air gap
function [Nu]=CalcNusseltPV(tilt,Ra)
Nu=1+1.44*(1-(1708*(sin(tilt) )^1.6)/(Ra*cos(tilt)))*subplus(1-1708/(Ra*cos(tilt)))+subplus(((Ra*cos(tilt))/5830)^(1/3)-1);
if (isnan(Nu)==1) %check to see if it is a number
    Nu=0;
end
end
```

7.5.28 CalcThermalDiffusivityAir(...)

```
%Calculate the thermal diffusivity of air
function thd_A=CalcThermalDiffusivityAir(T_p,T_g)
tempAv=((T_p+T_g)/2)+273.5;
density_a=(1.1614-0.00353*(tempAv-300));
C_a=(1.007+0.00004*(tempAv-300))*10^3;
K_a=(0.0263+0.000074*(tempAv-300));
thd_A=K_a/(density_a*C_a);
end
```

7.5.29 CalcOmega(...)

```
%Calculate the hour angle
function [closestHourOmega,omega]=CalcOmega(dayofyear,longLoc,longSt,time) %used in ClacIncidence (to calculate the omega for specific incidence) and clacHourRb (to calc current hour omega and next hour omega)
B=CalcB(dayofyear);
degreesPerMinute=15/60;
radPerMinute=pi()*(degreesPerMinute/180);
radPerHour=pi()*(15/180);
E=229.2*(0.000075+0.001868*cos(B)-0.032077*sin(B)-0.014615*cos(2*B)-0.04089*sin(2*B));
nexthour=floor(time/60)+1;%+1 takes us to the current hour, +2 to the next hour
closestHourSolarTime=nexthour*60+E+4*(longSt*180/pi()-longLoc*180/pi());
closestHourOmega=radPerMinute*(closestHourSolarTime-12*60); %the omega form of the closes hour
solarTime=time+E+4*(longSt*180/pi()-longLoc*180/pi());%note, this is in minutes. Keep using minutes for omega; (change to degrees first???????)
omega=(solarTime/60-12)*15*pi()/180;%divide by 60 because it needs to be in hours
end
```

7.5.30 CalcRa(...)

```
%Calculate Raleigh's number
function Ra=CalcRa(Beta,T_high,T_low,thickness_a,kv_A,thd_A,g)
Ra=(g*Beta*abs(T_high-T_low)*thickness_a^3)/(kv_A*thd_A );
end
```

7.5.31 CalcRb(...)

```
%Calculate the ratio of tilted irradition to horizontal irradiation
function
[Rb,RbSunRise,RbSunSet,isSunriseHour,isSunsetHour]=CalcRb(dayofyear,structuralProperties,coordinates,omegaRiseSet,hour,todaysDeclination, oldRbSunRise,oldRbSunSet,orientation,surfaceType) %Calculates the average if it is a new sunrise/set for the day else uses the old one. If it is not in these hours, it uses the per minute Rb
%PVT and still may have different angles
if strcmp(surfaceType,'PVT')
    tilt=structuralProperties.tilt_PVT;
else
    tilt=structuralProperties.tilt_still;
end;
```

```
latitude=coordinates.latitude;
longLoc=coordinates.longitude;
longSt=coordinates.longitudeStandard;
[closestHourOmega,currentHourOmega]=CalcOmega(dayofyear,longLoc,longSt,hour);%Calculate the angle hour for the
current hour and the  next hour
Rb=0;
RbSunRise= oldRbSunRise;
RbSunSet=oldRbSunSet;
[isSunriseHour,isSunsetHour,sunBehindEarth]=checkSunRiseSetHour(currentHourOmega,omegaRiseSet);%check to see if it
is the sunset or rise hour. If it is, assign boolean variables to sunrise and sunset depending on which hour it is
%If Sunset or sunrise hour, calculate the average Rb
if (((isSunriseHour==1) && (isSunsetHour==0) && (oldRbSunRise==0)) || ((isSunriseHour==0) && (isSunsetHour==1) &&
(oldRbSunSet==0))) %if it is sunrise or sunset and if the average Rb for either sunset or sunrise has not been calculated

[omega1,omega2]=CalcOmegaRange(currentHourOmega,omegaRiseSet,closestHourOmega,isSunriseHour,isSunsetHour) ;
%calculate the omega range
    Rb=CalcRbAverage(latitude, tilt,omega1,omega2,todaysDeclination); %calculate the average Rb
    if ((isSunriseHour==1) && (isSunsetHour==0)) %assign this value to Rbsunrise or sunset if appropriate
        RbSunRise=Rb;
    elseif ((isSunriseHour==0) && (isSunsetHour==1))
        RbSunSet=Rb;
    end
else
    %just just use the instantanious Rb depending on the angle of incidence
    Rb=CalcRbInstant(tilt,latitude,todaysDeclination,currentHourOmega,orientation);
end
if ((sunBehindEarth==1))% if the sun is not up, Rb values dont matter
    Rb=0;
end
%if the Rbaverage for rise/set is beyond reasonable range or negative,neglect it.
if   ((RbSunRise>2))
    RbSunRise=2;
elseif (RbSunRise<0)
    RbSunRise=2;
end
if   ((RbSunSet>2))
    RbSunSet=2;
elseif (RbSunSet<0)
    RbSunSet=0;
end
if   ((Rb>2))
    Rb=2;
elseif (Rb<0)
    Rb=0;
end
end
```

7.5.32 CalcRbAverage(...)

```
%Calculate the average Rb value (ie. around sunset or sunrise)
function [Rb]=CalcRbAverage(latitude, tilt,omega1,omega2,declination)
azi=pi;
a=(sin(declination)*sin(latitude)*cos(tilt)-sin(declination)*cos(latitude)*sin(tilt)*cos(azi))*(omega2-
omega1)+(cos(declination)*cos(latitude)*cos(tilt)+cos(declination)*sin(latitude)*sin(tilt)*cos(azi))*(sin(omega2)-sin(omega1))-
(cos(declination)*sin(tilt)*sin(azi)*(cos(omega2)-cos(omega1))) ;
b=cos(latitude)*cos(declination)*(sin(omega2)-sin(omega1))+sin(latitude)*sin(declination)*(omega2-omega1);
Rb=a/b;
end
```

7.5.33 CalcRbInstant(...)

```
%Calculate an 'instantaneous' Rb value (that is, for an hour midpoint)
function Rb=CalcRbInstant(tilt,latitude,declination,omega,orientation)
if (orientation==1) %1 is optimally aligned north (180 degrees)

Rb=(cos(latitude+tilt)*cos(declination)*cos(omega)+sin(latitude+tilt)*sin(declination))/(cos(latitude)*cos(declination)*cos(omega)
+sin(latitude)*sin(declination));
else
   %South Facing
   Rb=(cos(latitude-tilt)*cos(declination)*cos(omega)+sin(latitude-
tilt)*sin(declination))/(cos(latitude)*cos(declination)*cos(omega)+sin(latitude)*sin(declination));
end
end
```

7.5.34 CalcRe(...)

```
%Calculate Reynolds number for the determination of turbulence
function [Re]=CalcRe(velocityMean,kinematicViscosity,diameter)
Re=(velocityMean*diameter)/(kinematicViscosity);
end
```

7.5.35 CalcThermalConductivtyWater(...)

```
%Calculate the thermal conductivity of water
function K_w=CalcThermalConductivtyWater(temp,S_p)
t_68=temp*1.00024;
logKsw=log10(240+0.0002*S_p)+0.434*(2.3-(343.5+0.037*S_p)/(t_68+273.15))*(1-(t_68+273.15)/(647+0.03*S_p ))^0.333;
K_w=10^(logKsw)*10^-3;
r=isreal(K_w);
end
```

7.5.36 ReadingIn(...)

```
%Reads in important climatic data from an excel file
function [weatherProperties,coordinates]=ReadingIn()

xlRangeDirectNormal = 'E7:E8766';
xlRangeDifHorzRad = 'D7:D8766';
```

```
xlRangeWindSpeed='O7:O8766';
xlRangeBulbTemp='P7:P8766';
xlRangeWindDirection='Q7:Q8766';
xlLong='D5';
xlLat='D3';
xlStLong='F5';
sheet=2;
filename='editedData.xlsx';
weatherProperties.DirectNormal=xlsread(filename,sheet,xlRangeDirectNormal);
weatherProperties.DifRad=xlsread(filename,sheet,xlRangeDifHorzRad);
weatherProperties.WindSpeed=xlsread(filename,sheet,xlRangeWindSpeed);
weatherProperties.AmbientTemp=xlsread(filename,sheet,xlRangeBulbTemp);
weatherProperties.WindDirection=xlsread(filename,sheet,xlRangeWindDirection);
coordinates.latitude=xlsread(filename,sheet,xlLat);
coordinates.longitude=xlsread(filename,sheet,xlLong);
coordinates.longitudeStandard=xlsread(filename,sheet,xlStLong);

end
```

7.5.37 Doy(...)

```
%Determine the day of the year
function day=doy(date)
DateString1 = '1-January-2007';
formatIn = 'dd-mmm-yyyy';
ref=datenum(DateString1,formatIn);
dateWanted=datenum(date,formatIn);
day=dateWanted-ref+1;
end
```

7.5.38 CalcViscosityWater(...)

```
%Calculate the viscosity of the water
function mew_sw=CalcViscosityWater(temp,S_p1)
S_p=S_p1*10^(-3);
I=(19.915*S_p)/((1-1.00487*S_p));
mew_w=4.2844*(10)^(-5)+(0.157*(temp+64.993)^2-91.296)^(-1);
ratio=0.0428*I+0.00123*I^2+0.000131*I^3+(-0.03724*I+0.01859*I^2-0.00271*I^3)*log10(mew_w*10^3);
mew_sw=(10^ratio)*mew_w;
end
```

7.5.39 CalcuateViewFactor(...)

```
%Calculates the view factor in the still (for radiative heat transfer)
function [W_wk]=CalculateViewFactor(backHeight_bs,frontHeight_bs,width_bs,length_bs)
%backwall and water
Z=backHeight_bs;
X=width_bs;
Y=length_bs;
H=Z/X;
```

```
W=Y/X;
F_w_back=(1/(pi*W))* (W*atan(1/W)+H*atan(1/H)-
(H^2+W^2 )^(1/2)*atan(1/(H^2+W^2 )^(1/2) )+0.25*log((((1+W^2)*(1+H^2))/(1+W^2+H^2 ))*((W^2*(1+W^2+H^2))/((1+W^2)*(W^
2+H^2)))^(W^2 )*((H^2*(1+H^2+W^2))/((1+H^2)*(H^2+W^2)))^(H^2 ) ));
%frontwall and water
Z=frontHeight_bs;
X=width_bs;
Y=length_bs;
H=Z/X;
W=Y/X;
F_w_front=(1/(pi*W))* (W*atan(1/W)+H*atan(1/H)-
(H^2+W^2 )^(1/2)*atan(1/(H^2+W^2 )^(1/2) )+0.25*log((((1+W^2)*(1+H^2))/(1+W^2+H^2 ))*((W^2*(1+W^2+H^2))/((1+W^2)*(W^
2+H^2)))^(W^2 )*((H^2*(1+H^2+W^2))/((1+H^2)*(H^2+W^2)))^(H^2 ) ));

%east and west calls (symmetrical)
Z=0.5*(frontHeight_bs+backHeight_bs);%average out to rectange
X=length_bs;
Y=width_bs;
H=Z/X;
W=Y/X;
F_w_side=(1/(pi*W))* (W*atan(1/W)+H*atan(1/H)-
(H^2+W^2 )^(1/2)*atan(1/(H^2+W^2 )^(1/2) )+0.25*log((((1+W^2)*(1+H^2))/(1+W^2+H^2 ))*((W^2*(1+W^2+H^2))/((1+W^2)*(W^
2+H^2)))^(W^2 )*((H^2*(1+H^2+W^2))/((1+H^2)*(H^2+W^2)))^(H^2 ) ));
F_w_side_total=2*F_w_side;

%total view factor
W_wk=1-(F_w_back+F_w_front+F_w_side_total);
end
```

7.5.40 CalculatePumpFlowRate(…)

```
%Calculate the pump flow rate
function
[velocity_m,appropropriateMdot,powerNeeded_pump]=CalculatePumpFlowRate(constants,fittingR_t,fittingR_bs,g,mew,density
_w,L_t_tot,D_i,L_b,D_b,T_w,T_w1,a_1,a_2,A_t,A_bs,height_c,hour,E_p,PreviousPowerNeeded_pump)
pumpEfficiency=constants.pumpEfficiency;
mdotConstant=constants.mdot;
powerNeeded_pump=0;
appropropriateMdot=mdotConstant;
if ((E_p>PreviousPowerNeeded_pump ) && (T_w<T_w1) && (appropropriateMdot ~=0))%if the power available is greater than
the previous amount of power needed for flow rate (power wont change much), run the pump and if there is still heat to be
gained in still. Also, if default mdot is 0, pump is off
   velocity_m=mdotConstant/(density_w*A_t);%m/s
   A=(fittingR_t)/(2*g)+fittingR_bs*(A_t/A_bs)/(2*g);%account for the different velocity in the still
   B=((32*mew)/(g*density_w))*((L_t_tot/(D_i)^2+(L_b*(A_t/A_bs))/(D_b)^2));%includes the area fraction to account for the
different velcotiy in the tube and basin
   head_total=A*velocity_m^2+B*velocity_m;%neglect head and pressure as at the same point (thus net is 0)
   powerNeeded_pump= mdotConstant*g*head_total/pumpEfficiency;
else
   [appropropriateMdot,
velocity_m]=CalculateFlowRate(fittingR_t,fittingR_bs,g,mew,density_w,L_t_tot,D_i,L_b,D_b,T_w,T_w1,a_1,a_2,A_t,A_bs,heigh
t_c);%just syphon outside of these hours
```

```
end
end
```

7.5.41 CalculateFlowRate(...)

```
%Calculates the flow rate in the system (in thermosiphon mode)
function [mdot,
velocity_m]=CalculateFlowRate(fittingR_t,fittingR_bs,g,mew,density_w,L_t_tot,D_i,L_b,D_b,T_w,T_w1,a_1,a_2,A_t,A_bs,heigh
t_c)
   A=fittingR_t/(2*g)+(fittingR_bs*(A_t/A_bs))/(2*g);%account for the different velocity in the still
   B=((32*mew)/(g*density_w))*((L_t_tot/(D_i)^2+(L_b*(A_t/A_bs))/(D_b)^2));%includes the area fraction to account for the
different velcotiy in the tube and basin
   C=(T_w-T_w1)*(2*a_1*T_w1+a_2)*height_c;
   velocity_m1=(-B+sqrt((B^2-4*A*C)))/(2*A);
   if (isreal(velocity_m1)==0) %check if real
      velocity_m1=0;
   end
   velocity_m2=(-B-sqrt((B^2+4*A*C)))/(2*A);
   if (isreal(velocity_m2)==0) %check if real
      velocity_m2=0;
   end
   if ((velocity_m1>0) &&  (velocity_m2<0)) %chose the positive one
      velocity_m=velocity_m1;
   elseif ((velocity_m1<0) &&  (velocity_m2>0)) %chose the positive one
      velocity_m=velocity_m2;
   elseif  ((velocity_m1>=0) &&  (velocity_m2>=0)) %if they are both positive, chose the smallest
      if (velocity_m1<velocity_m2)
         velocity_m=velocity_m1;
      else velocity_m=velocity_m1;
      end
   elseif ((velocity_m1<0) && (velocity_m2<0)) %if both are negative, use absolte them and use the value closer to 0
      if (abs(velocity_m1)<abs(velocity_m2))
         velocity_m=abs(velocity_m1);
      else velocity_m=abs(velocity_m1);
      end
   else
      velocity_m=0; %Close valve when temperature saturation occures
   end
mdot=velocity_m*density_w*(A_t);

end
```

7.5.42 CalculateThermalConductivityAir(...)

```
%Calculate the thermal conductivity of air
function K_A=CalcThermalConductivityAir(temp)
K_A=(0.0263+0.000074*(temp-300));
end
```

7.5.43 CalcThermalDiffusivityAir(...)

```
%Calculates the Thermal Diffusivity of Air
```

```
function thd_A=CalcThermalDiffusivityAir(T_p,T_g)
tempAv=((T_p+T_g)/2)+273.5;
density_a=(1.1614-0.00353*(tempAv-300));
C_a=(1.007+0.00004*(tempAv-300))*10^3;

K_a=(0.0263+0.000074*(tempAv-300));

thd_A=K_a/(density_a*C_a);

end
```

7.5.44 CalcTransmisvAb(...)

```
%Calculate the transmittance of glass
function [transmisv]=CalcTransmisvAb(structuralProperties,materialProperties,refractionAngle)
extCoef_g=materialProperties.extCoef;
transmisv=exp(-(extCoef_g*structuralProperties.thickness_g)/cos(refractionAngle));
end
```

7.5.45 calcTA(...)

```
%Calculates the6.3.45   transmittance-absorptance for the glass and the
%panel/collector
function
[ta,ta_c]=calcTA(structuralProperties,materialProperties,transMisvAb,incidenceAngle,refractionAngle,complexityLevel) %calcul
ates Transmission Absorption for Beam on panel
reflectPerp=(sin(refractionAngle-incidenceAngle))^2/(sin(refractionAngle+incidenceAngle))^2;
reflectPar=(tan(refractionAngle-incidenceAngle))^2/(tan(refractionAngle+incidenceAngle))^2;
transMisvPerp= transMisvAb*(1-reflectPerp)^2/(1-(reflectPerp*transMisvAb)^2) ;
transMisvPar= transMisvAb*(1-reflectPar)^2/(1-(reflectPar*transMisvAb)^2) ;
transMisvTotal=0.5*transMisvPerp+0.5*transMisvPar; %Average for total transmisivity of glass
refractionAngleUnder=CalcRefraction(pi/3,structuralProperties);%calculate a new refraction angle from the perspective of
beneath the glass
transMisvAbUnder=CalcTransmisvAb(structuralProperties,materialProperties,refractionAngleUnder);% Transmissivity due to
absorption only
%reflection angle
reflectUnderPerp=(sin(refractionAngleUnder-pi/3))^2/(sin(refractionAngleUnder+pi/3))^2;
reflectUnderPar=(tan(refractionAngleUnder-pi/3))^2/(tan(refractionAngleUnder+pi/3))^2;
%Transmisvity for light heading out (depends on reflection angles and
%transmisvity due to absorption from beneath
transMisvPerpUnder= transMisvAbUnder*(1-reflectUnderPerp^2)/(1-(reflectUnderPerp*transMisvAbUnder)^2);
transMisvParUnder=transMisvAbUnder*(1-reflectUnderPar)^2/(1-(reflectUnderPar*transMisvAbUnder)^2) ;
transMisvTotalUnder=(transMisvPerpUnder+transMisvParUnder)/2;
difReflectivityPerp= reflectUnderPerp+ reflectUnderPerp*( transMisvTotalUnder^2*((1-reflectUnderPerp))^2)/(1-
((reflectUnderPerp*transMisvTotalUnder))^2);
```

```
difReflectivityPar=reflectUnderPar+reflectUnderPar*(transMisvTotalUnder^2*((1-reflectUnderPar))^2)/(1-
((reflectUnderPar*transMisvTotalUnder))^2);
difReflectivity=0.5*difReflectivityPerp+0.5*difReflectivityPar;%average them out
ta=0;
ta_c=0;
if (complexityLevel==1) %see if it's only a solar still
    absorp_w=materialProperties.absorp_w;
    ta=(transMisvTotal*absorp_w)/(1-(1-absorp_w)* difReflectivity);
    ta_c=0;% Set collector transmission absoprtion factor to zero if there is only a solar still (not relevant).

elseif (complexityLevel==2) %see if it's a pv/t-solar still
    absorbP=materialProperties.absorptionPanel;

    ta=(transMisvTotal*absorbP)/(1-(1-absorbP)* difReflectivity);
    ta_c=0;
elseif (complexityLevel==3) %see if it's a pv-t-solar still with exposed collector (without the PV panels above it)
    absorbP=materialProperties.absorptionPanel;
    absorbC=materialProperties.absorptionCollector;
    ta=(transMisvTotal*absorbP)/(1-(1-absorbP)* difReflectivity);
    ta_c=(transMisvTotal*absorbC)/(1-(1-absorbC)* difReflectivity); %TA factor for the collector
end
if (ta<0)
    ta=0;
end;
if (ta_c<0)
    ta_c=0;
end
end
```

7.5.46 CalcSunSetRiseOmega(...)

```
%Calculate Omega at sunset/sunrise
function [omega]=CalcSunSetRiseOmega(latitude,declination)

omega=(pi/180)*acosd(-tan(latitude)*tan(declination));
end
```

7.5.47 CalcSpecificHeatWater(...)

```
%Calculate the specific heat of water
function C_w=CalcSpecificHeatWater(temp,S_p)
T_68=(temp+273.15)*1.00024;%Convert to Kelvin scale
A=5.328-9.76*(10)^(-2)*S_p+4.04*(10)^(-4)*(S_p)^2;
B=-6.913*(10)^(-3)+7.351*(10)^(-4)*S_p-3.15*(10)^(-6)*S_p^2;
C=9.6*(10)^(-6)-1.927*(10)^(-6)*S_p+8.23*(10)^(-9) *S_p^2;
D=2.5*(10)^(-9)+1.666*10^(-9)*S_p-7.125*10^(-12)*S_p^2;
C_w=(A+B*T_68+C*(T_68)^2+D*(T_68)^3)*(10)^(3); %find the output and covert to J/kg
end
```

7.5.48 CalcRefraction(…)

```
%Calculate the refraction angle
function [refractanceAngle]=CalcRefraction(incidenceAngle,structuralProperties)

refractanceAngle=degtorad(asind(structuralProperties.refractiveIndexAir*sin(incidenceAngle)/structuralProperties.refractiveIndexGlass));
end
```